SPARK PLASMA SINTERING OF SILICON CARBIDE, MULTI-WALLED CARBON NANOTUBE AND GRAPHENE REINFORCED ZIRCONIUM DIBORIDE CERAMIC COMPOSITE

By

GOVINDARAAJAN BALARAMAN

YADHUKULAKRISHNAN

Bachelor of Science in Mechanical Engineering

Anna University

Chennai, India

2010

Submitted to the Faculty of the
Graduate College of the
Oklahoma State University
in partial fulfillment of
the requirements for
the Degree of
MASTER OF SCIENCE
July, 2012

SPARK PLASMA SINTERING OF SILICON CARBIDE, MULTI-WALLED CARBON NANOTUBE AND GRAPHENE REINFORCED ZIRCONIUM DIBORIDE CERAMIC COMPOSITE

Thesis Approved:

Dr. Sandip P. Harimkar

Thesis Adviser

Dr. Kaan A. Kalkan

Dr. Hamed Hatami-Marbini

Dr. Sheryl A. Tucker

Dean of the Graduate College

TABLE OF CONTENTS

Chapter Page

Chapter Page

Chapter Page

Chapter Page

LIST OF TABLES

LIST OF FIGURES

Figure Page

CHAPTER 1

Introduction

1.1 Introduction

Space vehicles re-entering the earth’s atmosphere experience very high temperatures due to aerodynamic heating. The need for materials that can operate at temperatures above 3000˚C with retained mechanical properties and limited oxidation has led to the development of ultra high temperature ceramics (UHTCs). UHTCs have melting point higher than 3200˚C and posses good oxidation resistance in extreme environments. However for UHTCs to be the future material for hypersonic re-entry vehicles there is a critical need in the improvement their thermal shock resistance, oxidation resistance and mechanical properties like strength and fracture toughness. Zirconium and hafnium based diboride have been identified as the most promising among the family of UHTCs. Reinforcements are added to UHTCs for better densification during sintering and improved mechanical and oxidation properties. In this study spark plasma sintering (SPS) of silicon carbide (SiC), multi-walled carbon nanotube (CNT) and graphene nano platelets (GNP) reinforced zirconium diboride (ZrB_2) UHTC composites is reported. Detailed characterization including phase and micro structural analysis, and multi-scale mechanical characterizations were performed and reported.

1.2 Ultra high temperature ceramics (UHTCs):

Ceramic is an inorganic, non-metallic compound usually made from a transition metal and a non-metal. The family of ceramic borides, carbides and nitrides with very high melting points, high hardness, chemical inertness and good oxidation resistance at extreme environments came to know as Ultra High Temperature ceramics (UHTCs) [1-3]. The strong chemical bonds in these ceramics give them the structural stability at high temperatures [1]. The ceramic carbides bonds are usually classified as covalent and interstitial. The common covalent carbides are SiC and B_4C which are extremely hard and exhibit good thermal and chemical stability. HfC, ZrC and TaC are some of the common interstitial carbides. They have very high melting points and also retain good strength at high temperatures [4]. Ceramic nitrides are also high melting point materials with high hardness but difficult to fabricate due to strong covalent bonds [5]. The better oxidation resistance of the ceramic borides makes them the most interesting among the UHTC family. The borides also have low coefficient of thermal expansion and high thermal and electrical conductivities [6]. HfB_2 and ZrB_2 are the most promising among the diboride UHTCs because of their combination of mechanical, thermal and oxidation properties [7-8].

1.2.1 Properties of UHTCs

UHTCs exhibit very high melting points in the range of 3000-3900˚C making them suitable for high temperature applications. The ceramic carbides exhibit high melting points than the ceramic diborides. Thus they require higher processing temperatures for sintering. Good mechanical properties are needed for any structural application. The Young’s moduli and hardness of these UHTCs are very high due to their strong covalent bonding. They also exhibit good flexural strength and it varies by the method of processing and resulting grain sizes. Whereas fracture toughness for these ceramic systems is considerably low due to their brittle nature. Therefore improvement in the fracture strength is critically important for the UHTCs. In order for high temperature applications, a material should have high thermal conductivity and low co-efficient of thermal expansion (CET) and good oxidation resistance. The UHTCs systems have good thermal and oxidation properties at elevated temperatures making them suitable material for high temperature application. The thermal conductivities of the borides are high compared to other high temperature ceramics. They also have comparatively low co-efficient of thermal expansion. Usually reinforcements are added to these ceramic matrixes to obtain better mechanical, thermal and oxidation resistance properties. The effect of reinforcements on the various properties of the UHTCs is discussed in detail later in this chapter. The melting points and mechanical properties of some of the UHTCs are listed in table 1.

Table 1.1 Density and Properties of UHTCs [1, 9-10]

Material	Density (g/cc)	Melting Point (˚C)	Young's Modulus (GPa)	Hardness (GPa)
ZrB_2	6.09	3245	500	25.3-28.0
HfB_2	11.19	3380	530	21.2-28.4
ZrC	6.56	3400	348	27.0
HfC	12.76	3900	352	26.0
TaC	14.50	3800	285	18.2

1.2.2 Applications

The most important application of UHTC is in the leading edges and nose caps of re-entry space vehicles. Space vehicles re-entering the earth's atmosphere is aero-thermodynamically heated up to very high temperatures. Present day space vehicles are designed with blunt body and large radius leading edges and nose caps to maintain moderate temperatures avoid material failure due to thermal stress. But such blunt design will dramatically reduce the maneuverability of the vehicle due to drag and also reduces the cross range during re-entry. To improve the maneuverability and decrease the cross range of hypersonic space vehicles we need vehicles with sharp leading edges and slender body design. The sharp leading edges will improve the lift to drag ratio of the vehicle and also decreases the cross range, enabling the vehicle to decent from its orbit and ensures safe landing at desired locations. Therefore there is a critical need for materials that can withstand the thermodynamic heating occurring during reentry and retain its mechanical properties to avoid failure of the vehicle. This led to the development of Ultra High Temperature Ceramics, a relatively new and promising material for next generation space vehicles [11]. UHTCs also find industrial and military applications [12-13]. The important applications of UHTCs are listed below:

1. Leading edge of re-entry and hypersonic space vehicles
2. Nose caps of re-entry and hypersonic space vehicles
3. Thermal protection systems in military applications
4. Molten metal crucibles
5. Electrical heaters
6. Electrical igniters

1.3 UHTC matrix composites

As the melting point of UHTCs is very high, sintering them to full densification requires high temperatures, high pressures and long processing times. This leads to significant grain growth, porosity and also cracking of samples during sintering, all of which will reduce the mechanical properties of the bulk samples [2-3]. To improve the sinterability and densification of these UHTCs, sintering additives or reinforcements are added to the ceramic matrix. They help in better densification at lower processing temperatures and also act as grain growth inhibitors [14-15]. This leads to the improvement of mechanical properties of UHTC ceramic composites. They also improve the oxidation resistance by forming passive oxide layers on the sintered bulk samples. The mechanisms of densification and improvement in mechanical, thermal and oxidation resistance of UHTC composites is explained in detail later in this chapter.

1.3.1 Classification of reinforcement in UHTC composites

The type of reinforcements used in UHTC matrix can be broadly classified into ceramic-ceramic reinforcement and graphitic-ceramic reinforcements. In the ceramic-ceramic reinforcement, a harder phase ceramic material is used as reinforcement in the UHTC ceramic matrix. Usually the reinforcement ceramic has a lower melting point than the matrix ceramic. These reinforcements are usually sintering additives than enable better densification of the composite matrix. They also improve the oxidation resistance of the composite in certain cases. The other kind of reinforcement is the graphitic-ceramic reinforcement, where graphite based materials are used as reinforcement in the UHTC matrix. These reinforcements do not have direct impact on densification, but they significantly improve the mechanical properties of the composites. The various potential reinforcements for UHTC matrix composites are explained below.

1.3.1.1 Ceramic reinforced UHTC composites

The ceramic reinforced UHTC composites can be classified into two types

(a) Particle reinforced UHTC composites

(b) Whisker/short fiber reinforced UHTC composites

1.3.1.1.1 Particle reinforced UHTC composites

Ceramic particle reinforced UHTC matrix is the most common form of UHTC composites. This is mainly because of the ease of dispersion and consolidation of ceramic in ceramic matrix. There is no need for any special colloidal dispersion techniques for obtaining good dispersion of reinforcements in the ceramic matrix. Mechanical processing methods like attrition milling or high energy ball milling is used to obtain uniform dispersion of ceramic particle reinforcement in UHTC matrix. The addition of stiffer reinforcement particles will enable the matrix to transfer the load to the reinforcements which is a direct strengthening process. There is also an indirect mechanism of strengthening that is caused by the difference in thermal conductivities of the reinforcement and the matrix. This thermal mismatch leads to the formation of dislocations at the matrix-reinforcement interface and enables indirect strengthening of the matrix [16-17].

Silicon carbide (SiC) with a lower melting point (2820˚C) than UHTCs and high hardness (32 GPa) [18] is the most promising ceramic particle reinforcement. The size of the SiC particles can vary from nano to few micro meters in diameter. SiC is added as sintering additive and it promotes densification of the UHTC composite. SiC also acts as grain growth inhibitor of the UHTC matrix [19-20], promoting smaller grains and improving the strength of the composite. Since SiC is a very hard material, they improve the hardness of the composites. They also improve fracture toughness of the composite by toughening mechanisms like crack deflection and shearing of the reinforcement particles. Several investigations have indicated that SiC reinforcement proved the strength, hardness and fracture toughness of the UHTC composites through the above mentioned mechanisms [21-27].The most important aspect of addition of SiC is the oxidation resistance it provides to the UHTC composite. SiC at high temperatures forms SiO_2 a product of oxidation which acts as a stable passive oxidation protection layer up to 1700˚C, this improves the oxidation resistance of the composite [7, 28-38]. The studies on SiC reinforced ZrB_2 UHTC composites are explained in detail in the review of ZrB_2 based UHTC composites section.

Apart from SiC, there are other ceramics that has been used as reinforcements in UHTC composites. Gang Li *et al.* [39] used different particle sizes of BN as reinforcement in ZrB_2-SiC ceramic matrix.

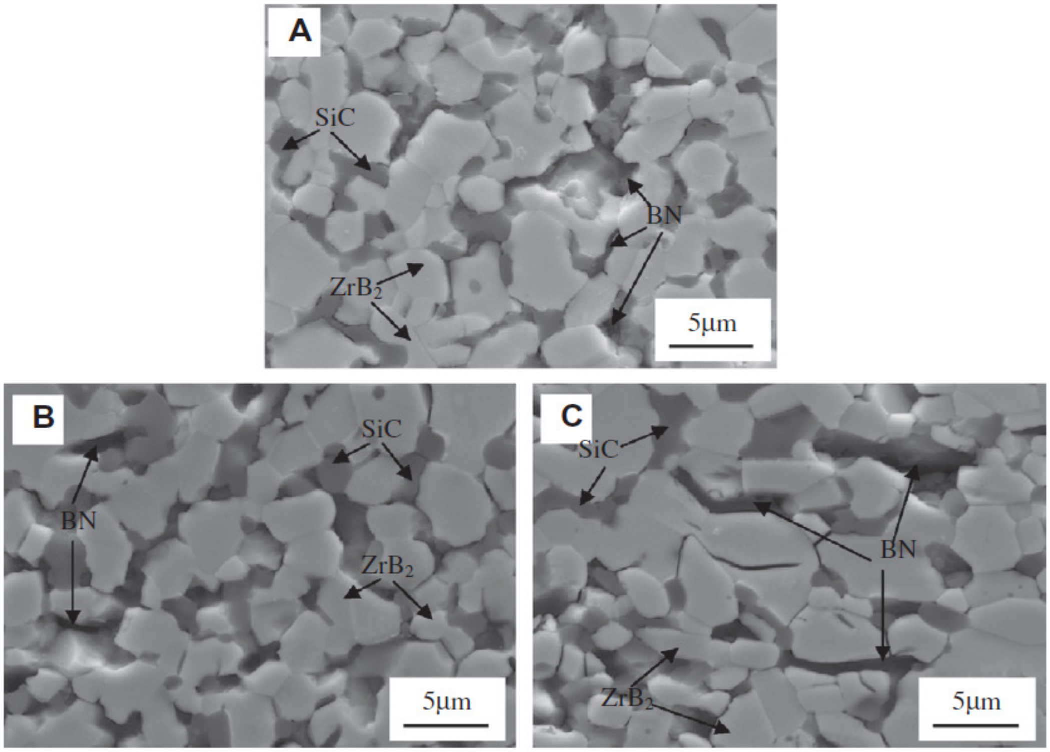

Fig. 1.1 SEM micrographs of polished-etched surfaces of ZrB_2-SiC composites with (A) 1µm BN, (B) 5 µm BN and (C) 10 µm BN particles [39].

Figure 1.1 shows the (SEM micrographs taken on the polished surfaces) uniform distribution of BN particles in the ZrB_2-SiC composite matrix. The addition of BN to the ZrB_2-SiC system improved the fracture toughness of the ceramic composites. This improvement in toughness was attributed by weaker interface bonding leading to improved crack deflection and stress relaxation near the crack tip. But this weak interface bonding and also lower relative density lead to lower flexure strength of the samples. Among the composites, ZrB_2-SiC with 5µm BN particles had better strength and fracture toughness. The addition of BN also improved the thermal shock resistance in the composites.

Zhang *et al.* [40] used B_4C and resin derived carbon as the reinforcements in ZrB_2-SiC ceramic system. The effect of SiC and C on ZrB_2 was reported. B_4C was added as sintering additive to enable pressureless sintering of ZrB_2-SiC and also aided in the removal of the surface oxides.

1.3.1.1.2 Whisker/short fiber reinforced UHTC composites

Whisker/short fibers have an aspect ratio (length to diameter ratio) of ~10-1000 and diameter in the range of 0.1-25 μm [41]. The whiskers are smaller in length compared to the short fibers. The purpose of whisker/short fiber reinforcement to the UHTC matrix is to improve the strength and fracture toughness by convention mechanisms like fiber pull-out, crack deflection and crack bridging. However obtaining uniform dispersion of whiskers/short fibers is difficult. SiC whiskers/short fibers are the most common type of reinforcement in UHTCs. But the thermal stability of the whiskers/short fibers is low [42] compared to SiC particles. In 2008, Zhang *et al.* [43] fabricated 20 vol.% SiC whiskers reinforced ZrB_2 composites by two different methods namely hot pressing(1800˚C) and Spark Plasma sintering(1600˚C). The hot pressed composites had bigger grains than the SPS sintered composites. In both cases the composites with SiC whiskers outplayed the monolithic ZrB_2 in strength and toughness. Toughening mechanism like crack deflection and whisker crack bridging was observed by SEM micrographs (Fig. 1.2). They reported the flexural strength to be >700 MPa and toughness to be >6 $MPam^{1/2}$ for both cases of composites which is significantly higher than other literature values reported monolithic ZrB_2 and ZrB_2-SiC composites.

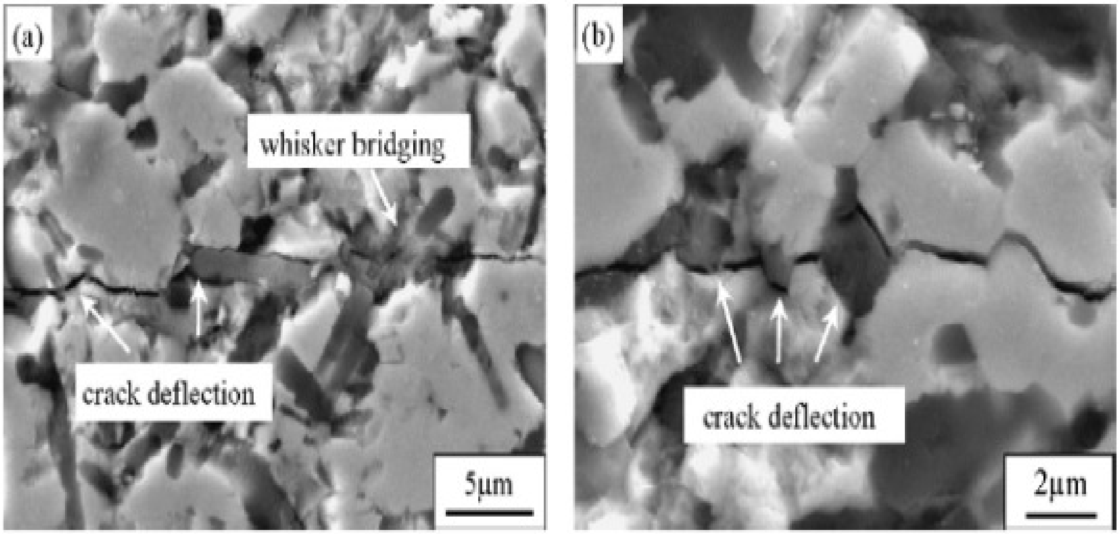

Fig. 1.2 Indentation induced crack propagation in hot pressed ZrB_2-SiC whisker composite showing (a) crack deflection and whisker bridging (b) crack deflection [43].

Later in 2009, Zhang *et al.* [44] consolidated 20 vol.% SiC whiskers reinforced ZrB_2 in the range of 1750 to 2000˚C by hot pressing. They reported that SiC whiskers was not stable at 1900˚C and degraded to SiC particles. They recommended the sintering temperature to be less that 1800˚C to retain the SiC whiskers in the matrix. The composites had better strength and toughness than the monolithic ceramic. In the same year Chen *et al.* [45] performed a comparative study between ZrB_2-$SiC_{particle}$, ZrB_2-$SiC_{whisker}$ and ZrB_2-SiCparticle-$SiC_{whisker}$ composites. The ZrB_2-$SiC_{particle}$-$SiC_{whisker}$ composites had better fracture toughness than ZrB_2 composites with just SiC particles or SiC whiskers. Guicciardi *et al.* [46] fabricated ZrB_2-Si_3N_4 composites by SPS with SiC whiskers and SiC chopped fibers as reinforcements. Both whisker and chopped fibers reinforced ceramics showed improvement in fracture toughness compared to their referral material (ZrB_2-Si_3N_4). However the chopped fiber reinforced composites had lower flexural strength compared to whisker reinforced composites. There are also few other studies on the effect of SiC whiskers/short fibers as reinforcements for the improvement of mechanical properties in UHTC composites [47-48]. The oxidation behavior of SiC particles, whiskers and short fibers in a ZrB_2 matrix was studied by L. Silvestroni and D. Sciti [37]. All the three composites showed similar weight gain and surface morphology (Fig. 1.3) after put under oxidation test. The fiber composites had better strength than the particle and whisker composites at 1200˚C. After oxidation all composites showed a low flexure strength of ~200 MPa (Fig 1.4).

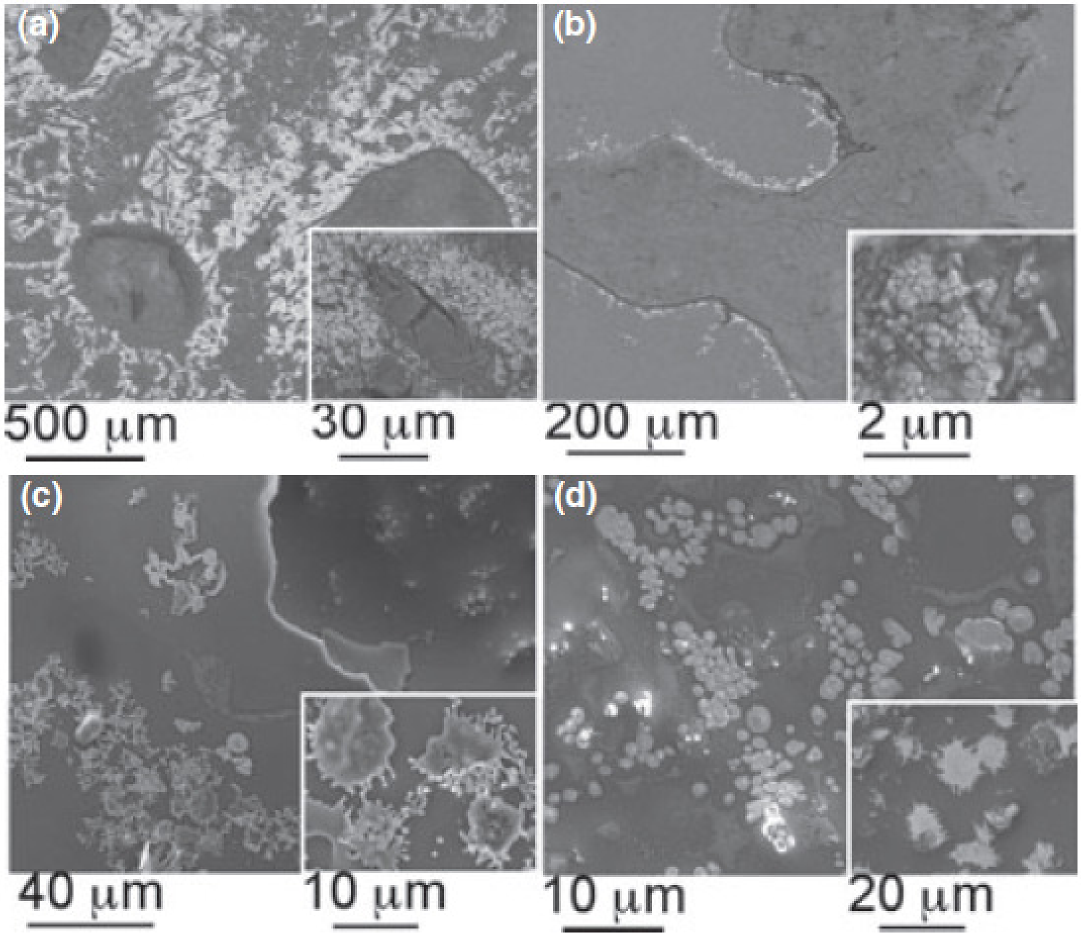

Fig. 1.3 Surface morphology of (a) 20% fiber (b) 20% whisker at 1200˚C and (c) 20% fiber (b) 20% whisker at 1700˚C [37].

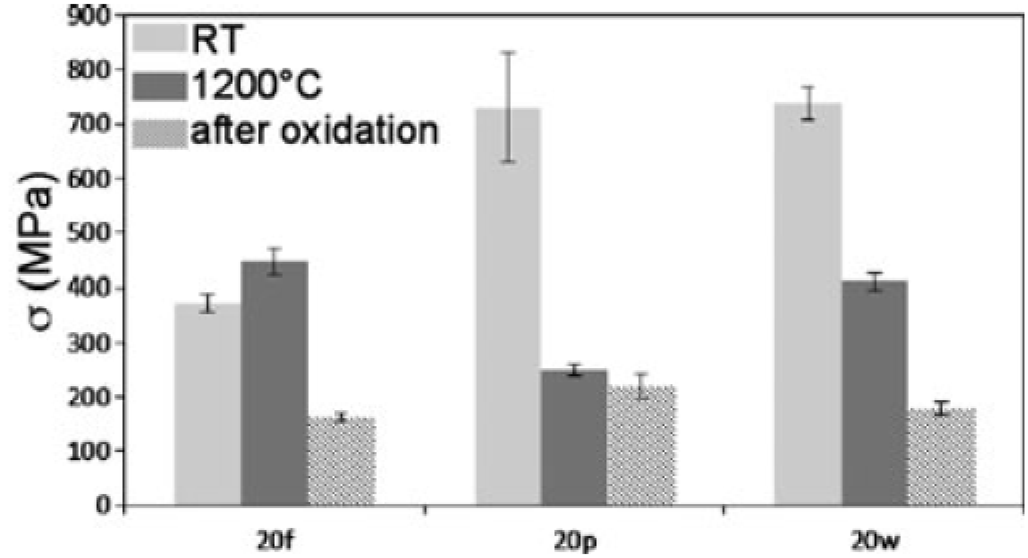

Fig. 1.4 Strength of ZrB_2 composites containing 20 vol.% of SiC fibers, particles and whiskers at room temperature, at 1200˚C and after oxidation at 1700˚C for 30 min [37].

1.3.1.2 Graphitic-Ceramic UHTC composite

The graphitic- ceramic UHTC composites can be classified into three types

(a) Carbon reinforced UHTC composites
(b) Graphene Nanoplatelets (GNP) reinforce UHTC composites
(c) Graphite reinforce UHTC composites
(d) Carbon Nanotubes (CNT) reinforced UHTC composites
(e) Carbon fiber reinforced UHTC composites

1.3.1.2.1 Carbon reinforced UHTC composites

Carbon is added as a sintering additive in the UHTC matrix. It also helps in removing the SiO_2 that is formed during sintering. Zhang *et al.* [40] studied the effect of carbon on densification and mechanical properties of ZrB_2. Based on their previous study [49] the stoichiometric amount of carbon required to eliminate SiO_2 is 2.8% wt of SiC content. However some amount of carbon was consumed by reactions with B_2O_3 or ZrO_2.

Therefore the amount of carbon required for full densification may be greater than 2.8 wt% of SiC. ZrB_2 composites with SiC, B4C (4 wt% of ZrB_2) and 2.8, 5, 7.3 and 10 wt% of resin derived C were pressurelessly sintered. The 2.8 wt% carbon with 30 vol.% SiC gave a relative density of 96.7 %, whereas the 5 and 10 wt% carbon composites were sintered to near full densification. The SEM analysis showed that for 7.3 and10 wt% C composites, there was excess carbon at the grain boundaries (Fig 1.5) and this lead to the reduction in flexural strength. The composites with 5 wt% carbon did not show residual carbon within their microstructure and they exhibited better flexural strength. Therefore they concluded that 5 wt% carbon was the optimum reinforcement content in ZrB_2 matrix for further studies.

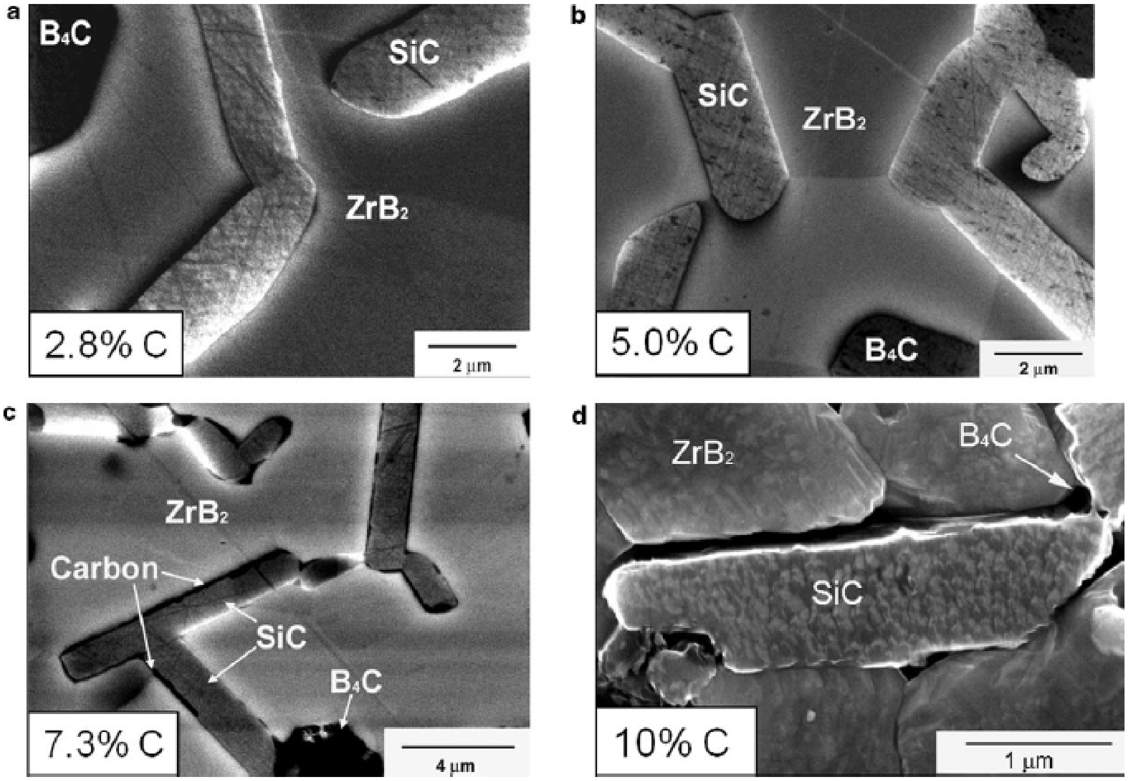

Fig. 1.5 SEM images of ZrB_2-30% SiC with (a) 2.8 wt% (b) 5 wt% (c) 7.3 wt% and (d) 10 wt% of carbon. (c) (d) shows excess carbon resulted in the formation of residual carbon at the ZrB_2/SiC grain boundaries [40].

1.3.1.2.2 Graphene Nanoplatelets (GNP) reinforce UHTC composites

Graphene is a single atom thick sheet of sp2 hybridized carbon atoms arranged in a honeycomb structure. It is the building block for other sp2 hybridized carbon forms like SWCNT and MWCNT. They exhibit outstanding mechanical (modulus and strength), electrical and thermal properties [50-55].These properties are also extended to bi- and few-layer graphene [56-58]. Unlike CNTs, a fairly uniform distribution of graphene is possible in the ceramic matrix under same processing conditions [59]. This makes graphene potential nano reinforcement for ceramic systems. Graphene platelets have been successfully used as nano reinforcement in several polymer and structural ceramic systems to enhance the mechanical, electrical and thermal properties [60-66]. But the study on graphene as a potential nano reinforcement for UHTC has not yet been carried out.

1.3.1.2.3 Graphite reinforce UHTC composites

Many layers of graphene stacked on top of each will give graphite. Graphite is added as reinforcement in UHTC to improve the fracture toughness and thermal shock resistance. In 2009 Wang *et al.* [67] studied the effect of graphite on the microstructure, mechanical properties and thermal shock resistance of ZrB_2-SiC composites. Composites with 10, 15, 20 and 30 vol.% of graphite was prepared by hot pressing at 1900˚C, 30 MPa for 1 hour. Relatively larger grains and lower relative density was noticed for the 20 and 30% graphite samples compared to 10 and 15% graphite samples. The flexural strength and fracture toughness also followed the same pattern as the 10 and 15% graphite samples exhibited better strength and toughness than the 20 and 30% composites. The decrease in strength of the 20 and 30% samples was attributed by larger grains and lower relative density. The improvement in fracture toughness for 10 and 15% composites was due to toughening mechanisms like crack deflection and branching, stress relaxation at the tip of crack and lower residual thermal stress. Fig 1.6 shows the SEM micrographs of the graphite samples showing graphite flakes, micro cracks and closed pores in the fracture surface. Later in 2011 Wang *et al.* [68] studied the impact of annealing on mechanical properties of the 15 vol.% graphite reinforced ZrB_2-SiC composites. The study indicates the optimum annealing parameters to be 1700˚C and 90 min, for which the samples showed improvement in hardness and strength and decrease in fracture toughness.

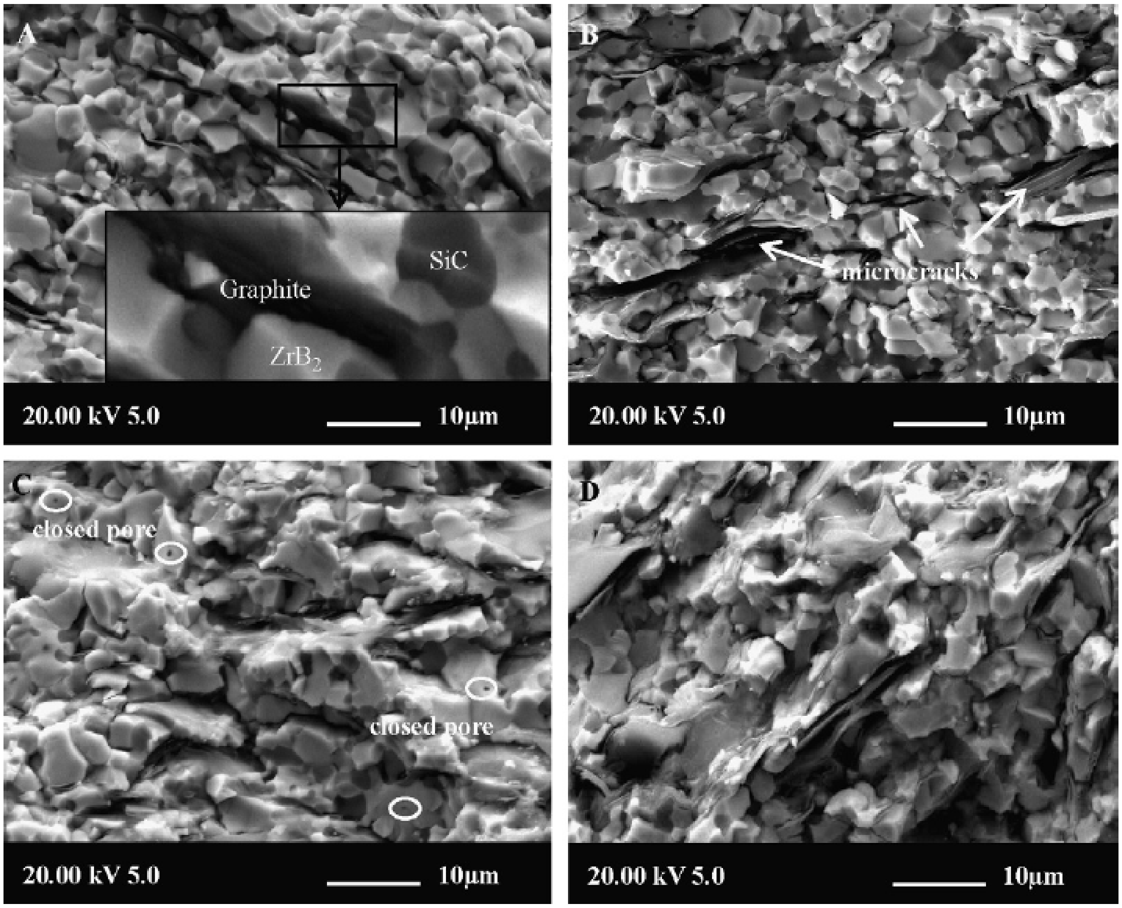

Fig. 1.6 SEM micro graphs of fracture surface (a) 10 vol.% (b) 15 vol.% (c) 20 vol.% (d) 30 vol.% graphite samples [67].

1.3.1.2.4 Carbon nanotubes (CNT) reinforced UHTC composites

Carbon nanotubes are formed by seam-less rolling up of graphene sheets. When a monolayer of graphene is rolled up it forms single-wall carbon nanotube. By adding one more layer of concentric cylinder will give double-wall carbon nanotube and rolling-up multiple layers of graphene layers into concentric cylinders will give multi-wall carbon nanotube. Their high aspect ratio makes them represent one dimensional system [61]. CNTs became exciting field of research due to their interesting physical properties and applications. They possess extraordinary mechanical properties like high Young's modulus (1000 GPa) and high tensile strength (75 GPa) and they also exhibit exceptional electrical and thermal properties making them ideal reinforcements for ceramic matrix [70-74]. CNTs have been successfully used as reinforcements in structural ceramics like alumina and silicon nitride [75-80]. CNTs enhanced the fracture toughness of the composites through a range of toughening mechanisms like CNT pull-outs, crack bridging, and crack deflection. While the toughening effects of CNT reinforcement in structural ceramics are now well established, these effects are not well investigated for UHTC ceramics. Tian *et al.* [81] fabricated ZrB_2-SiC composites with and without CNT by hot pressing (1900˚C for 1 hour). The significance of their work will be discussed in the review of Zirconium diboride based UHTC composites section.

1.3.1.2.5 Carbon fiber reinforced UHTC composites

Short carbon fibers are used as reinforcements in UHTC matrix because of their low cost and ease of fabrication. They enhance the strength and toughness of the composites by conventional fiber mechanisms like crack deflection, fiber pull-out and fiber debonding. Yang *et al.* [82] fabricated ZrB_2-20 vol.% SiC composites with and without 20 vol.%

short carbon fibers at 2000°C, 30 MPa for 30 1 hour by hot pressing. They reported an increase of 54% in fracture toughness of the composite with short fiber when compared with the composite without short fibers. This increase in fracture toughness was due to toughening mechanisms like crack deflection, fiber debonding, fiber fracture and fiber pull-out (Fig 1.7). However they also noticed a reduction in flexural strength of the composite with short fibers. This reduction in strength was attributed by graphitization of the fiber at the fiber matrix interface [82-83].

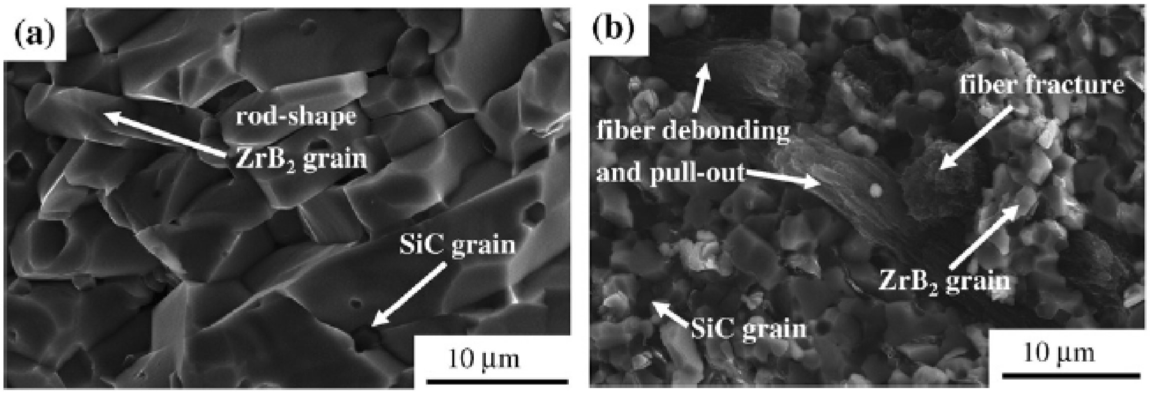

Fig. 1.7 SEM micrographs showing fracture surface of (a) ZrB_2- 20 vol.% SiC composite (b) ZrB_2-20 vol.% SiC-20 vol.% short carbon fiber [82].

1.4 Family of UHTC

The family of UHTC predominantly consists of transition metal diborides, carbides and nitrides. Some of the commonly studied UHTCs are ZrB_2, ZrC, ZrN, HfB_2, HfC, HfN, TaB_2, TaC, TaN, TiB_2, TiC, TiN and SiC. Reinforcements are added to these UHTCs for better densification and enhanced mechanical, electrical, thermal and oxidation properties as explained in section 1.3.1. The various investigations on some of these UHTCs are explained in detail in the following sections.

1.4.1 Zirconium diboride based UHTC composites

Detailed investigation on ZrB2 based UHTCs is presented in the Review of Zirconium diboride based UHTC composites section.

1.4.2 Hafnium diboride based UHTC composites

Hafnium diboride is one of the promising ceramic of the UHTC family. HfB_2 has the best oxidation resistance among the UHTC ceramics and a lot of studies have been made on the improvement of mechanical and oxidation properties of HfB_2. Extensive research on SiC reinforced HfB_2 composites was carried out by F. Monteverde [23-25,84-86] and silicides based HfB_2 composites was studied by Scitti *et al.* [87-88]. There are also other significant works done on HfB_2 based UHTC composites [89-91]. F. Monteverde consolidated HfB_2-SiC composites by reactive hot pressing at 1900˚C full densification were achieved [23]. He reported a significant improvement in mechanical properties like micro hardness (~19 GPa), Young's Modulus (520 GPa) and strength (770 MPa) due to SiC reinforcement. He also conducted oxidation testing of the composite at 1700˚C for 20 hours. There was no significant mass gain due to oxidation and the microstructure remained the same. The refractoriness of HfB_2 and SiC lead to this good thermal stability. In 2006 Monteverde *et al.* [24] fabricated HfB_2- 30 vol.% SiC by spark plasma sintering at 2100˚C. The fracture toughness and flexural strength remained almost the same at room temperature and at 1500˚C. The retained mechanical properties at high temperature were attributed by the depletion of secondary phases at grain boundaries. Later in 2007 F.

Monteverde performed a comparative study on HfB_2- 30 vol.% SiC composited sintered by spark plasma sintering (SPS) at 2100˚C for 3 min and by hot pressing (HP) at 1900˚C for 35 min [25]. The average grain size of SPS sintered samples was greater than the HP samples as shown in Fig 1.8.

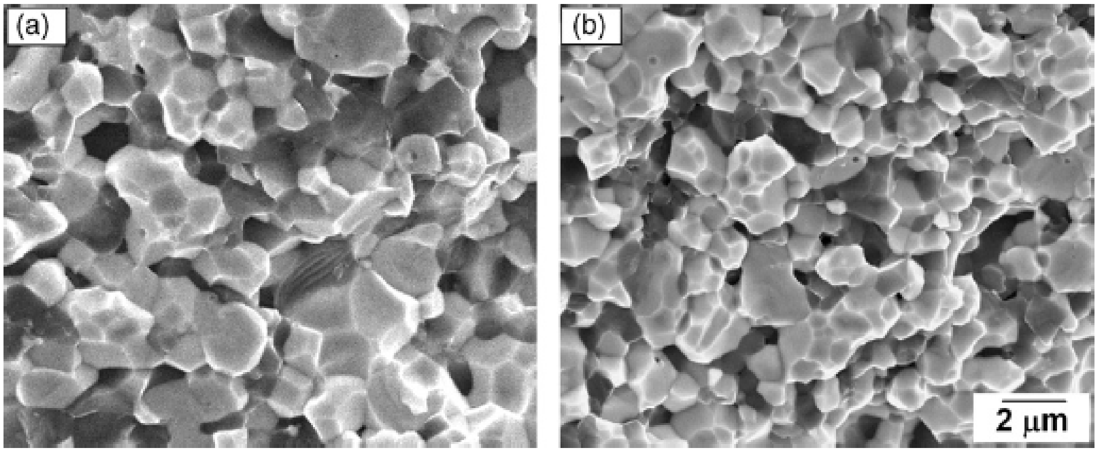

Fig. 1.8 SEM micrograph from fractured surface (a) SPS sample (b) HP sample [25].

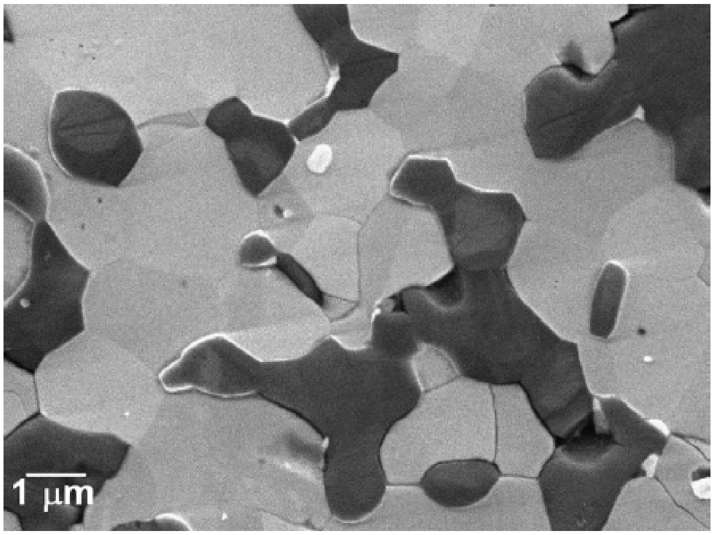

Fig. 1.9 SEM micrograph showing micro cracks on polished SPS sample [25].

The Hot pressed samples had better flexural strength than the SPS samples (665 MPa for HP and 465 MPa for SPS samples). The SPS samples also showed premature failure during flexural test. This was due to the thermal shock produced by rapid cooling rate of SPS (500° C/min) leading to the formation of micro-cracks (Fig 1.9) in the samples. However the SPS samples had better fracture toughness than the HP samples due to this strained configuration. Sciti *et al.* fabricated HfB_2 composites with 3 vol% silicided of molybdenum and tantalum as sintering additives by spark plasma sintering. $MoSi_2$ was a better sintering additive than $TaSi_2$ giving better relative density at same sintering parameters. They calculated the flexural strength at room temperature, at 1200˚C and at 1500 ˚C. In all the cased the $MoSi_2$ samples had better strength than the $TaSi_2$ sample. A number studies [23, 85-86, 89] on the oxidation properties of HfB_2 was conducted and the studies show that HfB_2 has good oxidation resistance much attributed by its refractoriness and also the protective oxide layers formed due to reinforcements like SiC.

1.4.3 Zirconium carbide based UHTC composites

Zirconium carbide (ZrC) is a UHTC with a melting point of 3400˚C and is used in field emitters and nuclear particle fuels. Sciti *et al.* fabricated ZrC composites in temperature range of 1750-2100˚C by spark plasma sintering with $MoSi_2$ as sintering additive [92]. Composites with 1, 3 and 9 vol.% of $MoSi_2$ were prepared and put under mechanical testing. All the composites gave near full density. Hardness, fracture toughness and flexural strength improved compared to monolithic ZrC. Densification and thermal expansion mismatch between ZrC and $MoSi_2$ was attributed to the increase in strength and fracture toughness. In 2011 Zhao *et al.* [93] consolidated ZrC- SiC composites by spark plasma sintering at 1800˚C. A maximum relative density of ~96% was obtained for the composites. The composites had better hardness, strength and fracture toughness than the monolithic ZrC samples. The improvement in mechanical properties was due to better relative density, refined microstructure, formation of intergranular structure and thermal mismatch between SiC and ZrC.

1.4.4 Hafnium carbide based UHTC composites

Hafnium carbide (HfC) has the highest melting point of 3900˚C among the UHTCs. This very high melting point makes it difficult to sinter. Therefore there is not much investigations made on the consolidation of HfC. In 2004 A. Sayir consolidated carbon fiber reinforced HfC [94]. He also try to consolidate TaC reinforced HfC. But the TaC reinforced HfC did not have a refined microstructure and also lacked toughening mechanisms. The carbon fiber reinforced HfC had better toughening and failure mechanism attributed to the pyrolytic graphite interface between carbon fibers and HfC ceramic matrix. Later in 2011 Silvestroni *et al.* [95] performed a comparative study on HfC and TaC based composites consolidated by hot pressing at 1900˚C for 5 to 20 min. 5 vol.% of $MoSi_2$ was added as sintering additive. All the composites had relative density greater than 95% whereas the monolithic samples had an average density of 85-90%. The composites had better mechanical properties than the monoliths. The improvement in strength and toughness was attributed to better density and microstructure.

1.4.5 Tantalam carbide based UHTC composites

Tantalam carbide is a UHTC that is gaining attention in recent years as a potential high temperature ceramic. A number of studies have been made on the fabrication of TaC with different sintering additives and reinforcements [95-99]. In 2010 Khaleghi *et al.* consolidated TaC by SPS and HP in a temperature range of 1900-2400˚C and studied the microstructure, hardness and strength of the samples. The grain growth helped in densification of the samples but not improved strength. In order to limit the grain growth they added CNT as reinforcement. Addition of CNT improved the strength but had no impact on the microstructure of the samples. They also concluded that SPS was a better sintering mechanism than HP because of its rapid heating rate and less holding time. Later in 2011, Bakshi *et al.* [97] consolidated TaC by SPS with 1 wt.% B_4C ad sintering additive at 1850˚C at different pressures of 100 255 and 363 MPa. There was increase in grain size with increase in temperature. But the addition of B_4C acted as grain growth inhibitor. It also improved the relative density, hardness and toughness of the composite. The improvement in properties was attributed to refined microstructure. Later in the same year Bakshi *et al.* studied the effect of carbon nanotube (4 wt.%) reinforcement in TaC and its impact on the densification and mechanical properties [98]. The pressure (100, 255, 363 MPa) and lengths of carbon nanotubes (long 10-20, short 1-3 μm) were varied and its impact on the properties was analyzed. The short CNTs enabled better densification at 100 MPa than the longer CNTs, whereas the longer CNTs were better grain growth inhibitors. The longer CNTs also proved to be a better toughening reinforcement than their shorter counterparts. The fracture toughness increase for about

60% in the long CNT reinforced TaC composites SPS sintered at 363 MPa. Raman spectroscopy, SEM and TEM was carried out and the study indicated that CNTs are converting to graphite flakes at more than 100 MPa pressure. The short CNTs underwent more damage than the long CNTs. This was the reason for the long CNTs to out play the short CNTs in toughening of the composite. Fig 1.10 and 1.11 shows the SEM images of CNTs on the fracture surface of TaC-CNT composites sintered at 100 MPa.

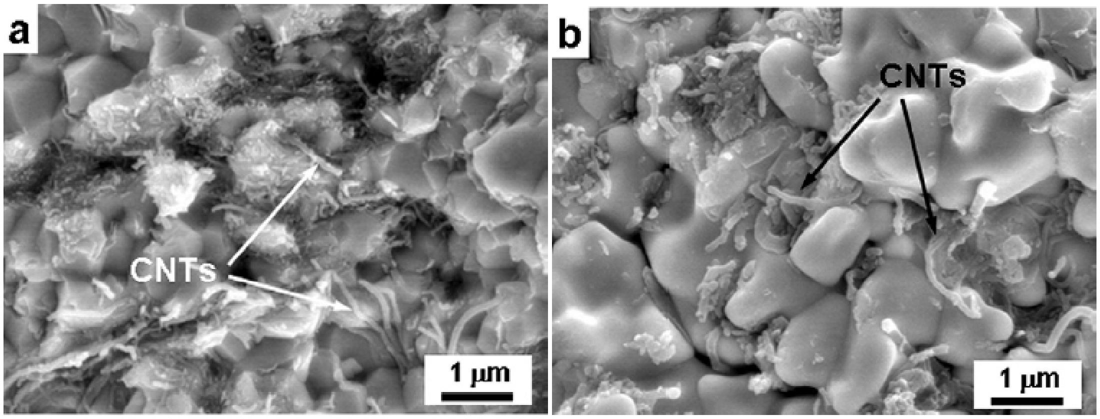

Fig. 1.10 SEM micrographs from fracture surface of (a) TaC-long CNT (b) TaC-short CNT sintered at 100 MPa [98].

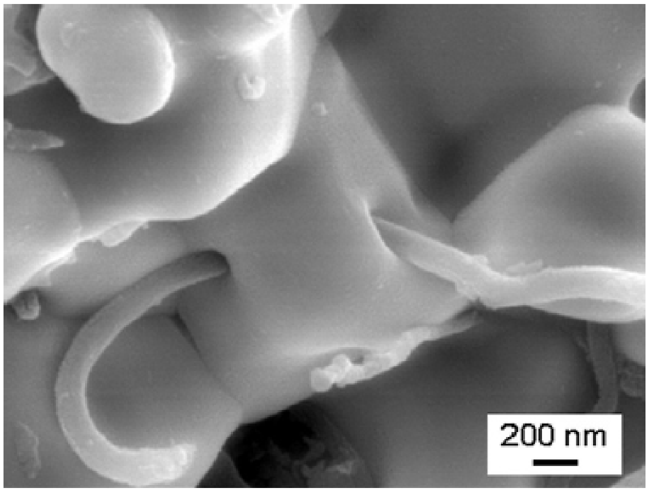

Fig. 1.11 High magnification SEM image showing molten TaC encapsulating short CNT sintered at 100 MPa [98].

1.5 Processing of UHTC composites

Full densification is important to obtain better mechanical and thermal properties. Fabrication of UHTCs to full densification needs very high temperature and pressure with large holding time. Let us see some of the common sintering mechanisms used to produce UHTC composites.

(a) Hot pressing

(b) Reactive hot pressing

(c) Pressureless sintering

(d) Spark plasma sintering

1.5.1 Hot pressing

Hot pressing (HP) is the most common consolidation mechanism followed to sinter UHTC composites. It is a powder metallurgy process where the ceramic powder is heated to high temperate in the range of ~1800 to 2400 ˚C under moderate uniaxial pressure of ~ 20 to 40 MPa with holding time varying from 30 to 60 min is used to produce fully dense samples where densification is a diffusion controlled rate process. A number of studies have been done on the fabrication of fully dense UHTC composites [7,19,32]. Due to this high processing temperature and long holding time undesired microstructural features like grain growth, strong interfacial bonding between the reinforcements and ceramic matrix and disintegration of nano reinforcements are observed in HP UHTC composites. These features will deteriorate the mechanical and thermal properties of the UHTCs.

Tian *et al.* [81] fabricated CNT reinforced ZrB_2-SiC composites by HP at 1900 under 30 MPa for 1 hour. This high temperature for long holding time of 1 hour led to the disintegration of CNTs and also created strong interfacial bonding between CNT and the ceramic matrix which lead to insignificant improvement in the mechanical and thermal properties of the composites.

1.5.2 Reactive Hot pressing

Reactive hot pressing (RHP) is a processing method to produce dense UHTC composites with less impurities and lower processing temperature. The consolidation mechanism of RHP involves two stages namely the in-situ reaction of the starting particles and the densification process itself. The in-situ reaction and densification of the composites takes place simultaneously under the applied temperature and pressure. RHP has been successfully used to consolidate dense UHTC composites at low temperature [20, 101].

Chamberlain *et al.* [20] used RHP to fabricated ZrB_2-SiC composites to relatively density greater than 95% at a relatively low temperature of 1650˚C. Nano sized elemental zirconium and boron was used as starting particles along with SiC as reinforcement and B_4C as sintering additive. The composite powder was heated in RHP for 360 min at 600˚C with a heating rate of 10/min. Zr reacted with B to form ZrB_2. Later the powder was heated to 1000 ˚C and 1450˚C with holding time of 60 min. Then the composite was heated to 1650˚C with 40 MPa pressure for 30 min to obtain dense composite samples.

1.5.3 Spark Plasma Sintering

Spark plasma sintering (SPS) is a new consolidation technique for ceramics that uses high pulsed direct current and uniaxial pressure to densify the materials. Rapid heating and cooling rates with low holding time usually in few minutes to densify ceramics makes SPS an interesting consolidation mechanism. Rapid heating rates and low holding time ensures no or insignificant grain growth and ensures the survival of nano reinforcements.

Wu *et al.* [101] carried out a comparative study on the consolidation of ZrB_2-SiC composites by reactive hot pressing and spark plasma sintering. For the same processing temperature of 1800˚C, RHP with a heating rate of 10˚C/min needed 60 min to produce dense samples, whereas SPS with a heating rate of 100˚C/min needed only 5 min to sinter fully dense samples. The SPS sintered samples had a more homogeneous and fine microstructure than RHP samples due to the rapid heating rate and low holding time.

The SPS consolidation mechanism and the effect of various processing on the densification, microstructure and properties of UHTC composites is discussed in detail in later section.

1.5.4 Pressureless sintering

New processing technique where sintering aids are added to the UHTC composites for Pressureless sintering to near full densification. Usually two types of sintering aids are added to the composite to facilitate densification. They are liquid phase formers and reactive agents. The liquid phase formers are usually silicides of transition metals. $MoSi_2$ and $TaSi_2$ [87-88] are the commonly used liquid phase formers for the consolidation of ZrB_2 and HfB_2 ceramic composites. These sintering additives melt to form liquid phase which reacts with the metallic element of the ceramic by replacing its atom with the additive atom reducing the lattice size. This lattice contraction will change the surface energy of the ceramic allowing it to increase the driving energy to densify at lower temperature with minimal or no external pressure.

The reactive agents are elements or compounds that react and eliminate the oxide impurities present in the composite powder. The presence of oxide impurities does not favor the densification mechanism. Therefore reactive elements like C, B_4C and WC are added to the ceramic composites to react and eliminate the oxides by forming compounds and facilitate densification without or with less external pressure. Zhang *et al.* [49] fabricated ZrB_2 by pressureless sintering at temperature as low as 1850˚C. B_4C and WC were added as sintering additive to eliminate the ZrO_2 oxide impurity to enable this low temperature pressureless sintering.

1.6 Spark Plasma Sintering

As explained in section 1.5.3 SPS is a novel sintering mechanism involving the passage of high pulsed direct current into the ceramic powder under uniaxial pressure for holding time of few minutes to consolidate the material. Nanocrystalline metals/alloys, nano structured ceramics, bulk metallic glasses and intermetallic materials can be sintered by spark plasma sintering. SPS enables near full densification of UHTC and other ceramic composites without significant grain growth. It is also reported that SPS sintered samples better mechanical and thermoelectric properties by producing samples with cleaner grain boundaries, improved bonding quality and homogeneous and finer microstructure [100-102]. In this section the densification mechanism and the effect of various processing parameters on the densification involved in SPS is discussed.

1.6.1 SPS Working Mechanism

Monolithic or composite ceramic powder is placed inside graphite die, punch and spacers arrangement. The entire arrangement is placed in between the two electrodes of SPS inside a sealed vacuum chamber. Pulsed direct current is passed through the powder matrix by the electrodes, spacers and punch assembly while simultaneous uniaxial pressure is applied through the upper electrode with the help of a hydraulic system. The schematic representation on the SPS chamber assembly and the graphite die, punch, spacer and sample assembly is shown in fig 1.12 (a) and (b) respectively.

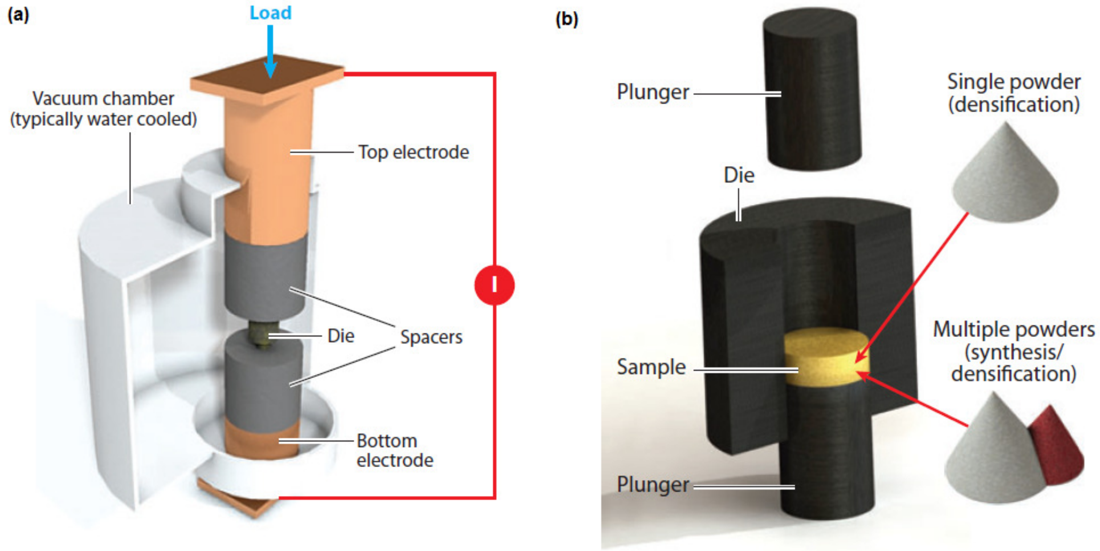

Fig. 1.12 Schematic representation of SPS (a) chamber assembly and (b) graphite die, punches, spacers and sample assembly [102].

1.6.2 SPS Densification Mechanism

Densification of powder matrix in SPS is obtained by the elimination of inter and intra particles pores and sintering the compact by mass transfer mechanism. The densification mechanism takes place in two different forms. The first form of densification is the rearrangement of particles to remove porosity of the powder matrix which is directly influenced by the applied sintering pressure. The second form is the actual sintering process where the curvature of the particles is reduced by applied temperature and simultaneous pressure causing a reduction in surface energy which drives the sintering mechanism. The ON-OFF DC pulsed current induces joule heating in the powder particles and also discharges sparks in the gaps and contact area between the particles. This spark production creates very high localized temperature leading to the evaporation and subsequent solidification causing surface diffusion on the surface of the particles. This evaporation and melting on the surface of the particles produces necking of the particles leading to volume diffusion. Particles form several necks with the adjacent particles leading to the expansion of necks. Finally the expansion of necks is formed into grain boundaries by plastic deformation. Thus the entire mass transfer involved in SPS sintering can be divided into four processes namely

- Vaporization and solidification
- Surface diffusion
- Volume diffusion
- Grain boundary diffusion

There are other densification mechanisms that can take place during sintering. They can be classified into thermal and non-thermal effects. The thermal effects will include the mismatch in thermal conductivity creating thermal stress leading to dislocation creep, highly non-uniform local temperature leading to melting of particle and high local temperature gradient leading to thermal diffusion. The non-thermal densification factors include electroplasticity and dielectric breakdown of oxide films that provide the cleansing effect on particles improving densification [101-102].

The exact densification mechanism of SPS is still under debate but Joule heating is widely accepted as the densification mechanism in SPS [100-102]. The pulsed direct current that passes through the monolithic/composite powder will generate high temperate by joule heating. Sparks are discharged in the gaps between the powder particles. These sparks further increases the temperature of the compact powder leading to necking and mass transfer induced densification. Localized joule heating and spark production (fig 1.13) enables sintering of materials at a lower temperature and faster rate than other conventional sintering processes. Thus the high temperature produced by the ON-OFF DC pulsed current and simultaneously uniaxial pressure is applied on the powder enables consolidation of the material to near theoretical density. Even though the process is called spark plasma sintering, a recent study indicated that there is no formation of plasma during the sintering process [100].

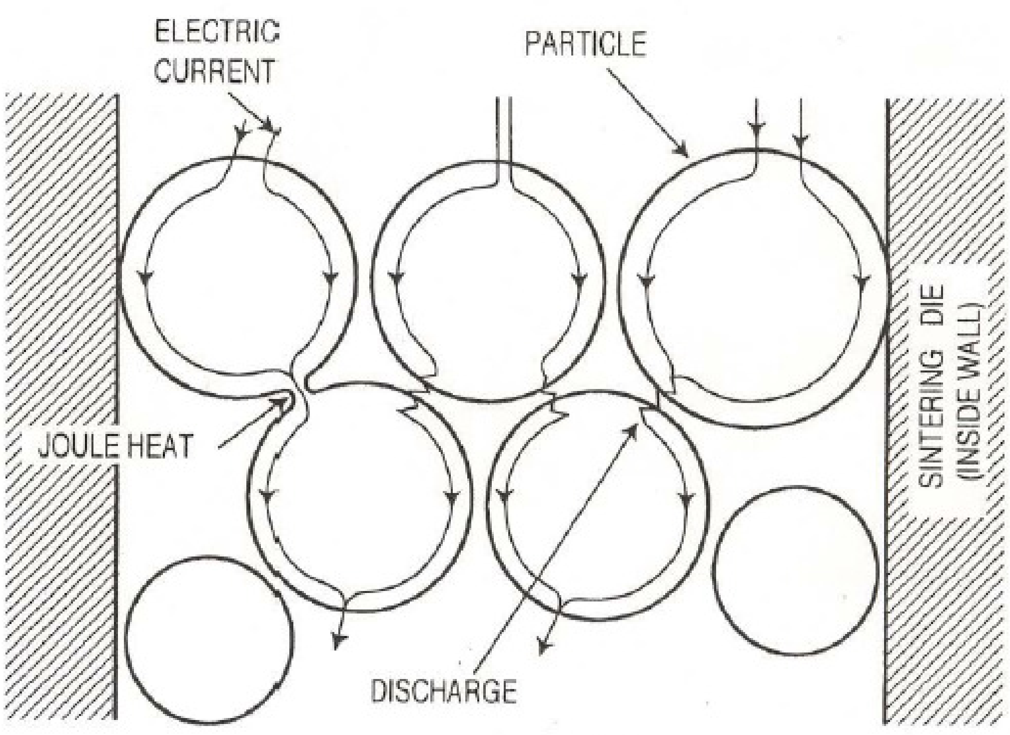

Fig. 1.13 Schematic representation of SPS densification mechanism indicating the Joule heating of particles by pulsed DC and sparks discharge in the gaps between particles [101].

1.6.3 SPS parameters and effect on densification

SPS processing parameters play an important role in the densification, microstructure, mechanical and thermoelectric properties of the sintered material. The various SPS processing parameters are heating rate, maximum hold temperature, cooling rate, pressure application rate, maximum hold pressure and pressure removal rate indicated by numbers 1 to 6 in figure 1.14. The DC current is switched on at the start of heating cycle and switched off at the end of soaking/holding time. Densification and grain growth occur simultaneously in SPS. Therefore selecting the optimum SPS parameters is critical in obtaining good densification. The effect of temperature, heating rate, pressure rate, hold pressure and applied direct current on the densification of the material is discussed in detail in this section.

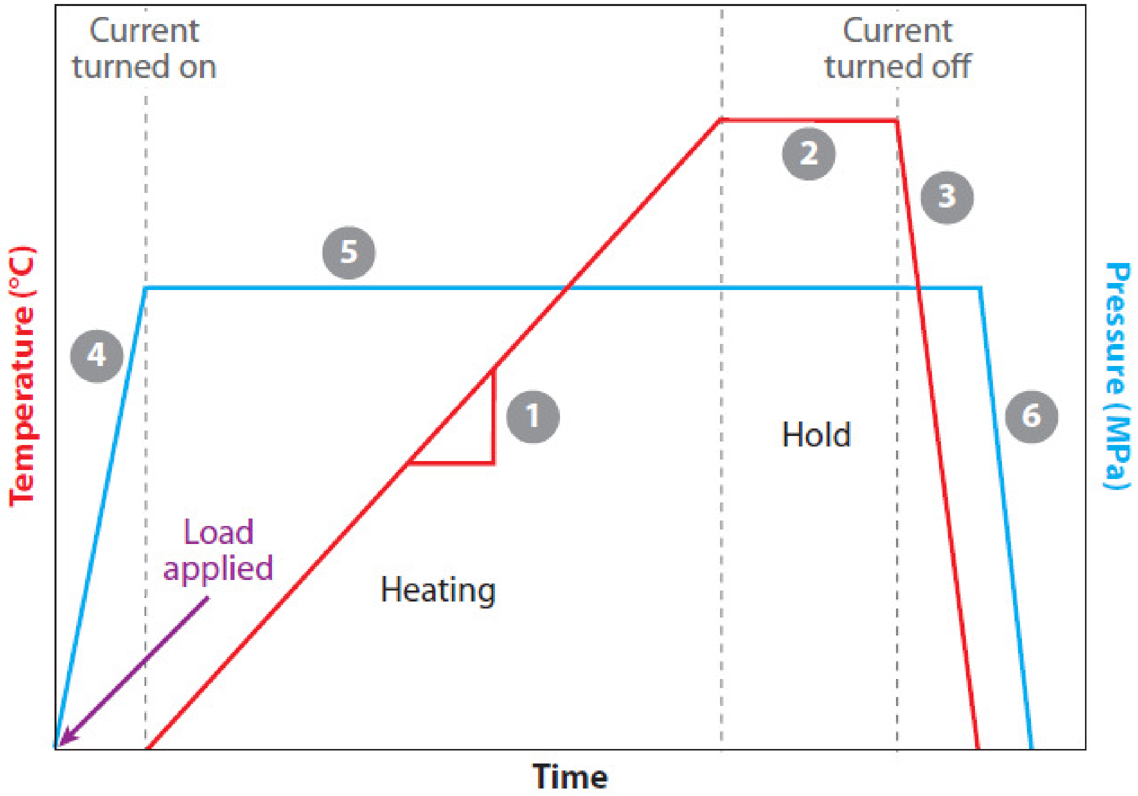

Fig. 1.14 Spark Plasma Sintering processing parameters as a function of time [102].

1.6.3.1 Heating Rate

Heating rate is one of the important parameters of SPS that impacts the grain size and densification of materials. Usually SPS heating rate varies between 100 to 600˚C/min. High heating rates helps in obtaining fine microstructure by inhibiting significant grain growth. A number of studies have been done on the impact of heating rate on the densification and microstructure of UHTC by SPS [106-107]. Guo *et al.* fabricated ZrB_2 by spark plasma sintering and studied the effect of temperature, heating rate and holding time on the densification and microstructure of the samples [106]. The study concluded that 200˚C/min was the optimum heating rate for ZrB_2. A heating rate below that resulted in the coarsening of the grains which in turn deteriorate the mechanical properties of the samples.

1.6.3.2 Temperature

The sintering temperature is selected based on the melting point temperature (Tm) of the material to be sintered. Usually around half of the melting temperature is selected as sintering temperature since most of the materials densify around 0.5 of Tm. The source of heat production is from the joule heating produced by the pulsed direct current. The heat generation rate q is given by

$$q = JE \text{ ………………………………………...(1.1)}$$

where J and E are current density and electric field respectively. A linear curve fit relationship between sintering temperature and relative density was obtained by Garay [102]. The relation is given by

$$\rho = s\left(\frac{T}{Tm}\right) + b\text{……………………………………..(1.2)}$$

where ρ is the relative density, T is the sintering temperature, Tm is the melting temperature of the material, b is the intercept on the density axis and s is the slope called as temperature sensitivity of the material. A high s value indicates high temperature dependence of material for densification.

1.6.3.3 Pressure

Simultaneous application of pressure along with temperature improves the sinterability and leads to better densification of the material. In the earlier stages of sintering pressure helps in the rearrangement of the particles to obtain a compact powder and also clearing of agglomerates. This helps in eliminating some porosity in initial stages of sintering. In later stages of sintering, the applied pressure helps in the densification of the material by impacting the driving force of sintering. The driving force of sintering is given by [100]

$$\frac{d\rho}{(1-\rho)dt} = B(g\frac{\gamma}{x} + P)\ldots\ldots\ldots\ldots\ldots\ldots\ldots\ldots\ldots\ldots\ldots\ldots\ldots(1.3)$$

where ρ is fractional density, t is time, B consists of diffusion coefficient and temperature, g is geometric constant, γ is surface energy, x is particle size and P is the applied pressure. B is the driving force for sintering and the second term along with B is the effect of applied pressure on the driving force.

1.6.3.4 Pressure Rate

The rate of pressure applied can be controlled in SPS. The impact of rate of pressure on densification has not been clearly understood. This is because of the lack of studies on the impact of SPS pressure rate on densification. Xu *et al.* [103] studied the effect of pressure rate on the densification of zirconia and reported that the rate of densification improved with increase in rate of applied pressure. Anyhow more study is needed to establish a relationship between pressure rate and densification.

1.6.3.5 Pulsed Direct Current

The application of pulsed direct current to sinter samples makes SPS unique and interesting from other conventional sintering mechanisms. Even though the exact sintering mechanism behind SPS is under debate, Joule heating and discharge of speaks between the gaps of particle is said to produce large temperature enabling the sintering process. The impact of pulse variation on the densification of materials has been studied [104-105]. The studies indicate that the variation in the pulse rate did not have any significant impact on the densification of materials by SPS. But there was a decrease in reaction rate under the absence of pulsed current in case of in-situ SPS [105].

1.7 Zirconium diboride based UHTC composites: A review

Zirconium diboride is one of the promising UHTC with a melting point of 3245°C and excellent oxidation resistance. A large number of studies have been done on the densification, mechanical and thermal properties, oxidation resistance and the effect of various reinforcements on these properties. The various processing methods and the content and type of reinforcements on the densification and properties of ZrB_2 composites have been presented in this section.

1.7.1 SiC reinforced ZrB_2 ceramic composite

Silicon carbide particles [19-20, 27, 31, 40, 106-116] and silicon carbide whiskers [42-48] are the most common reinforcement type used in ZrB_2 ceramic matrix. The addition of silicon carbide acts as grain growth inhibitor and improves the mechanical properties of the composite. It also improves the oxidation resistance of the composite by the formation of glassy SiO_2 a passive oxidation layer on the surface of the ceramic at elevated temperatures. Since we have discussed the effect of SiC whiskers on the microstructure, mechanical and oxidation properties of ZrB_2 composites in section 1.3.1.1.2, we will concentrate more on SiC particles as potential reinforcement in this section.

In 2004 Chamberlain *et al.* [19] fabricated ZrB_2 with 10, 20 and 30 vol.% SiC by hot pressing at 1900˚C under a uniaxial pressure of 32 MPa for 45 min. The composite powders were prepared by attrition milling in tungsten carbide (WC) media and spindle for 2 hours with hexane before they were hot pressed. This extensive milling led to WC contamination in the composites which was identified by SEM and XRD. There was also an unidentified phase present in the composites. The monolith, 20 and 30 vol.% SiC composites had a relative density >99% whereas the the 10% SiC composite had a relatively low density of ~93%. The composites had better refined and smaller grains compared to monolithic ZrB_2. The average grain size for ZrB_2 was ~6 μm whereas the composites had an average grain size of ~3μm (Fig 1.15).The reinforced SIC particles acted as grain growth inhibitors. The young's modulus and mechanical properties like hardness (Vicker's indentation), flexural strength (four point bend test) and fracture toughness (four point bending test after Vicker's indentation) were measured. The hardness and elastic modulus of the composites did not change compared to the monolith, but the strength and toughness of the composites improved. The 20 and 30% SiC composites had flexural strength greater than 1000 MPa compared to the 565 MPa strength of ZrB_2. This large improvement in strength was attributed to decreased grain size as well as the presence of WC in the composites. The fracture toughness also improved for the composites from 3.5 for ZrB_2 to 5.3 MPa.m$^{1/2}$ for 30% SiC composite.

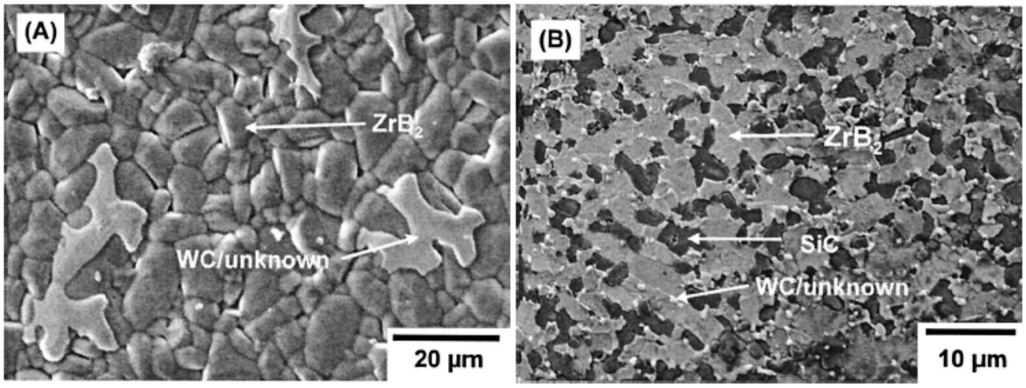

Fig. 1.15 SEM micrograph from fracture surface of (a) ZrB_2 showing grains of ~6µm (b) ZrB_2-30 vol.% SiC composite showing grains of ~3µm. The SEM also shows the presence of WC and an unknown phase present in the samples [19].

Later in 2006, Chamberlain *et al.* [20] carried out low-temperature sintering of ZrB_2-SiC by reactive hot pressing. ZrB_2 nano powder was formed by elemental mixing of Zr and B by attrition milling below 600˚C. ZrB_2- 30 vol.%SiC composites with relative density greater than 95% was produced at a low temperature of 1650˚C. Composites were also sintered at 1800˚C to make a comparative study. The 1800˚C sintered samples had a relative density of around 99%. B_4C was added in small quantities to eliminate ZrO_2 produced during sintering. Due to the low temperature sintering the composites had a very low grain size of 0.5 µm for 1650˚C samples and 1.5 µm for 1800˚C samples (Fig 1.16). The hardness, flexural strength and fracture toughness of the samples was measured. The 1800˚C samples had better mechanical properties than the 1650˚C samples. This is due to presence of distributed porosity in the 1650˚C composites and the better densification caused small grain growth in the 1800˚C composites leading to better properties.

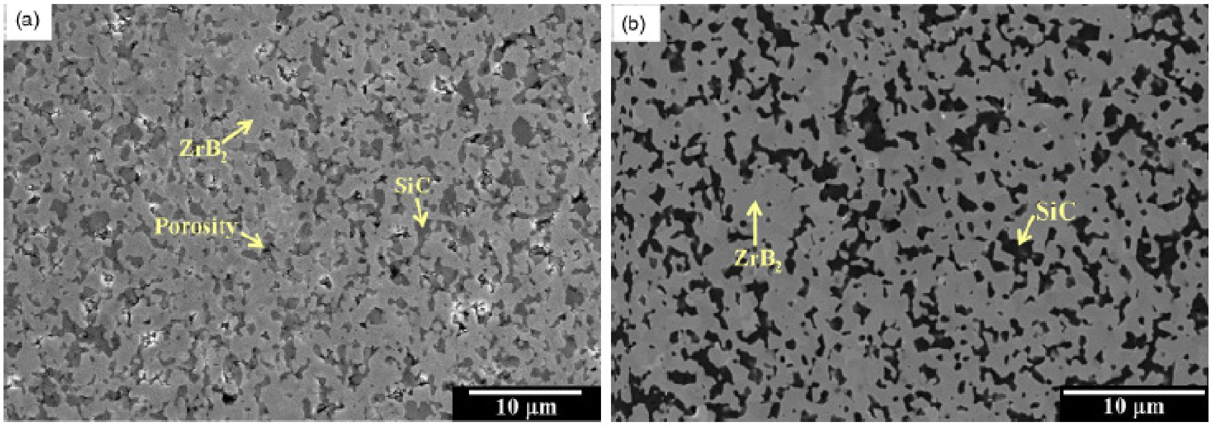

Fig. 1.16 SEM micrographs from polished surface of (a) ZrB_2-30% SiC sintered at 1650˚C showing distributed porosity and grain size 0.5 µm (b) ZrB_2-30% SiC sintered at 1800˚C showing dense microstructure and grain size 1.5 µm [20].

In 2007, Wu *et al.* [109] carried out a systematic study on the densification and microstructure of reactive hot pressed (at 1800˚C with a heating rate 10˚C per min and a holding time of 60 min under 20 MPa pressure) and spark plasma sintered (at 1800˚C with a heating rate 100˚C per min and a holding time of 5 min under 50 MPa pressure) ZrB_2-SiC composites. They also prepared other combination of composites like ZrB_2-SiC-ZrC, ZrB_2-SiC-ZrN and ZrB_2-SiC-AlN and carried out similar studies. The reactive hot pressed samples had a better density than the SPS sintered samples in case of ZrB_2-SiC composites. But the SPS sintered samples had homogeneous and finer microstructure (< 5 µm) which was attributed by rapid heating rate and smaller holding time. Whereas the RHP samples had courser microstructure (5-10 µm) caused by slow heating rate and longer holding time.

Akin *et al.* fabricated SiC particles reinforced ZrB_2 ceramic composite by spark plasma sintering [27]. 20-60 mass% SiC samples were sintered at various temperatures varying between 1800˚C to 2400˚C and a holding time of 180 to 300 s and 20 MPa pressure. For samples sintered above 2100˚C, there was no holding time with 10 MPa pressure. All the composites had near full density. The micro structural study showed that for samples sintered below 2120˚C equiaxed grains of 2-5 µm for ZrB2 and 2-4 µm for SiC were formed which can be seen in Fig 1.17 (a) and (b). But for temperatures above that, the SiC grains changed morphology from equiaxed to elongated grain structure with a width of 1-3 µm and length of 3-6 µm as seen in fig 1.17 (c). The hardness and fracture toughness of the composites was evaluated using a microhardness tester. The hardness and fracture toughness of the composites increased with increase in SiC content till 50% of SiC attributed to the formation of fine homogeneous microstructure. For mass above 50% SiC there was a drop in the values of hardness and fracture toughness. This was attributed to the formation of porous microstructure for SiC mass content above 50%.

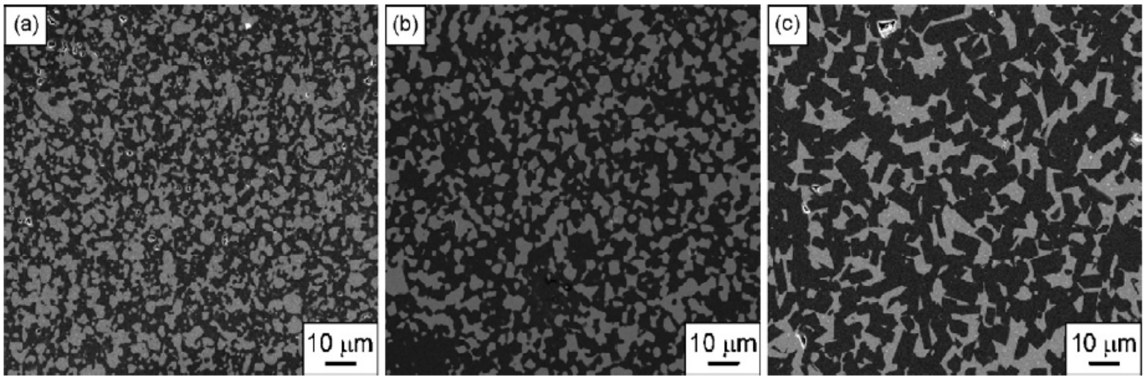

Fig. 1.17 SEM micrographs from polished surface of ZrB_2-50 mass% SiC (a) sintered at 1900˚C for 300 s (b) 2100˚C for 180 s (c) 2165˚C without holding time [27].

Liu *et al.* fabricated nano sized SiC reinforced ZrB_2 composite (20 vol.% SiC) by hot pot pressing at 1900˚C for 30 min and 30 MPa [111]. They evaluated the strength and toughness of the composite and compared it with the literature reported values for ZrB_2 and ZrB_2 reinforced with micro sized SiC particles.

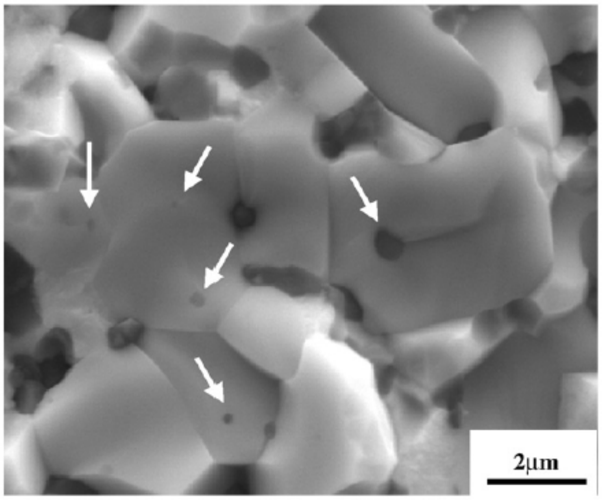

Fig. 1.18 SEM micrograph from fractured surface of ZrB_2-SiC nano composite [111].

The ZrB_2-20% SiC nano particle composite had strength of 925 MPa and a fracture toughness of 6.4 $MPa.m^{1/2}$ which was higher than the literature reported values for ZrB_2 composites reinforced with micro SiC particles. Fig 1.18 shows the SEM micrograph from the fracture surface of ZrB_2-SiC composite. It can be seem from the figure that SiC present inside the ZrB_2 grains (as indicated by arrows) leading to the formation of intragranular microstructure. The presence of intragranular produced micro cracks inside the grains which can help in deflecting cracks and also induced transgranular type of failure. Thus the improvement in strength and toughness was attributed by the formation of intragranular microstructure.

Cao *et al.* [114] also performed a study on the impact of SiC nano particle (20 and 100 nm) reinforcement on the microstructure and mechanical properties of ZrB_2. 5 and 20 mass% of SiC reinforced ZrB_2 ceramic composites were sintered by Spark plasma sintering at 1700˚C. The composites had relative density greater than 97%. The grain size of the ZrB2 matrix decreased with the increase in the mass content of SiC, indicating that SiC acted as grain growth inhibitor. 5 mass% 20 nm SiC particle reinforced composites had the highest strength and fracture toughness. The mechanical properties decreased for 20 mass% SiC composites for both 20 and 100 nm particle size which attributed to SiC agglomeration. Also the mechanical properties was better for the 20 nm particle size SiC reinforced composites than the 100 nm SiC reinforced composites indicating the effect of reinforcement particle size on the mechanical properties of the composites. The improvement in fracture toughness for the composites was due to crack deflection (Fig 1.19(a)) and crack bridging (Fig 1.19(b)).

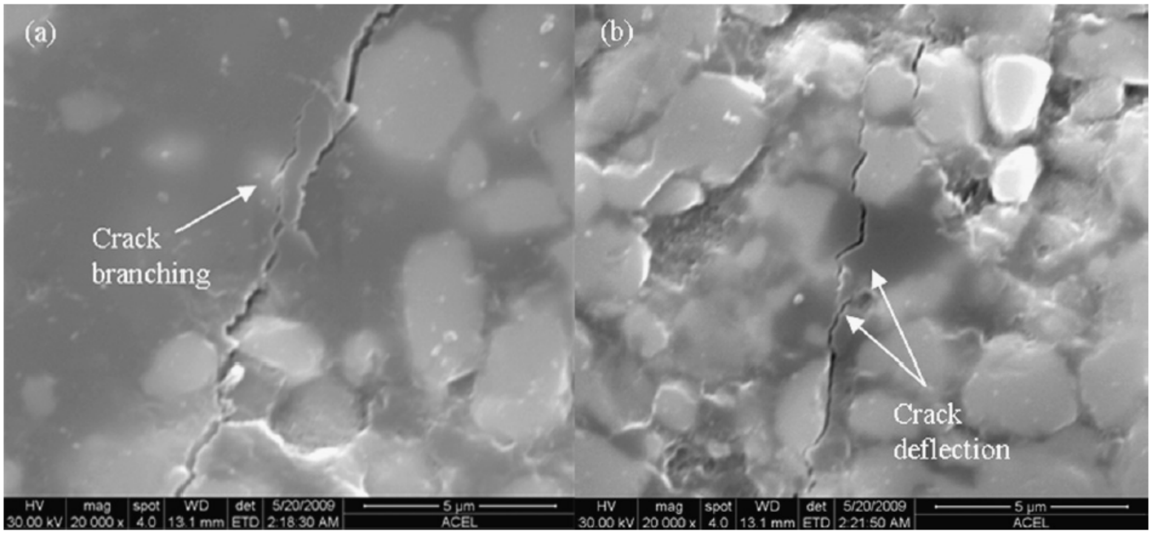

Fig. 1.19 SEM micrographs from polished surface showing crack branching and crack deflection in (a) ZrB_2-5 mass% SiC and (b) ZrB_2- 20 mass% SiC with 20 nm particle size [109].

High temperature flexural strength and fracture behavior of SiC reinforced ZrB_2 composites was carried out by P.Hu and Z. Wang [115]. 15 and 30 vol.% of SiC reinforced ZrB_2 was fabricated by hot pressing at 1900˚C and 30 MPa. Starting particle size of 2 and 0.5 µm for ZrB_2 and SiC were used respectively. The composites were put under flexural strength test at 1800˚C. Both the composites failed at a fairly lower load compared to room temperature testing. They composites had a retained strength of 13 and 7 % from the room temperature strength of 865 and 705 MPa for the 15 and 30% SiC samples respectively. Transgranular fracture with plastic mode of failure was observed in the samples at 1800˚C. The 15% SiC composites had much bigger grain size which acted as the origin of failure, whereas the 30% SiC samples had cavities that acted as the crack initiator for failure. The high temperature testing was also carried out on ZrB_2-15 vol.% SiC samples sintered with a starting particle size of 5 and 2 µm for ZrB_2 and SiC respectively. These samples had better strength retention of 43% of the room temperature strength of 500 MPa and exhibited intergranular fracture with elastic form of failure. The SiC grains pull out at 1800˚C indicated that the bonding strength of SiC-ZrB_2 is less than ZrB_2-ZrB_2 at high temperatures.

In 2011, Zhang *et al.* study the effect of SiC content and particle size on the microstructure and mechanical properties of ZrB_2 [40]. SiC particles with mean particle size of 0.45, 1.05 and 1.45 µm and ZrB_2 particles of 2 µm where used as starting powders to prepare ZrB_2-10, 20 and 30 vol.% SiC composites. B_4C was added as sintering additive and resin derived carbon was added as other reinforcement. The composites were densified using a resistance heated graphite crucible in a temperature range of 1850 to 2050˚C to obtain densification. All the composites had relative density greater than 97%. The average grain size of ZrB_2 decreased from ~5 to ~2 µm for SiC content 10 to 30 vol.% indicating that SiC particles acts as grain growth inhibitor in the ZrB_2 matrix. Young's modulus, hardness, strength and toughness increased with SiC content. The strength increased from ~400 to ~ 500 MPa for 10 to 30% SiC composites with SiC starting size of 0.45 µm. Moreover the SEM microstructural study (fig 1.20) indicated that composites with 0.45 µm SiC particles had a elongated whisker like morphology with an aspect ratio of 4. Whereas the 1.04 and 1.45 µm SiC composites had equiaxed grain structure. The average strength of 30% SiC was ~ 600 MPa for 1.05 µm and ~ 560 for 1.45 µm SiC starting particle size. The study concluded that the middle sized SiC particles reinforced composites with equiaxed grains had the highest strength compared to the fine and coarse SiC reinforced composites. Figure 1.21 shows the variation of grain size and strength of the composites as a function of SiC (0.45 µm particle size) content.

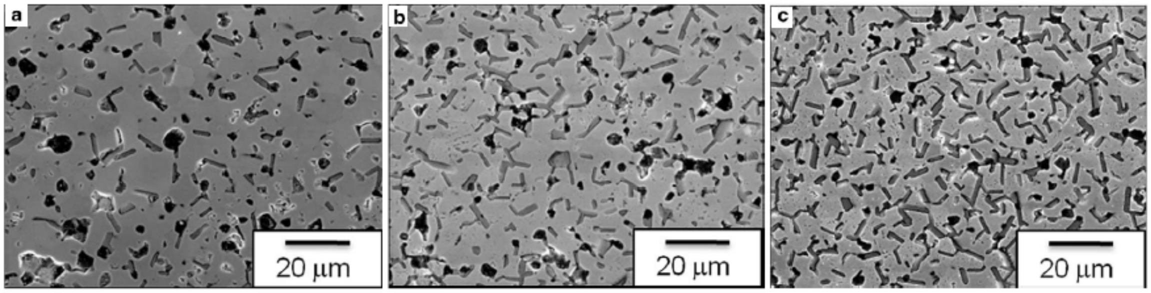

Fig. 1.20 SEM micrograph showing whisker like SiC grains in (a) 10 vol.% SiC , (b) 20 vol.% SiC, (c) 30 vol.% SiC with starting particle size of 0.45 µm [40].

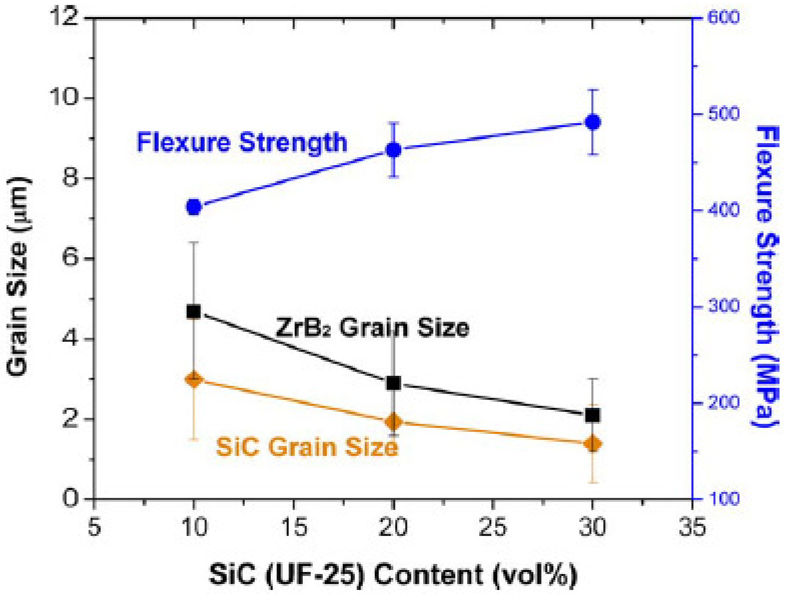

Fig. 1.21 Grain size and flexural strength as a function of SiC content [40].

Apart from the improvement of mechanical properties and as grain growth inhibitor, SiC also improves the oxidation resistance of ZrB_2 [7, 28-38]. At elevated temperatures, SiC forms a glassy SiO_2 a passive oxide layer on the surface of the ceramic which protects it from further oxidation. Opeka *et al.* [7] studied the oxidation behavior of ZrB_2 and ZrB_2- SiC and ZrB_2-ZrC-SiCcomposite. The samples were prepared by hot pressing at 2200˚C and thermogravimetric analyzer (TGA) was used to study the oxidation behavior of the samples. The samples were heated at 20/min to 1500˚C under argon/oxygen atmosphere in the TGA. The samples were also isothermally held for 5 hr at different temperatures. Monolithic ZrB_2 was oxidation resistant up to 1200˚C due to the formation of boria (B_2O_3), but above 1200 the B_2O_3 started to evaporate exposing fresh ceramic surface for oxidation. The ZrB_2 composites with SiC showed oxidation resistance up to 1500˚C with less TGA mass gain compared to monolithic ZrB_2. This was due to the formation of protective glassy borosilicate oxide layer that was stable at high temperature. The study concluded that ZrB_2- 25 vol.% SiC composite had the best oxidation resistance among the composites.

A. Rezaie at performed a systematic study on the evolution of structures during the oxidation of ZrB_2- 30 vol.% SiC composites in air up to a temperature of 1500˚C in a tube furnace [32]. Oxidation testing was also carried out using TGA. ZrB_2 and SiC with average particle size of 2 and 0.7 µm were hot pressed by 1950 to relative density greater that 98%. SEM, EDS and XRD were carried out to study the structure of the oxide products that were formed during oxidation. Up to temperature of 1200 the ZrB_2 was oxidation resistant due to the formation of liquid B_2O_3 layer over ZrO_2, but for temperature above that, the B_2O_3 evaporated due to its low vapour pressure. This is in accord with the observations made by Opeka *et al*. For the ZrB_2-30 vol.% SiC composites, a layer of SiO_2 was formed on the ZrO_2. The EDS study showed the existence of a layer of ZrO_2-SiO_2 under the SiO_2 layer and also ZrO_2 embedded in ZrB_2 matrix. Fig 1.22 shows the evolution of oxide products in the ZrB_2- 30 vol.% SiC put under oxidation test at 1500 for 30 min. The TGA study also served as an evidence for the formation of B_2O_3 below 1200˚C and there was weight loss accounting to the evaporation of B_2O_3 above 1200˚C for both monolithic ZrB_2 and ZrB_2-30 vol.% SiC composite.

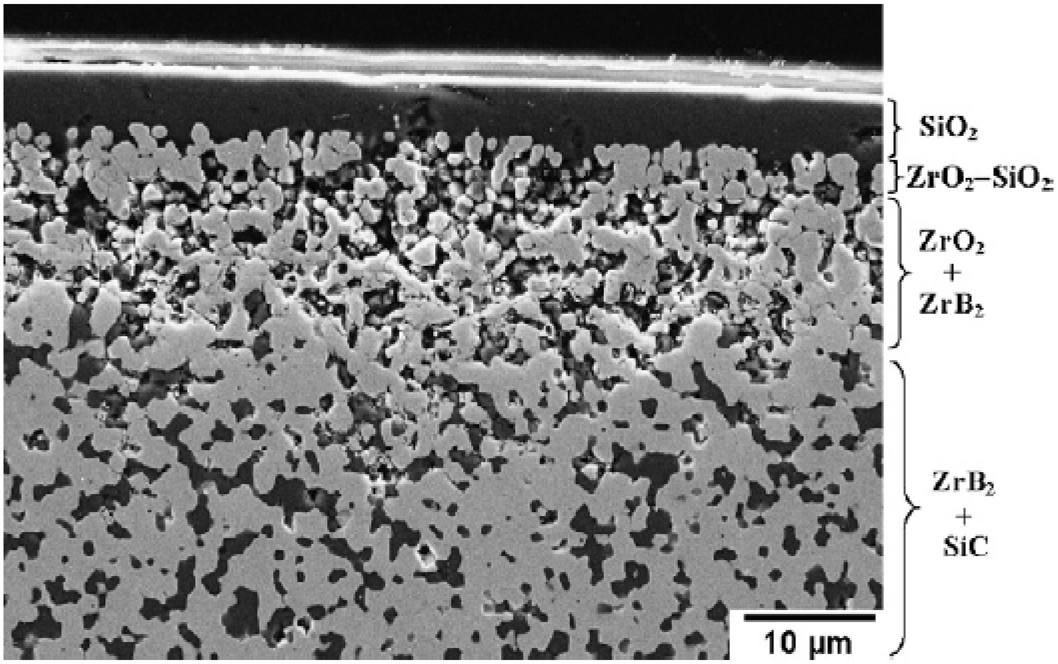

Fig. 1.22 SEM micro graph showing the evolution of oxide products in ZrB_2-30 vol.% SiC composite exposed to air at 1500˚C for 30 min [32].

1.7.2 CNT reinforced ZrB_2 ceramic composite

Using CNT as reinforcement in ZrB_2 ceramic system is a tough task due to very high processing temperatures involved in the consolidation of the composite. Tian *et al.* [81] fabricated ZrB_2- 20 vol.% SiC composites with and without 2 wt.% of multi walled CNTs by hot pressing at 1900˚C under 30 MPa for 1 hour. Mechanical and thermal properties of the composites were evaluated. There was not significant improvement in hardness, flexural strength and thermal conductivity due to reinforcement of CNT, whereas the fracture toughness improved by 15% for the CNT composites attributed to crack deflection and bridging by CNT. This non significant improvement in mechanical properties was attributed to the disintegration of CNT due to very high processing temperature and also strong interfacial bonding CNT and ceramic matrix. Fig 1.23 shows the TEM micrographs of ZrB_2-SiC and ZrB_2-SiC-CNT composites indicating the presence of CNT in the form of agglomerates in the ZrB_2-SiC-CNT composite.

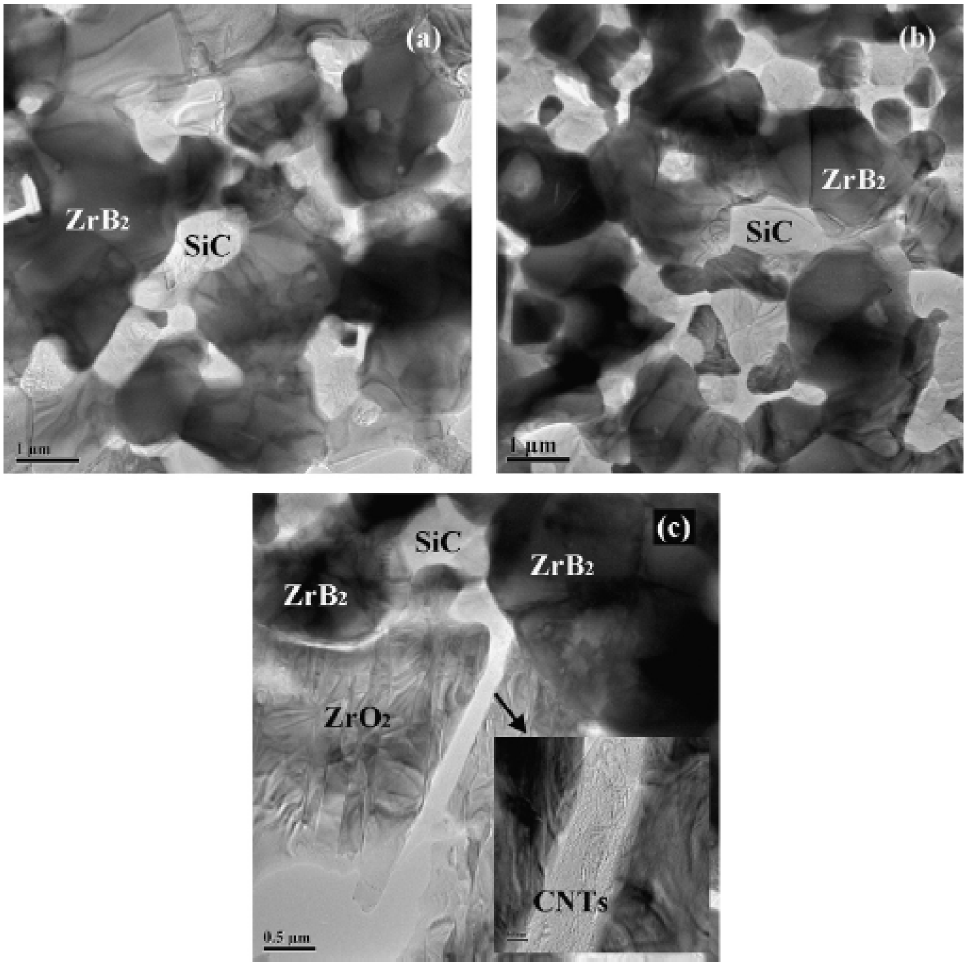

Fig. 1.23 TEM micrographs from (a) ZrB_2-SiC , (b) ZrB_2-SiC-CNT composites and (c) CNT agglomerates in ZrB_2-SiC-CNT composite [81].

1.8 Objectives of study

The objectives of this study are to investigate the effect of SPS processing parameters, reinforcement type and content on the densification mechanism, microstructure and mechanical properties of the ZrB_2 ceramic composites. The properties of composites are compared with those of monolithic ZrB_2. This study will report on the following ZrB_2 composites:

- 10, 20, 30 and 40 vol.% silicon carbide (SiC) reinforced ZrB_2 ceramic composites.
- 2, 4, 6 vol.% multi-walled carbon nanotube (MWCNT) reinforced ZrB_2 ceramic composites
- 2, 4, 6 vol.% graphene nano platelets (GNP) reinforced ZrB_2 ceramic composites.

CHAPTER 2

EXPERIMENTAL DETAILS

2.1 Materials

In this study commercially available zirconium diboride (ZrB_2) powder (99.5% pure, 1-2 μm diameter; Alfa Aesar, Ward Hill, MA, USA), silicon carbide (SiC) powder (2 μm diameter; American Elements, Los Angeles, CA, USA), multi-walled carbon nanotubes (CNTs) (OD/ID: 30-50/5-15 nm, number of walls ~23-67, 10-20 μm length, Nanostructured and Amorphous Materials Inc, Houston, Texas, USA) and Graphene nanoplatelets (GNP) (6-8 nm thick, 16-23 layers, 5 μm diameter, xGnP-M-5, XG Sciences, Michigan,USA) were used as starting materials as shown in table 2.1.

Table 2.1 Specification of materials used

Material	Density (g/cc)	Average size
ZrB_2	6.09	1-2 μm
SiC	3.21	2 μm
MWCNT	2.1	OD/ID: 30-50/5-15 nm Length: 10-20 μm
GNP	2.2	Thickness: 6-8 nm Diameter: 5 μm

2.2 Experimental Procedure

2.2.1 High Energy Ball Milling

The reinforcements were distributed in the ZrB_2 powder matrix with the help of high energy ball milling (Fritsch Pulverisette 7, fig 2.1). ZrB_2, ZrB_2-SiC (with 10, 20, 30, and 40 vol.% of SiC) and ZrB_2-CNT (with 2, 4, and 6 vol.% of CNT) composite powder mixtures were prepared by dry high energy ball milling for 8 min at 500 rpm with ball to powder weight ratio of 5:2. A break of 15 min was given after 4 min of milling to avoid any heating effect during milling. Tungsten carbide (WC) jars and tungsten carbide balls was used for the milling process. The ball milling parameters were carefully chosen to prevent any structural damage to the CNTs.

Fig. 2.1 Ball mill used to prepare composite powders.

For better dispersion of GNP in the ZrB_2 powder matrix, ZrB_2-GNP (with 2, 4, and 6 vol.% of GNP) composite powders were prepared by colloidal processing prior to ball milling. The GNP was dispersed in acetone [117] (0.1 gram of GNP to 100 ml of acetone) using a high speed magnetic stir apparatus (VWR, VMS-C7, fig 2.2) for 1.5 hour. Then ZrB_2 was added to the mixture and stirred for another 1.5 hour. The solution was heated up to 70˚C for 3 hours using same magnetic stir apparatus (incorporated with a heating element) and then the solution was placed in the hood for 24 hours for complete evaporation of acetone. The dry composite powders were then ball milled at 500 rpm for 5 min. Ball milling the GNP powder composite will enable exfoliation of the GNP into fewer or even single layer graphene [118].

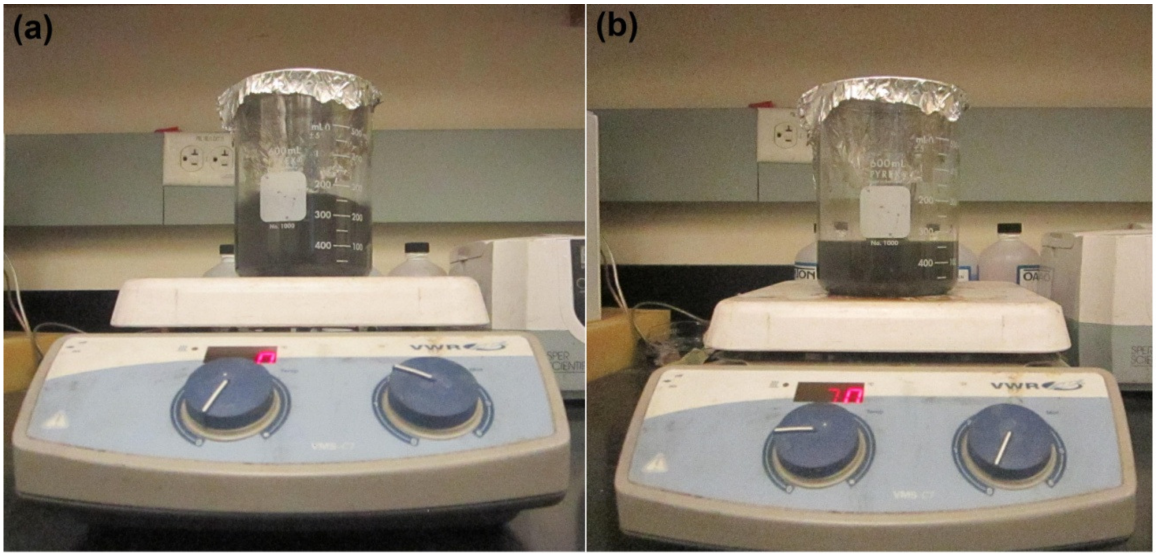

Fig. 2.2 Magnetic stir apparatus (a) colloidal processing (b) heating process.

2.2.2 Spark Plasma Sintering

Spark plasma sintering of ZrB_2 monolithic and composites was carried out using model SPS 10-3 manufactured by Thermal Technologies LLC (Santa Rosa, CA, USA). As shown in figure 2.3 the SPS equipment consists of three main systems namely the power unit, heating furnace and vacuum and cooling pumps. With a 3000 amps and 5 volts DC power supply the equipment is capable of producing 2500˚C within 5 minutes. A rapid heating rate of up to 600˚C/min can be obtained using this equipment. A high cooling rate can be obtained by purging the SPS furnace with liquid argon gas. A high vacuum of 10^{-2} Torr can be attained inside the heating chamber to maintain purity of the samples. The hydraulic pump system can reach up to maximum pressure of 100 kN. A single-color optical pyrometer (Raytek, RAYMM1MHVF1V) is used to measure the temperature profile of the sample. The SPS ram displacement, temperature and pressure profiles are continuously monitored to study the densification mechanism of the samples.

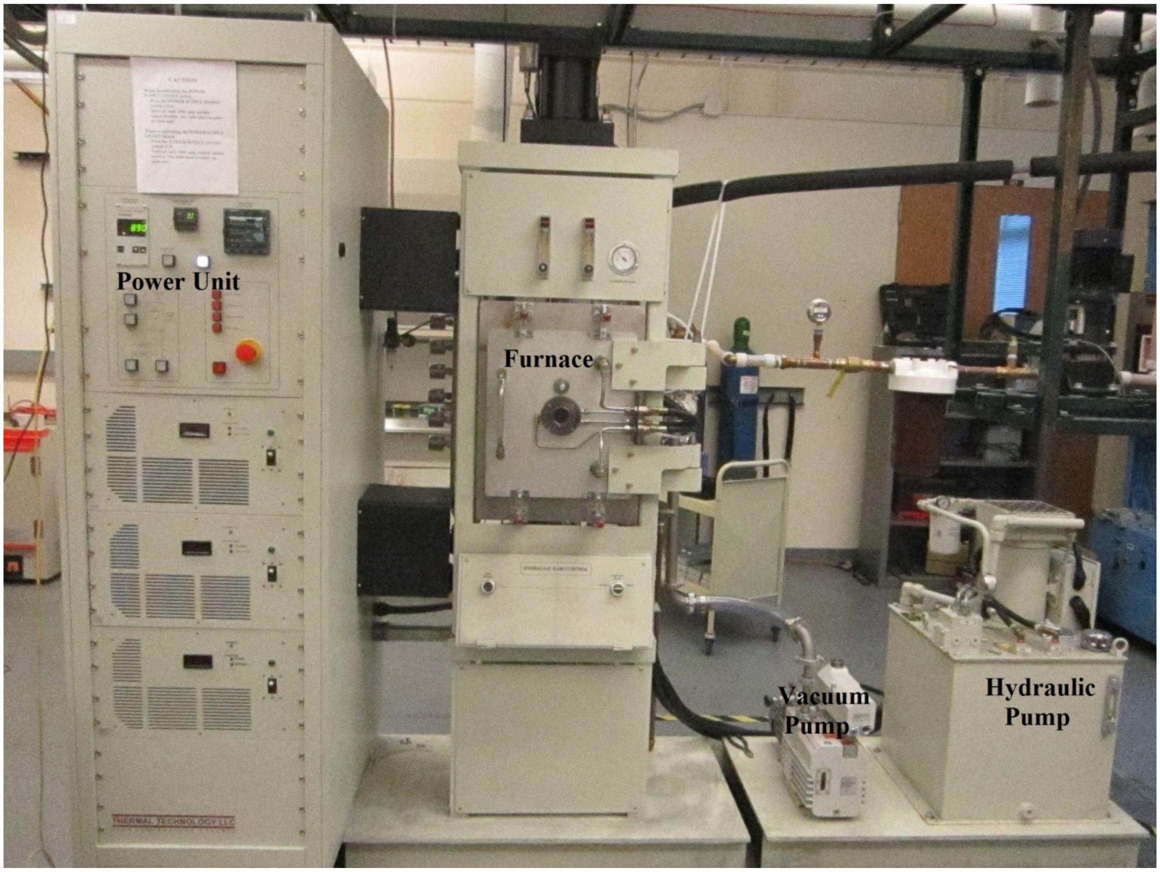

Fig. 2.3 Spark Plasma Sintering equipment.

The densification of the samples is dependent on the processing parameters like heating rate, temperature and pressure. The type of dies and punches used for sintering depends on the processing parameters of the samples. Usually graphite dies and punches are used in SPS for their ease of availability and good thermoelectric properties at high temperature. They are used for high temperature moderate pressure sintering. For consolidation of materials, the powder is placed in between the dies, punches and spacers assembly (as shown in figure 2.4) and processed in the SPS furnace with predefined parameters. Graphite cloth is wrapped around the graphite die to provide thermal insulation. A small hole is drilled through half the thickness of the graphite dies for accurate temperature measurement by the pyrometer (fig 2.5).

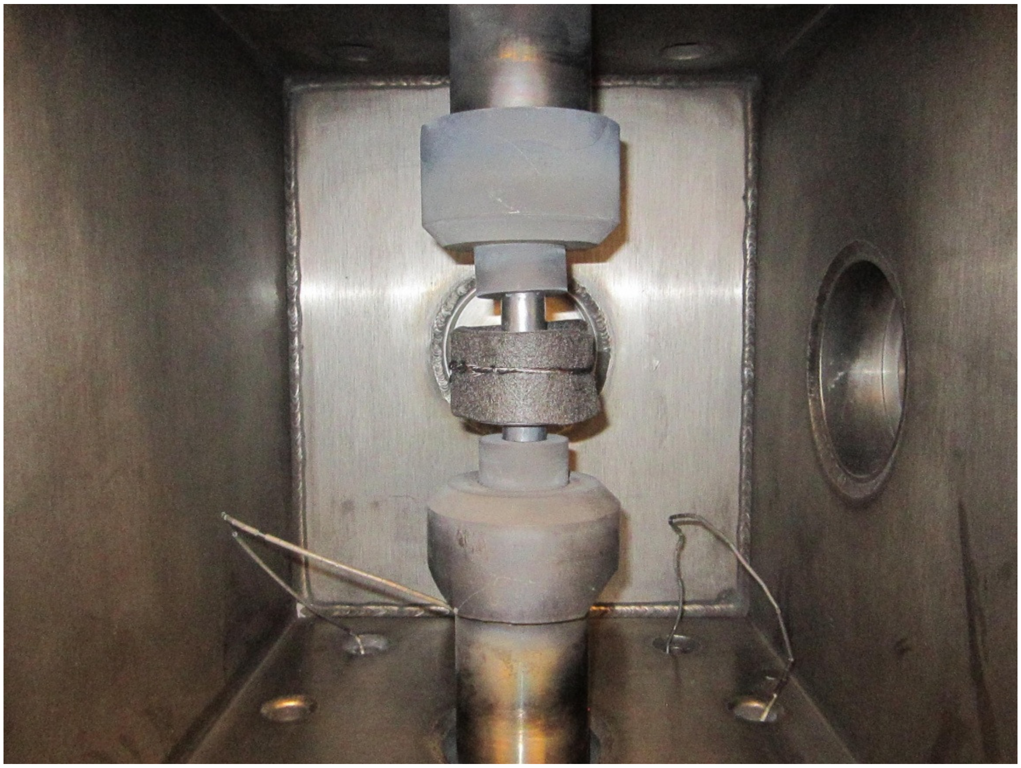

Fig. 2.4 Sample powder compacted in graphite die, punches and spacers assembly.

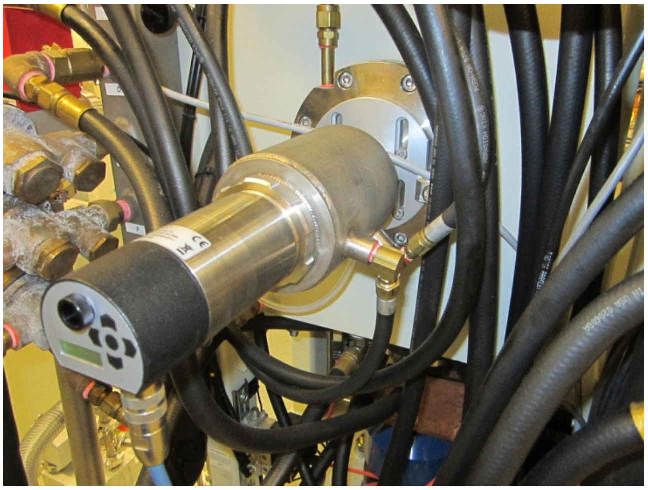

Fig. 2.5 Single color optical pyrometer to measure temperature of sample during SPS.

2.3Processing of ZrB_2 ceramic composites

2.3.1 Fabrication of ZrB_2 and ZrB_2 composites by SPS

Zirconium diboride and zirconium diboride composites (ZrB_2-SiC, ZrB_2-CNT and ZrB_2-GNP) were sintered by spark plasma sintering. All the ZrB_2, ZrB_2-SiC, ZrB_2-CNT and ZrB_2-GNP composite powders were SPS sintered at 1900˚C with uniaxial pressure of 70 MPa and soaking time of 15 min under inert argon atmosphere (high vacuum of 10^{-2} Torr was maintained in the SPS furnace till 1200˚C after which the chamber was purged with argon gas). A heating rate of 100˚C/min was used during SPS processing. Graphite dies and punches were used for sintering disc-shaped samples of 20 mm diameter and 2 mm thickness. The optical pyrometer was used to continuously monitor the temperature of samples during sintering.

2.4 Material Characterization

2.4.1 Relative Density Measurement

Bulk densities of the sintered samples were measured using Archimedes' principle. The rule of mixtures was followed to calculate the theoretical densities of the composites. The density of the samples can be measured using the equation given below.

$$\rho = \frac{x}{x-y}(\rho_o - \rho_L) + \rho_L \qquad (2.1)$$

where ρ is the density of the sample, x is the weight of samples in air, y is weight of samples in water, ρo is the density of auxiliary liquid (in this study its water, ρo at 20°C= 0.99804 g/cm^3) and ρL is air density (0.0012 g/cm^3). Density of samples was measured with the instrument provided by Mettler Toledo (Delta Range XD204, fig 2.6).

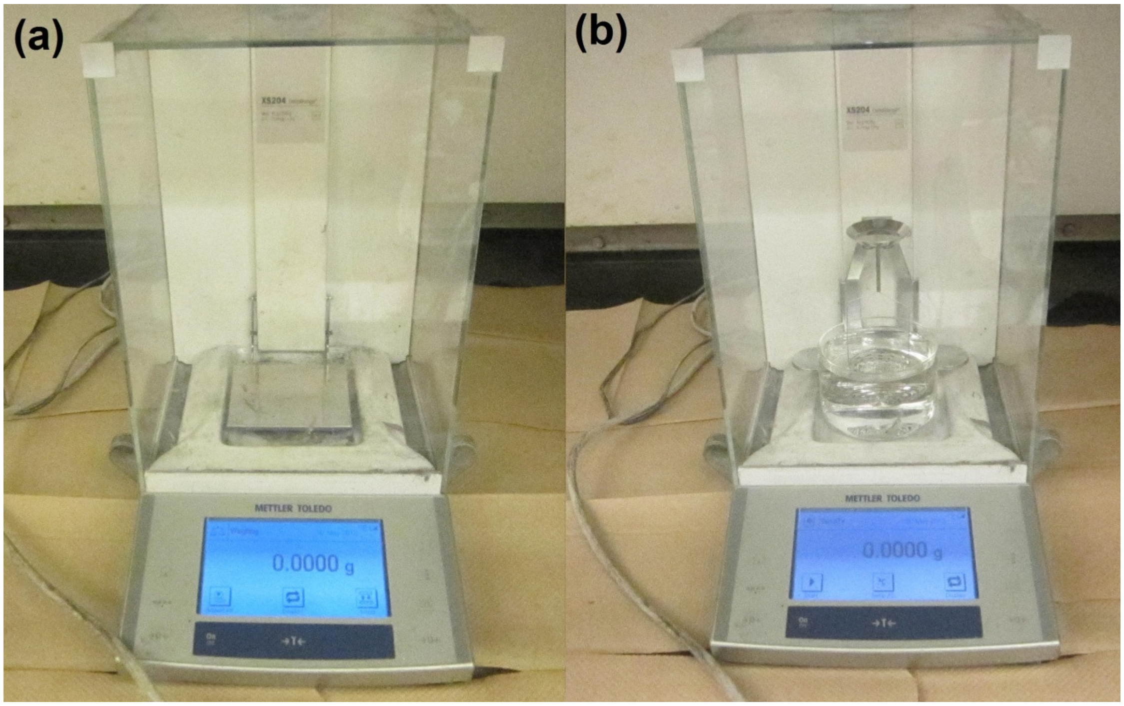

Fig. 2.6 Apparatus to measure (a) weight and (b) density of sintered sample.

The relative density of the samples can be measured from the following equation, where the theoretical density of the powder is calculated based on rule of mixture.

$$Relative\ Density = \frac{Density\ of\ sintered\ samples}{Theoretical\ Density\ of\ powder} \times 100 \ldots\ldots\ldots\ldots\ldots\ldots \quad (2.2)$$

2.4.2. Phase and Mirco Structural Analysis

2.4.2.1 X-ray Diffraction Analysis

X-ray diffraction (XRD) analysis was carried out on the spark plasma sintered zirconium diboride and zirconium diboride composite samples using Philips Norelco X-ray diffractometer operating with Cu K_α radiation (λ= 1.54178 Å) at 45 kV and 40 mA. The diffraction angle (2θ) was varied between 20 and 90° at a step increment of 0.02° with a count time of 1 s.

2.4.2.2 Raman Spectroscopy Analysis

The XRD study was not conclusive for the ZrB_2-CNT and ZrB_2-GNP samples due to low volume fractions of these reinforcements. Therefore Raman spectroscopy, a powerful tool to study the characteristics of graphene based compounds was carried out for these composites. Raman spectroscopy was carried out on fracture surfaces of ZrB_2-CNT and ZrB_2-GNP composites using WITec alpha300 R Raman system (532 nm laser excitation, 0.8 mW laser power, and 20 µm spot size) to identify presence and structural quality of CNTs in the composites.

2.4.2.3 SEM and EDS Analysis

The characterization of microstructure, fracture behavior and crack propagation and toughening mechanism in the sintered samples was conducted using scanning electron microscopy (JSM-6360, JEOL). The chemical characterization of ZrB_2-SiC composites was conducted using energy dispersive spectroscopy (EDS). FEI Quanta 600 field-emission gun Environmental SEM with an Evex EDS X-ray microanalysis system and HKL EBSD system is used for EDS analysis.

2.4.3 Mechanical Testing

2.4.3.1 Microhardness and fracture toughness Testing

The micro hardness of the samples was determined using Vicker's micro indentation (Clark Microhardness tester, CM-700-AT) operated with normal force of 9.8 N and holding time of 15 s on the polished surface of the SPS sintered samples (Fig 2.7). The indentation fracture toughness of the samples was calculated using diagonal crack lengths produced at the indentation corners from the microindentation tests. Fracture toughness values are based on three samples with five indents per sample. The fracture toughness K_{IC} is given by:

$$K_{IC} = 0.016\left(\frac{E}{H}\right)^{1/2}\frac{P}{c^{3/2}}\ldots\ldots\ldots\ldots\ldots\ldots\ldots\ldots\ldots\ldots\ldots\ldots (2.4)$$

where *E* is the Young's modulus of the composites by rule of mixtures (Young's modulus of ZrB_2, SiC and CNT are 500, 475, 1000 GPa respectively), *H* is the Vickers hardness (GPa), *P* is the applied load (N), and *c* is the diagonal crack length (m) [119].

Fig. 2.7 Clark Microhardness tester.

2.4.3.2 Flexural strength Test

The flexure strength for the samples (20 mm diameter and 2 mm thickness) was determined by a ring-on-ring (RoR) test method (Instron 5567, ASTM C1499-05). The support and loading ring diameters were 15 mm and 5 mm, respectively, with a displacement controlled loading rate of 0.5 mm/min. Adhesive tape was applied on the compressive side of the discs as per ASTM C1499 [120]. The flexure strength σ_{RoR} is given by:

$$\sigma_{ROR} = \frac{3P}{2\pi t^2}\left(\frac{(1-v)(a^2-r^2)}{2R^2} + (1+v)ln\frac{a}{r}\right) \ldots\ldots\ldots\ldots\ldots\ldots\ldots \text{(2.5)}$$

where P is the applied load (N), v is the Poisson's ratio of the composites by rule of mixtures (the Poisson's ratio of ZrB_2, SiC and CNT are 0.15, 0.19 and 0.165 respectively), a is the radius of the support ring, r is the radius of the load ring (m), and R and t are the radius and thickness (m) of the sample [121].

2.4.4 Oxidation Testing

The oxidation properties of ZrB_2 and ZrB_2-SiC composites were tested using thermogravimetric analysis (TGA) provided by ThermoFisher Scientific (Versa Therm, NH, USA). The fractured samples were put under TGA at a maximum temperature of 1100˚C. The samples were loaded in to the TGA and the TGA was purged with helium with a flow rate of 10 ml/min at 25˚C for the first 3 min for optimizing the equipment. Later the TGA was purged with air as carrier gas at a flow rate of 10 ml/min and a heating rate of 20˚C/min was applied to reach the peak temperature of 1100˚C. The weight of the samples was continuously recorded and the percentage increase in weight is plotted as a function of increase in temperature to study the oxidation properties of the samples.

CHAPTER 3

RESULTS AND DISCUSSION

3.1 Spark Plamsa Sintering of SiC reinforced ZrB_2 Ceramic Composites

3.1.1 Relative density, Densification Mechanism and Microstructure

The relative density of monolithic ZrB_2 and ZrB_2-SiC composites as a function of reinforcement content is indicated in figure 3.1. For the same SPS processing parameters, the relative density of monolithic ZrB_2 was about 85%, whereas all the ZrB_2-SiC (10, 20, 30 and 40 vol.% SiC) composite samples had a relative density >99%. The addition of SiC to ZrB_2 matrix has improved the densification of the composites. There was a small increase in the relative density with increase in reinforcement content of SiC. The relative density data indicates that for similar SPS parameters near full densification is possible for the ZrB_2-SiC composites where as the monolithic ZrB_2 has a lower relative density. A higher sintering temperature or longer holding time is required for better densification of ZrB_2. The improvement in densification of the SiC reinforced ZrB_2 composites can be attributed to particles rearrangement by applied pressure, necking and grain diffusion mass transfer mechanism caused by pulsed DC and also by dislocation creep facilitated by thermal stress due to non uniform temperature distribution caused by mismatch in thermal conductivity of SiC and ZrB_2.

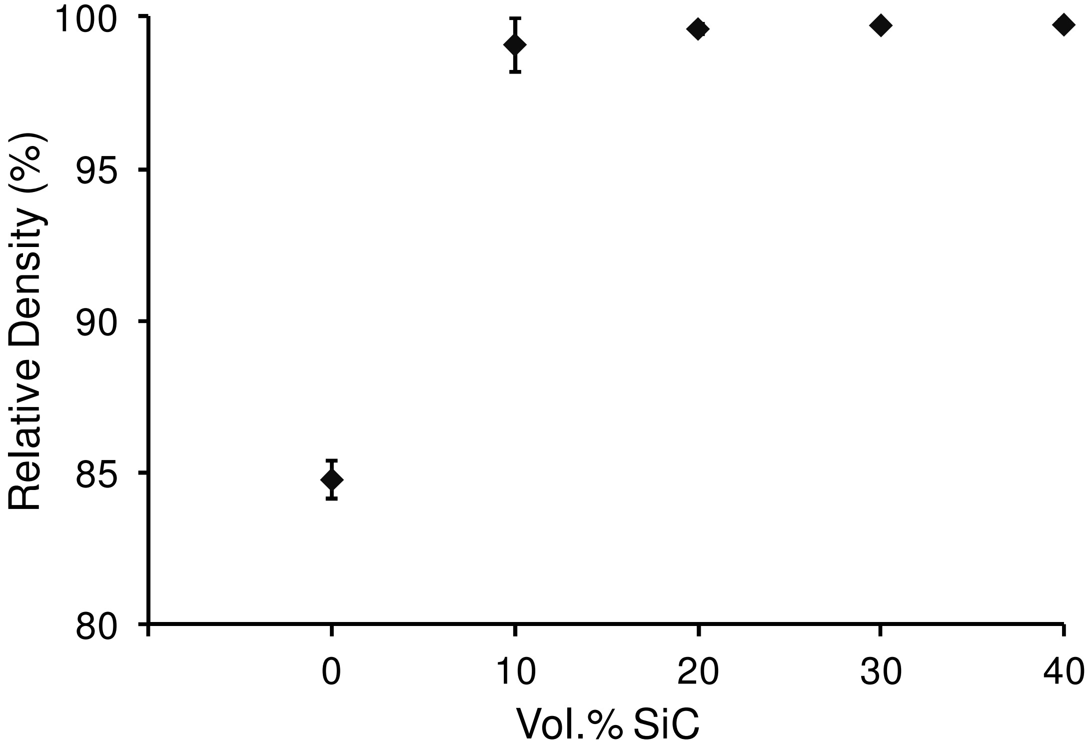

Fig. 3.1 Variation of relative density of ZrB_2-SiC composites with reinforcement content.

To understand the densification behavior of ZrB_2-SiC composites during SPS processing, the data on punch displacement was recorded during sintering. Fig. 3.2 shows the variation of punch displacement with sintering time during initial heating and soaking stages of sintering cycles. The sintering temperature and applied pressure during these sintering stages are also indicated in the figure. Note that the sintering cycle was initiated with simultaneous increase in temperature (100°C/min) and pressure (10 MPa/min). The sintering pressure of 70 MPa was reached in first 8 minutes, and the sintering temperature of 1900°C was reached in first 17 minutes of the sintering cycle. The samples were soaked for 15 min at the given sintering temperature of 1900°C and pressure of 70 MPa (total heating and soaking time of 32 min).

As showed in Fig. 3.2, where a positive slope indicates compression and negative slope indicates expansion, the punch displacement showed three distinct trends during SPS sintering: initial increase corresponding to densification with pressure leading to particle rearrangement and reduction in inter particle porosity (stage I), intermediate decrease corresponding to thermal expansion (stage II), and final increase due to densification (stage III). The densification in Stage III is facilitated by the reduction of surface curvature of the particles by applied temperature and simultaneous pressure causing a reduction in surface energy which drives the sintering mechanism. The ON-OFF DC pulsed current induces joule heating in the powder particles and also discharges sparks in the gaps and contact area between the ZrB_2 and SiC particles. This spark production creates very high localized temperature leading to the evaporation and subsequent solidification causing surface diffusion on the surface of the particles. This evaporation and melting on the surface (surface diffusion) of the particles produces necking of the particles leading to volume diffusion. The Particles form several necks with the adjacent particles leading to the expansion of necks. Finally the expansion of necks is formed into grain boundaries by plastic deformation (grain boundary diffusion). The difference in thermal conductivities of SiC and ZrB_2 leading to dislocation creep and also the dielectric break down of oxide impurities improving the densification of the composites.

The first stage is dominated by densification of power by the rearrangement of particles and plastic deformation due to applied pressure. The extent of punch displacement during this stage I is very small (<0.25 mm) for pure ZrB_2 samples. This may be due to the fairly uniform particle size of 1-2 μm for monolithic ZrB_2 leading to little rearrangement of particles. The ZrB_2-SiC composites had better rearrangement of particles attributed by the differences in the particle size between SiC and ZrB_2 indicated by better SPS punch displacement during stage one. In general the extent of punch displacement during this stage increases with increasing reinforcement content with 40 vol.% SiC composites had the highest displacement of ~1.25 mm.

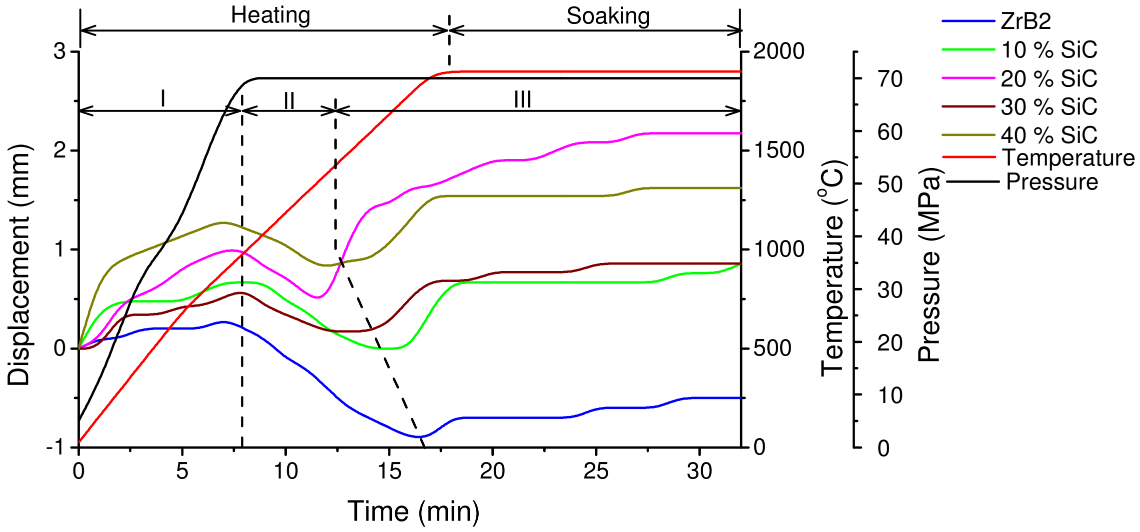

Fig. 3.2 Ram displacement, temperature and pressure profiles during heating and soaking stages of SPS sintering cycles for ZrB_2-SiC composites.

Stage II as indicated in figure has a negative slope indicating thermal expansion of compact powder. Stage III is the actual densification process induced by pulsed DC of spark plasma sintering creating localized joule heating under simultaneously applied pressure. The densification of the compact powder takes place by mass transfer mechanism (as explained above) and small grain growth facilitating densification. The monolithic ZrB_2 showed poor densification mechanism in stage III. There was no significant punch displacement in stage III for ZrB_2, this is a clear indication that the current SPS parameters is not good enough to obtain full densification of ZrB_2. Therefore for better densification of ZrB_2 the sintering temperature and/or the holding time should be increased. The ZrB_2-SiC showed better densification in stage III, indicating better mass transfer mechanism in the composites. The differences in melting point of SiC and ZrB_2 also contribute to densification of the composites. SiC has a lower melting point of 2820˚C than ZrB_2 that has a melting point of 3245˚C, thus leading to better mass transfer of the reinforced phase at same SPS parameters leading to better densification. There is also a thermal conductivity mismatch between the reinforced SiC (114 W/mK) [1] and ZrB_2 (56 W/mK) [122] matrix. This difference in thermal conductivities leads to thermal stress in the composite facilitating dislocation creep. For ZrB_2, this stage II-III transition corresponds to starting of soaking stage (t=17 min; T=1900°C). Whereas for ZrB_2-SiC (10-40 % SiC) composite samples, this stage II-III transition point corresponds to about t=11-15 min (corresponding temperature of ~1300-1700°C in heating cycle). This indicates that for the SiC composites the densification starts much earlier than the monolithic ZrB_2. This shift of densification towards lower temperature in the composites is caused by the above mentioned densification mechanisms.

Figure 3.3 shows the SEM micrographs from the fracture surfaces of ZrB_2 and ZrB_2-SiC composites. The pure ZrB_2 exhibits well distributed porosity with the grain size equivalent to starting particle size of 1-2 µm (Fig. 3.3(a)). The fracture surfaces from ZrB_2-SiC samples show dense faceted grain structure with well distributed SiC particles (Fig. 3.3(b-d)). The microstructural observations from the fracture surfaces are in general agreement with the measured relative density values for these ZrB_2 and ZrB_2-SiC composite samples. While the distributed larger grains with grain size about <5 μm appear in the microstructures of the ZrB_2-SiC composites, significant grain growth was not observed. This insignificant grain growth is attributed to the rapid heating rate of SPS which in turn inhibits surface diffusion that caused grain coarsening. The fracture surface of the composites shows rough surface morphologies with intergranular form of fracture. The voids in the composites are attributed to the SiC grains pull-out during fracture of the composite samples.

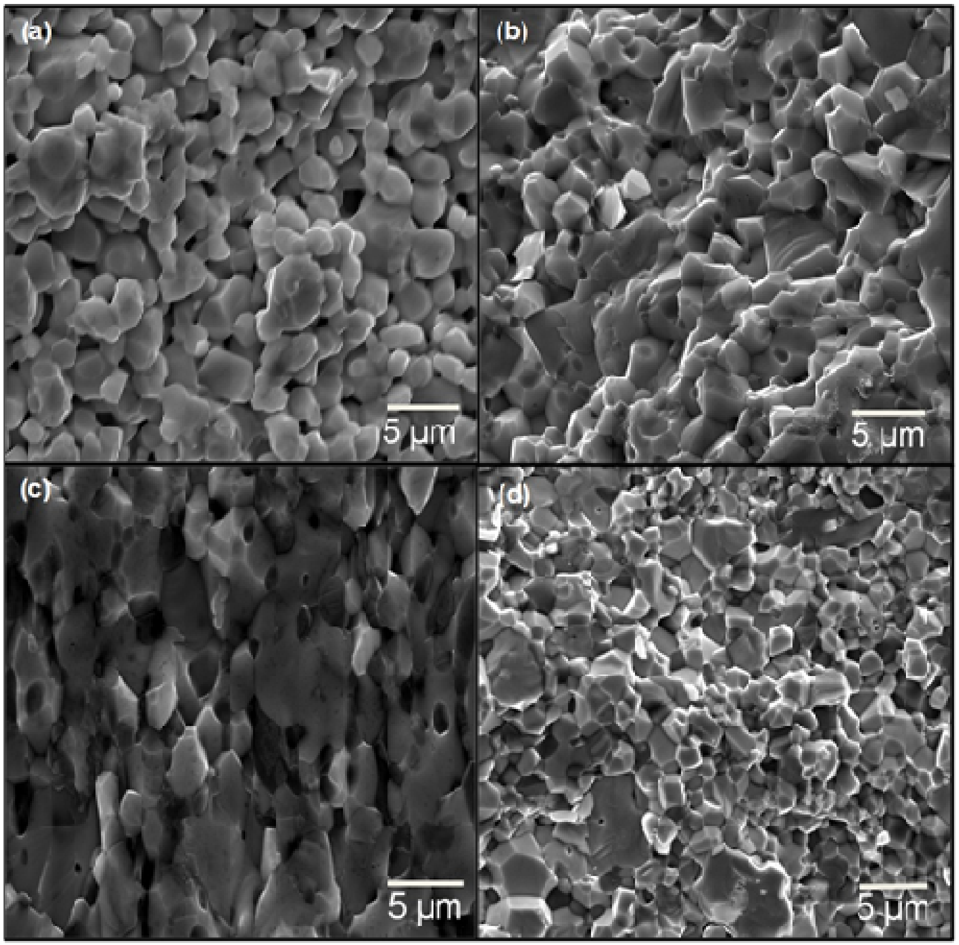

Fig. 3.3 SEM micrographs from the fracture surfaces of (a) ZrB_2, (b) ZrB_2+10% SiC, (c) ZrB_2+20% SiC, and (d) ZrB_2+40% SiC composites.

Figure 3.4 shows the SEM image from the fracture surface of ZrB_2-10 vol.% SiC composite with a high magnification insert showing SiC particle intact in ZrB_2 matrix. The insert shows a small reduction in the size of SiC particle which can be attributed to ball milling of the composite powder prior to sintering.

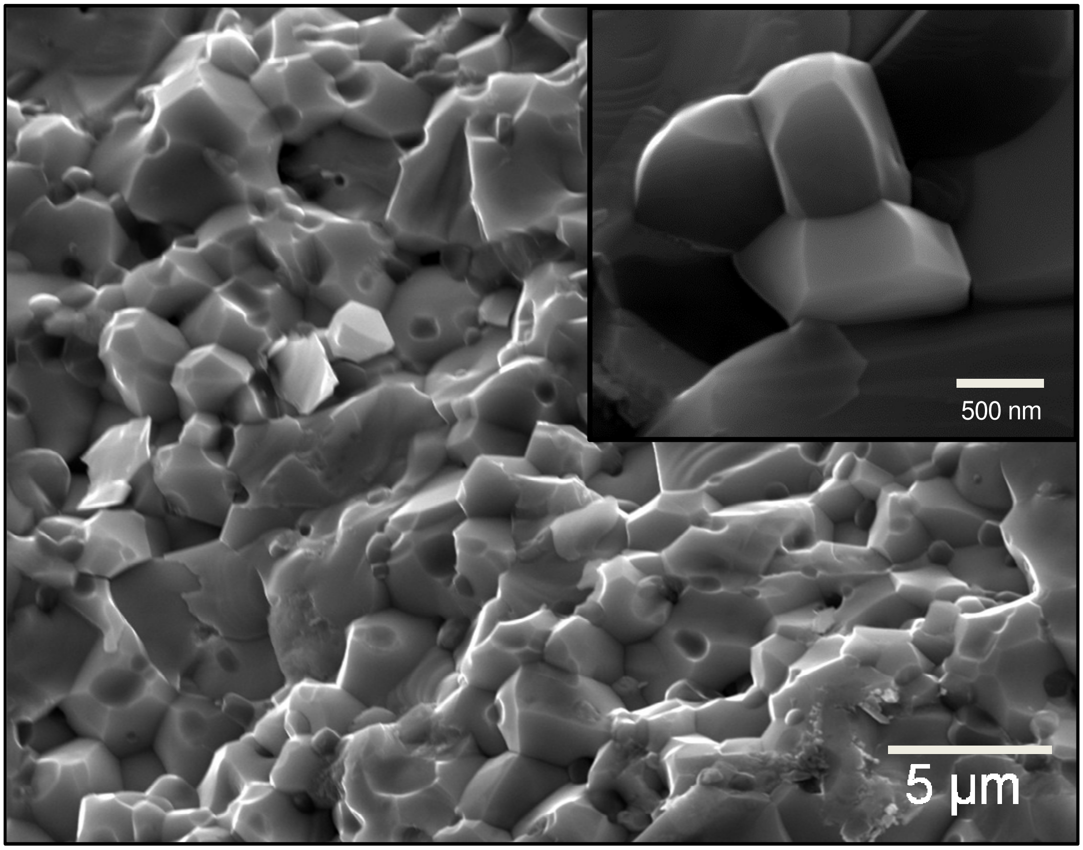

Fig. 3.4 SEM micrograph from fracture surface of ZrB_2- 10 vo.% SiC composite with high magnification SEM insert showing SiC particle intact in the ZrB_2 matrix.

3.1.2 XRD and EDS Analysis

X-ray diffraction (XRD) patterns from SPS sintered ZrB_2, ZrB_2-SiC (10,20,30 and 40 vol.% SiC) composites are presented in Fig. 3.5. For ZrB_2-SiC composites, all the characteristic peaks of ZrB_2 and SiC were identified. No additional peaks were observed suggesting sintering of two phase mixtures without any undesirable interfacial reactions. The XRD analysis indicates that the chosen SPS parameters did not disintegrate the reinforced SiC particles.

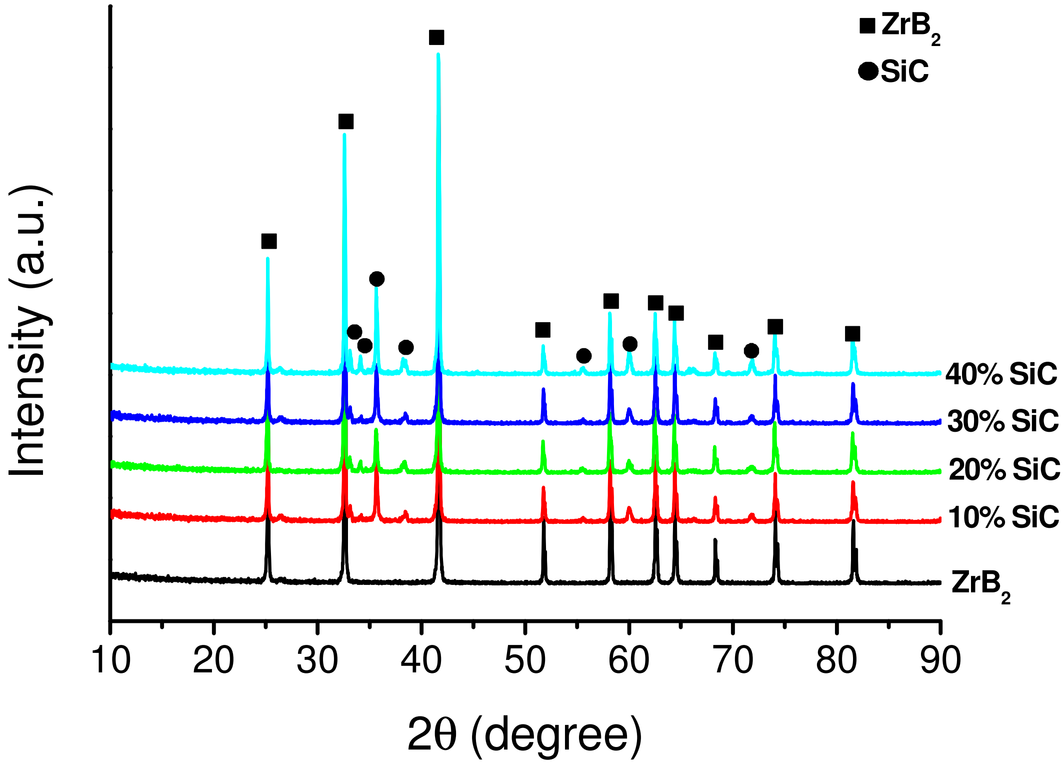

Fig. 3.5 XRD patterns of Spark Plasma Sintered ZrB_2 and ZrB_2-SiC composites.

Energy dispersive spectroscopy (EDS) was carried out to study the composition changes that could have occurred in the spark plasma sintered ZrB_2-SiC composites. The EDS study concluded that no compositional changes occurred during the sintering process and both the SiC reinforced particles and ZrB_2 matrix remind intact. Fig 3.6 shows the EDS mapping for ZrB2- 10 vol.% SiC composite. The EDS mapping showed intense peak for Zr and a smaller Si peak corresponding to their original composition.

The mapping was done at low SEM magnification to cover larger fracture surface area. The mapping images show uniform distribution of SiC in the ZrB_2 matrix (bright green spots indicating SiC particles and red region indicating ZrB_2 matrix). This indicates that the chosen ball milling parameters were good to obtain uniform distribution of SiC particles in ZrB_2 powder matrix.

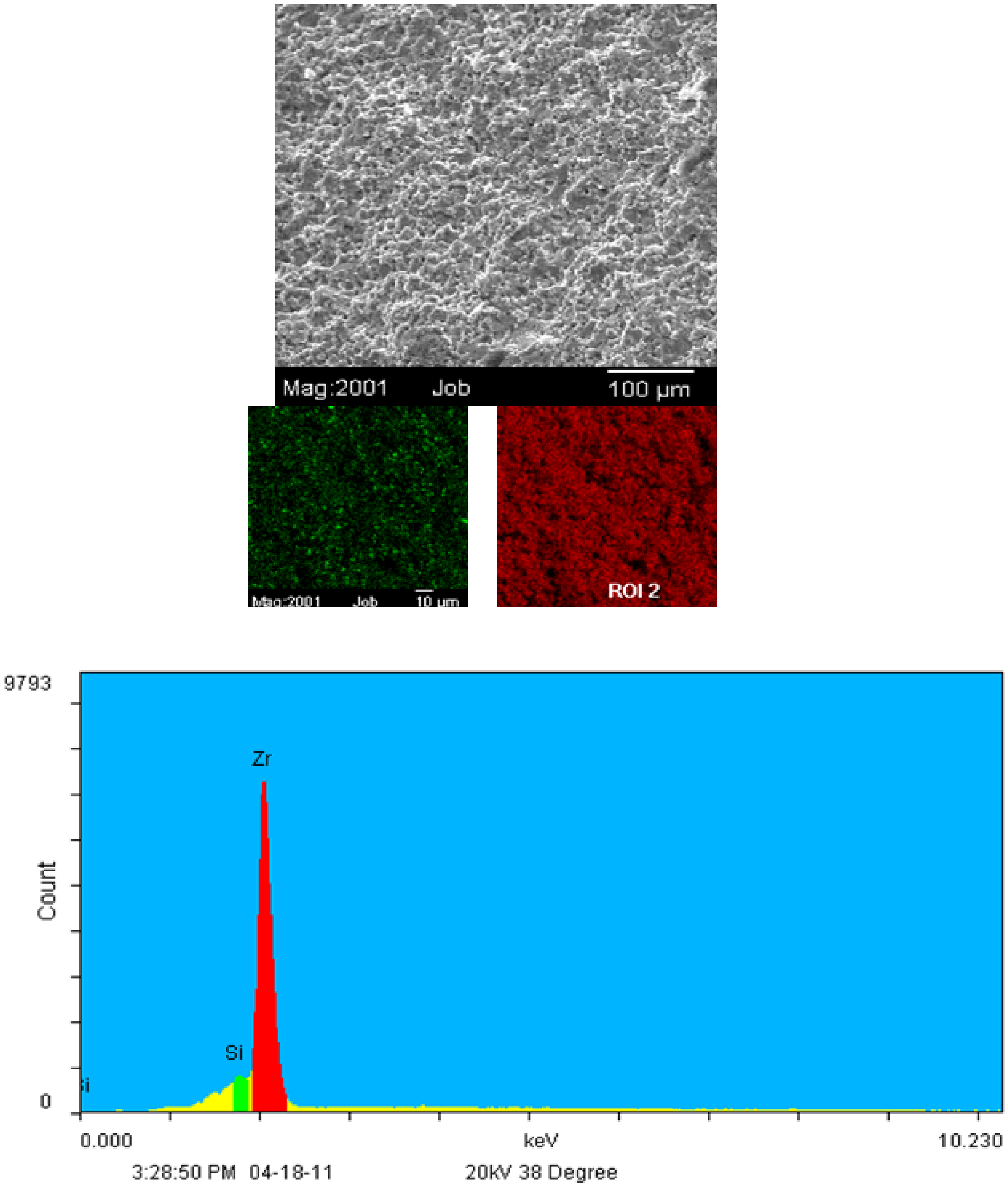

Fig. 3.6 EDS analysis of ZrB_2- 10 vol.% SiC composite.

3.1.3 Mechanical Properties of ZrB_2-SiC composites

3.1.3.1 Micro Hardness

The variation of hardness of ZrB_2 and ZrB_2-SiC composites with the reinforcement content is shown in figure 3.7. The average hardness of SPS sintered ZrB_2, with relative density of ~85%, was found to be 16.64 GPa in this investigation. The average hardness of the ZrB_2-SiC composites increased with increasing SiC reinforcement content with maximum hardness of reaching ~22.71 GPa for composites with 40% SiC. The average hardness of 10, 20 and 30 vol.% of 19.38, 20.80 and 21.44 GPa respectively. The higher hardness for the ZrB_2-SiC composites compared to ZrB_2 seems to be due to combination of effects such as higher relative density and presence of high volume fraction of harder reinforcement (SiC) particles. he increasing hardness with SiC content seems primarily due to composite strengthening.

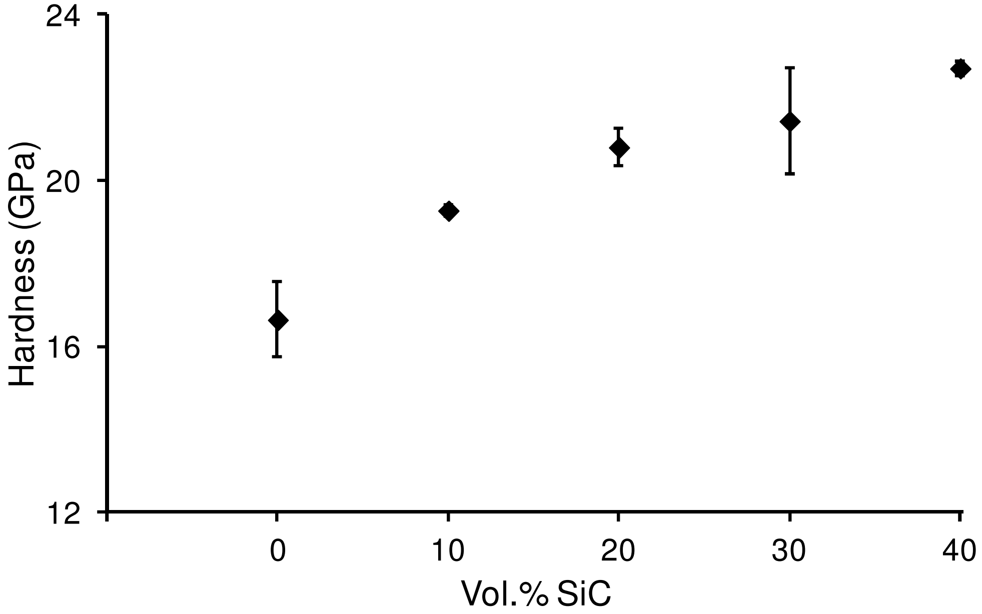

Fig. 3.7 Hardness of ZrB_2-SiC composites as a function of reinforcement content

3.1.3.2 Flexural Strength

The SPS sintered ZrB_2 samples had biaxial flexure strength of 162 MPa and the flexural strength of the ZrB_2-SiC composites was improved with increasing SiC reinforcement content (Fig. 3.8). The flexural strength of the SiC reinforced composites was in the range of 300 to 560 MPa with 10 vol.% SiC composites had the highest flexural strength of 553±07 MPa. The flexural strength of 20, 30 and 40 vol.% SiC composites was 301±51, 431±39, 410±17 MPa respectively. The low flexural strength of ZrB_2 is mainly attributed to the low relative density of 85% with distributed porosity. The improvement in the flexural strength for the SiC reinforced composites can be attributed to better relative density of >99%, intergranular fracture mechanism and SiC grains pull-out.

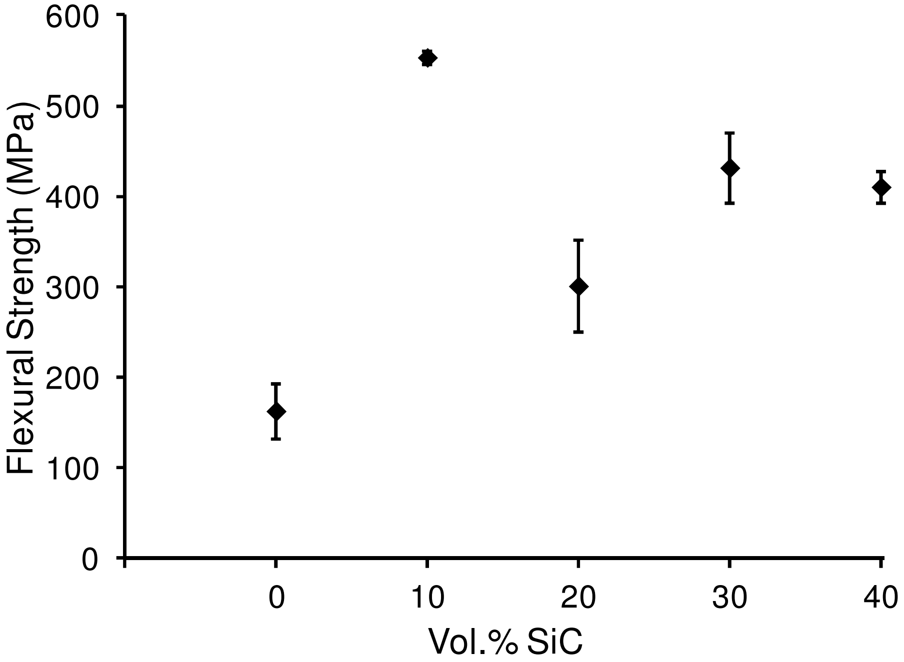

Fig. 3.8 Flexural strength of ZrB_2-SiC composites as a function of reinforcement content.

The fracture surface of ZrB_2-SiC composites (Fig. 3.3(b-c)) shows dense microstructure with predominantly intergranular form of fracture with rough surface morphology. The voids seen in the fracture surfaces of the composites are created by SiC grains pull-out which helped in the improvement of flexural strength of the composites.

3.1.3.3 Fracture Toughness

There was Significant improvement in fracture toughness was observed in the ZrB_2-SiC composites compared to ZrB_2. The variation of fracture toughness with reinforcement content is shown in figure 3.9.The average fracture toughness of SPS sintered ZrB_2 was 1.5 MPa.m$^{1/2}$. Whereas the average fracture toughness of ZrB_2-SiC composites was in the range of 2-2.7 MPa.m$^{1/2}$. The low fracture toughness of monolithic ZrB2 is attributed to its low relative density of ~85% and the absence of reinforcements to improve toughening mechanisms in the ceramic matrix. Among the ZrB_2-SiC, the 20% vol.% composites had the highest toughness of 2.66±0.34 MPa.m$^{1/2}$. The 10, 30 and 40 vol.% SiC composites had fracture toughness of 2.21±0.25, 1.92±0.32, 2.31±0.23 MPa.m$^{1/2}$ respectively.

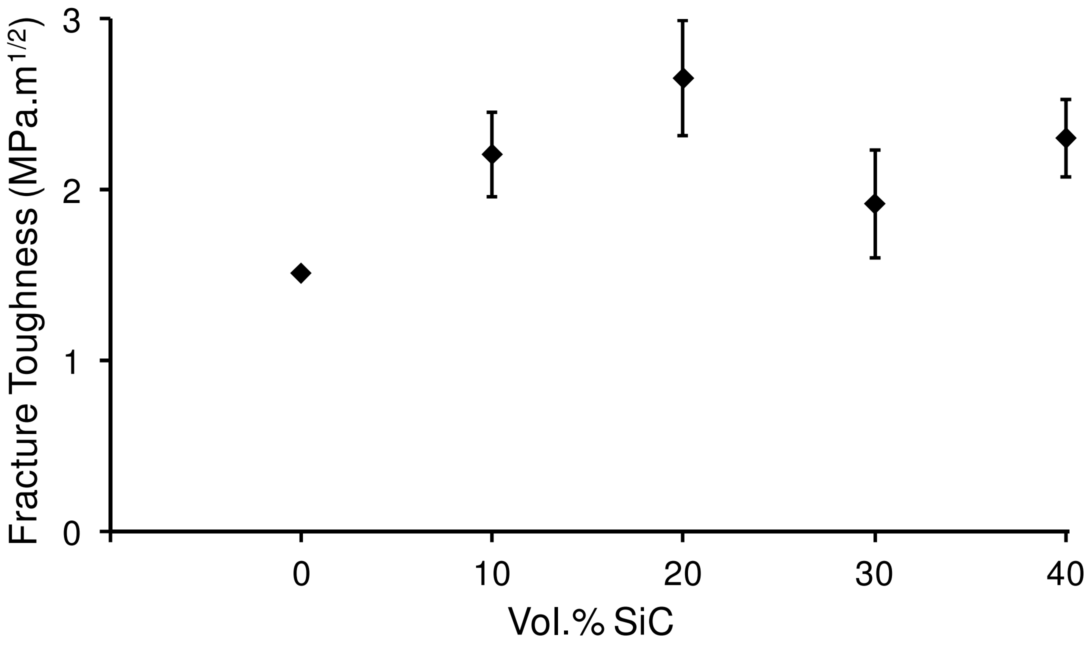

Fig. 3.9 Fracture toughness of ZrB_2-SiC composites as a function of reinforcement content.

The improvement in fracture toughness of composites can be attributed to two toughness improvement factors of the composites. The first factor is the high relative density of the composites with all the ZrB_2-SiC composites had a relative density greater than 99%. The second factor is the toughness improvement mechanisms like crack deflection, shearing of reinforced particles and SiC grain pull-outs that is observed in the composites. Whereas these toughening mechanisms are absent in monolithic ZrB_2. In ZrB_2 samples, the crack front was relatively straight without significant bending or deflection (Fig. 3.10(a)). However, the crack seems to propagate along boundaries of smaller grains (1-2 μm) indicating intergranular fracture feature. For ZrB_2-SiC composites, the indentation crack interacts with the reinforced SiC particles causing shear of the finer particles and crack getting deflected at the coarser particles (fig 3.10(b)). The fracture surface of the ZrB_2-SiC composites also shows predominantly intergranular fracture features with distributed depressions due to grain pull-outs (Fig. 3.3(b-c)) which is also a toughening mechanism in reinforced ceramic composites.

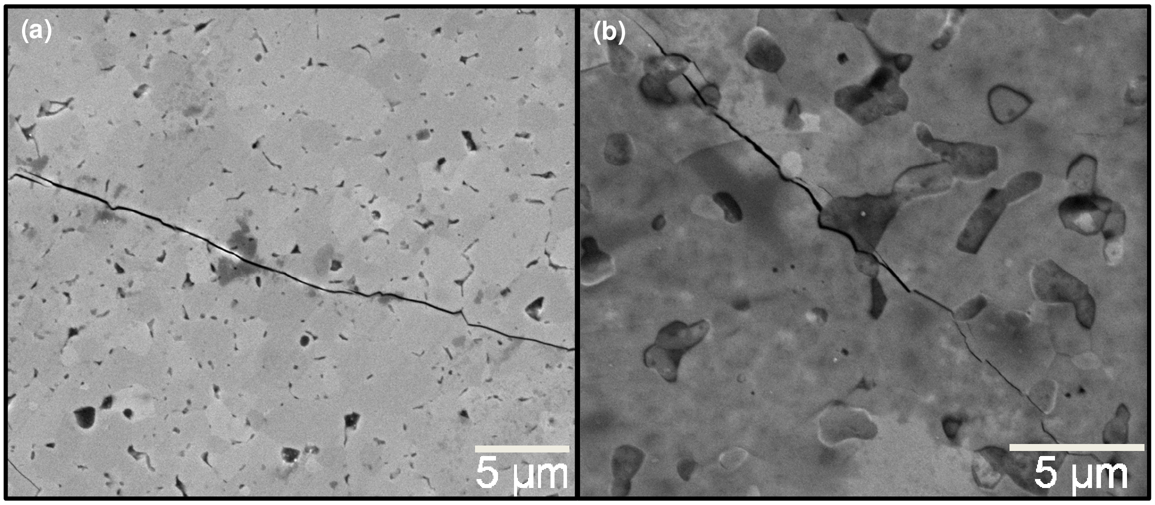

Fig. 3.10 High Magnification Crack Propagation and Toughening mechanism of (a) Monolithic ZrB_2 (b) 20 vol.% SiC.

3.1.4 Oxidation properties

The variation of TGA weight of ZrB_2 and ZrB_2-SiC samples with respect to temperature (25-1100˚C) is shown is figure 3.11. At high temperatures the samples oxidizes by reacting with air (that was used as carrier gas) to form oxide products. The increase in weight of the samples is attributed to the formation of oxidation products. As it can be seen from the figure that monolithic ZrB_2 had a maximum weight gain of 5.91% from its starting weight. Whereas the all the SiC composites has a low TGA weight increase of ~0.2 to 0.5% of the initial weight which is low compared to the monolithic ZrB_2 sample.

The 40% SiC composite has the least TGA weight gain of 0.19% followed by the 30% SiC which had a weight gain of 0.33%. The 10 and 20% SiC composites showed weight gain of 0.45 and 0.52% respectively.

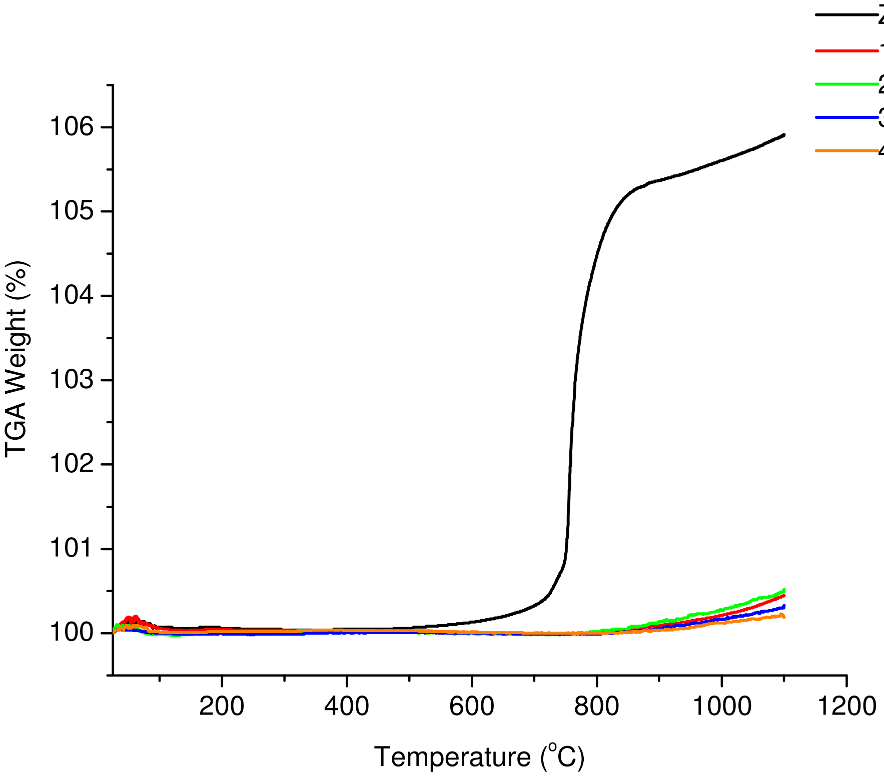

Fig. 3.11 TGA weight gain of ZrB_2 and ZrB_2-SiC composites.

It is evident from the TGA oxidation test that the addition of SiC has improved the oxidation resistance of the ZrB_2 ceramic. The monolith had lower oxidation resistance and was stable up to 500˚C and started to oxidize above that temperature. There was a steep increase in weight gain of ZrB_2 in the temperature range of 700 to 850˚C which is the indication of production of a non-protective pores B_2O_3 product of oxidation. This in accordance with the literature oxidation studies on ZrB_2 [7, 32].There was a continuous gain in weight for Zrb2 up to 1100˚C which is the peak TGA temperature indicating the low oxidation resistance and continuous production B_2O_3 up to the peak temperature. The rate of oxidation is low for the SiC reinforced composites. They did not show gain in weight up to a temperature of 800˚C which is 300˚C above that of the monolithic ZrB_2 indicating the oxidation resistance of the composites. Above this temperature there was a small weight gain in the composites up to 1100˚C. B2O3 and a small amount of SiO_2 are expected to be the oxide products in the composites. SiO_2 is protective passive oxide layer that is stable up to 1500˚C. The formation of SiO_2 is attributed to the improved oxidation resistance of the composites.

EDS and SEM analysis are needed to study the structural development of oxide products at different temperature ranges is needed for the better understanding of the oxidation mechanism involved in TGA. These analyses are not included in the current work. and are to be carried out as future works to broaden the scope of this study.

Table 3.1 lists the relative density and mechanical properties of monolithic ZrB_2 and ZrB_2-SiC ceramic composites.

Table 3.1 Relative density and mechanical properties of ZrB_2 and ZrB_2-SiC ceramic composites.

Sample	Relative density (%)	Hardness (GPa)	Fracture toughness ($MPa.m^{1/2}$)	Flexural strength (MPa)
ZrB_2	84.8	16.64±0.90	1.51±0.02	162±31
ZrB_2+10%SiC	99.1	19.38±0.13	2.21±0.25	553±07
ZrB_2+20%SiC	99.6	20.80±0.46	2.66±0.34	301±51
ZrB_2+30%SiC	99.7	21.44±1.27	1.92±0.32	431±39
ZrB_2+40%SiC	99.7	22.71±0.19	2.31±0.23	410±17

3.2 Spark Plamsa Sintering of CNT reinforced ZrB_2 Ceramic Composites

3.2.1 Relative density, Densification Mechanism and Microstructure

The relative density of monolithic ZrB_2 and ZrB_2-SiC composites as a function of reinforcement content is indicated in figure 3.12. For the same SPS processing parameters (sintering temperature of 1900°C, soaking time of 15 min, and pressure of 70 MPa) the 4 and 6 vol.% CNT composites had relative densities greater than 99%. The 2 vol.% CNT composites had a relatively low density of 95.3%. As explained earlier higher temperature and holding time is needed for better densification of monolithic ZrB_2. The improvement in densification of the CNT reinforced ZrB_2 composites can be attributed to particles rearrangement by applied pressure, necking and grain diffusion mass transfer mechanism caused by pulsed DC.

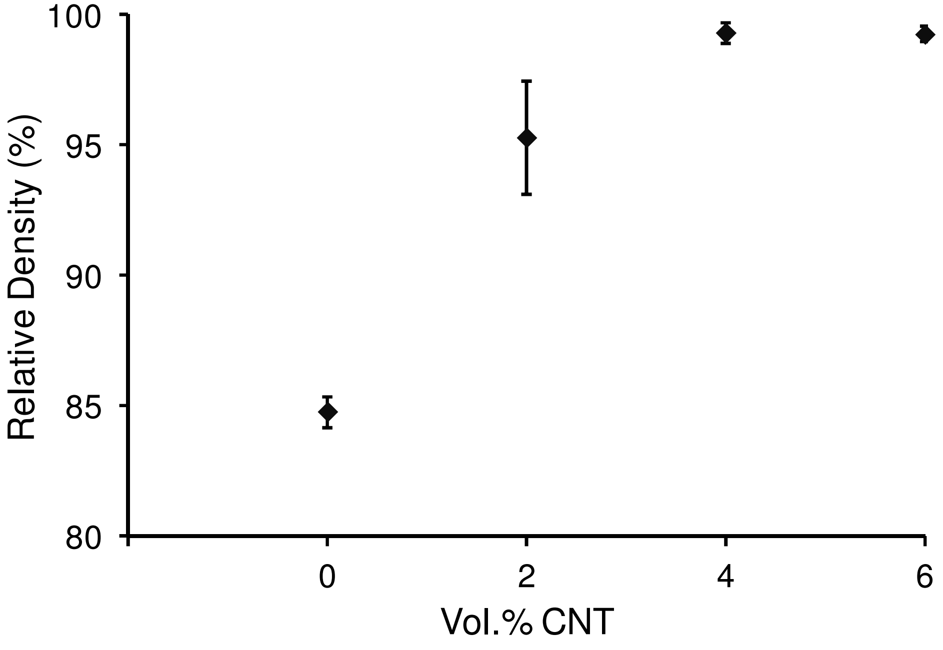

Fig. 3.12 Variation of relative density of ZrB_2-CNT composites with reinforcement content.

To understand the densification behavior of ZrB_2-CNT composites during SPS processing, the data on punch displacement was recorded during sintering. Fig. 3.13 shows the variation of punch displacement with sintering time during initial heating and soaking stages of sintering cycles. As shown in figure the densification cycle can be divided into three stages as Stage I which corresponds to particle rearrangement by applied pressure, Stage II corresponding to thermal expansion of the particles and the third and final stage named as Stage III which is the actual densification of the powder matrix facilitated by the reduction of surface curvature of the particles by applied temperature and simultaneous pressure causing a reduction in surface energy which drives the sintering mechanism. Joule heating in the powder particles and also discharges sparks in the gaps and contact area between the ZrB_2-ZrB_2 and ZrB_2-CNT particles drives the mass transfer process by necking of particles and volume diffusion leading to the densification of the composites.

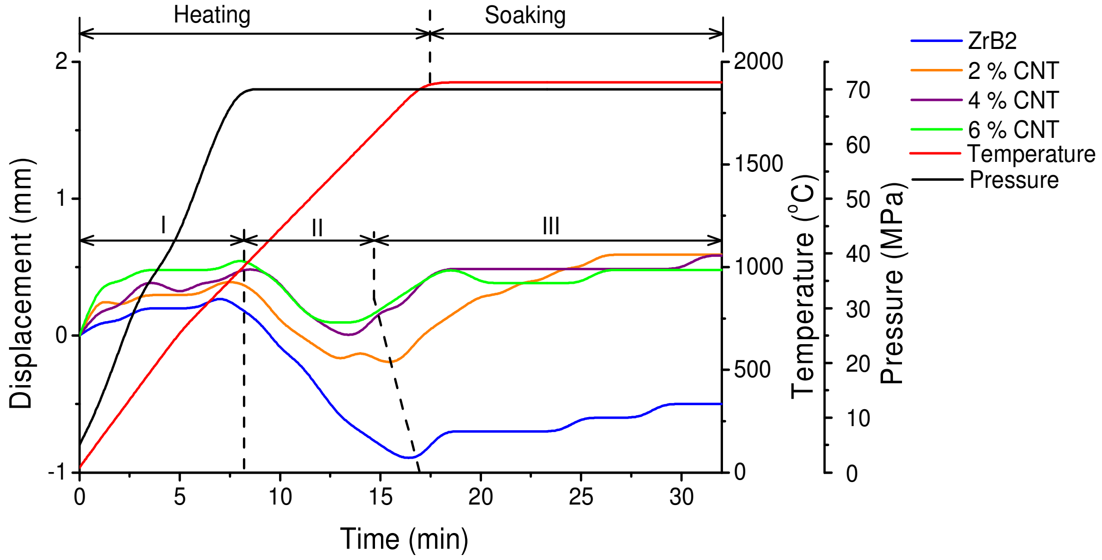

Fig. 3.13 Ram displacement, temperature and pressure profiles during heating and soaking stages of SPS sintering cycles for ZrB_2-CNT composites.

In figure 3.13 positive slopes indicates compression and negative slopes indicates expansion. The monolithic ZrB_2 as explained before does not have good particle rearrangement in stage I because of similar particles size (punch displacement of less than 0.25). Whereas the CNT reinforced composites had a punch displacement of ~0.5 mm. The lubrication property of CNT provides better particle reinforcement under applied pressure for the composites in stage I. The effect of lubrication is directly proportional to CNT content of the composites with 2 and 6 vol.% CNT composites having the least and maximum punch displacement in stage I. This helps in compacting the powder matrix enabling better densification. Stage II is the thermal expansion of the compact powder leading to negative punch displacement. Large thermal expansion is seen in monolithic ZrB_2 compared to the CNT reinforced composites. This could be due to the presence of pores in the monolithic ZrB_2 powder that expanded in stage II to leading to larger punch displacement for ZrB_2.

Stage III is the densification process induced by pulsed DC of spark plasma sintering creating localized joule heating under simultaneously applied pressure. Mass transfer induced densification takes place attributed by necking of adjacent particles enabling volume diffusion and grain boundary diffusion. The difference in thermal conductivities of ZrB_2 and CNT also helps in densification process. The thermal conductivity of isolated CNT could be as high as 3000 W/mK [123] which is far higher than the thermal conductivity of ZrB_2 which is reported to be 56 W/mK [122]. This huge difference in the thermal conductivities of CNT and ZrB_2 leads to very high non-uniform temperature gradient and local melting of particles within the interparticle contact areas improving densification. This is evident from the improvement of relative density directly proportional to CNT content in the composites. This temperature gradient also led to grain growth in the CNT composites which is explained later in this section. Also the stage II to stage III transition for the CNT reinforced composites was shifted to lower temperatures corresponding to ~1400 to 1700°C (t= 12-15 min). This indicates that the composites can start densification at a much lower temperature than the monolithic ZrB_2.

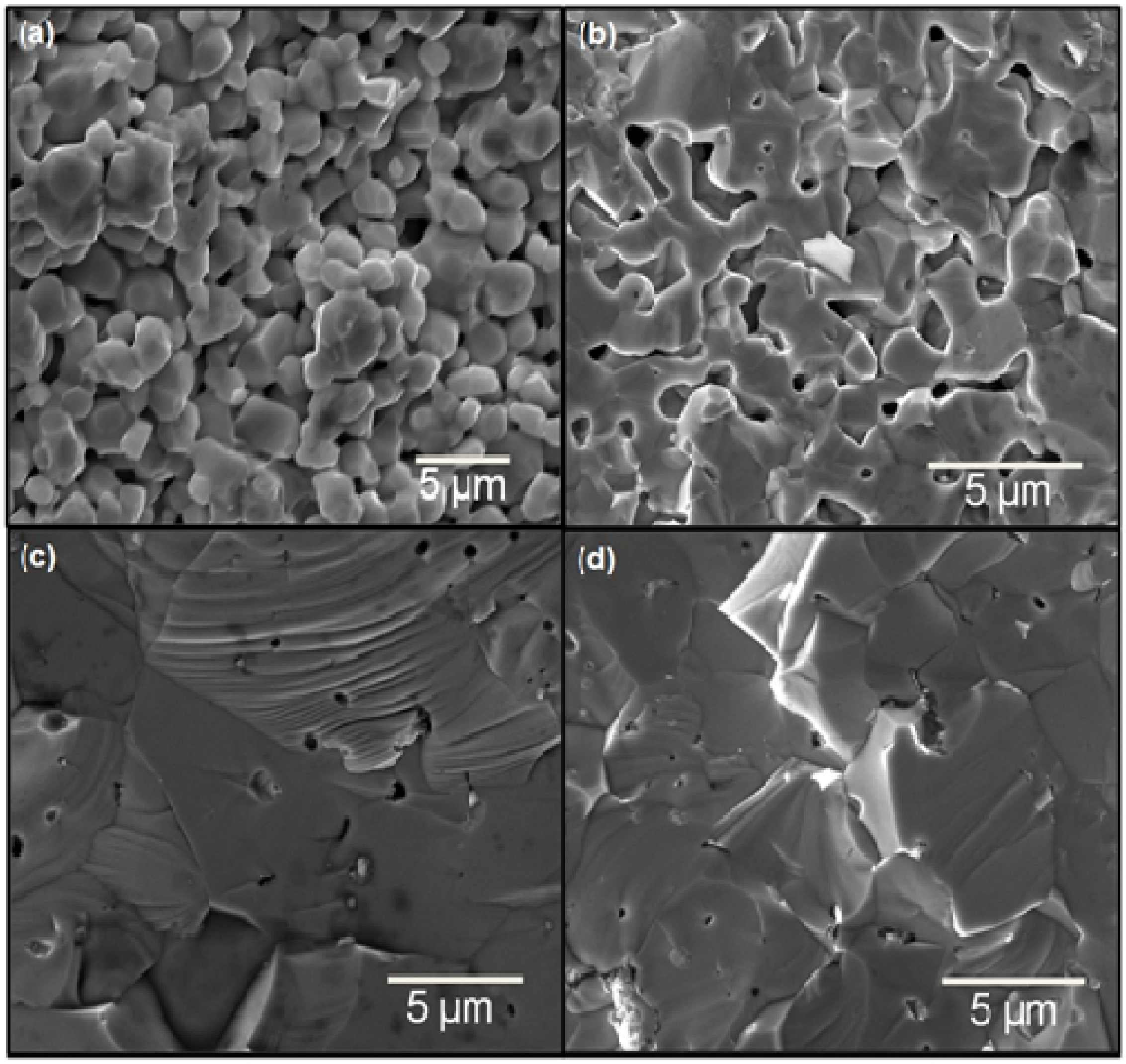

Fig. 3.14 SEM micrographs from the fracture surface of (a) ZrB_2, (b) ZrB_2+2% CNT, (c) ZrB_2+4% CNT, and (d) ZrB_2+6% CNT composites.

The microstructure of the monolith and CNT composites is studied with the help of SEM micrographs from the fracture surface of the composites. The SEM images support the relative density values calculate by Archimedes principle for the ZrB_2 and ZrB_2-CNT composites. As explained in earlier section the ZrB_2 has fine microstructure with grain size equivalent to starting particle size of 1-2 μm and distributed porosity accounting to its low relative density (Fig. 3.14(a)). The ZrB_2-CNT composites with 2% CNTs shows interconnected porosity on the fracture surface with slightly larger grains (2-3 μm) than starting particle size (Fig. 3.14(b)). The micrograph also shows regions of necking between adjacent particles. The necking between adjacent particles did not grow enough for complete volume diffusion to take place thus leading to the pores microstructure. The composites with higher CNT content (4 and 6%) showed dense fracture surface with distributed networks of CNTs (Fig. 3.14(c,d)). There was significant grain growth in the 4 and 6 vol.% CNT composites with grain size in the range of 5-10 μm. This increase in grain size for the CNT composites can be attributed by the high non-uniform temperature gradient and local melting of particles within the interparticle contact areas created due to the large difference in thermal conductivities of CNT and ZrB_2. The fracture surface also shows distribution of CNT networks both inside the grains and at the grain boundaries. The presence of CNT inside the ZrB_2 grains indicate the melting of ZrB_2 particles due to high localized heating as explained above and surrounds the CNTs. Later they consolidate into ZrB_2 grains encapsulating the CNTS. The composites also show smooth fracture surface morphology indicating predominant transgranular form of fracture mechanism with shear-band like fracture features. This may be attributed to dense and large grained microstructure. The voids in the fracture surface are attributed by CNT pull-out which is a toughening mechanism in CNT reinforced ceramic composites.

A high magnification micrograph clearly shows the CNT networks and protruded CNTs in the ZrB_2- 2 vol.% CNT composite sample (Fig. 3.15). The CNTs are distributed in the ZrB_2 matrix as networks rather than individual nanotubes. The agglomerates of CNTs indicate that ball milling did not produce uniform distribution of CNTs in the ceramic powder matrix. Better composite powder preparation methods like ultra-sonication or other colloidal processing is needed to obtain uniform distribution of CNT in ZrB2 ceramic matrix. Clearly, the CNTs were retained in the composites processed using SPS. The rapid heating rate (100˚C) and small soaking time (15 min) involved in SPS ensured better densification and eliminated the risk of CNT disintegration or strong interfacial reactions between the CNTs and ceramic matrix as encountered by Tian *et al.* [81].

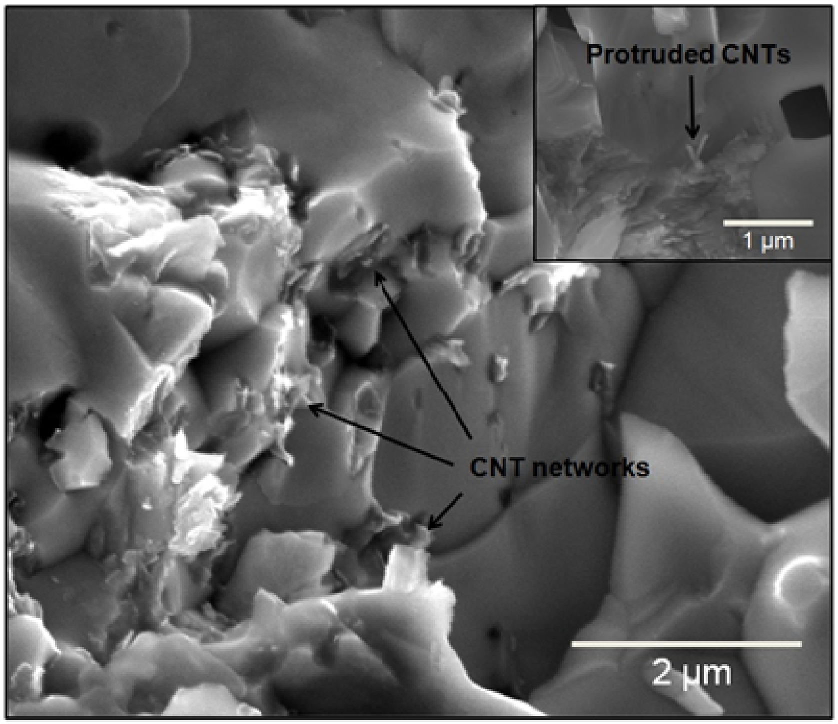

Fig. 3.15 A high magnification SEM micrograph from the fracture surface of ZrB_2-2 vol.% CNT composite showing CNT networks at the grain boundaries and inside the grain.

3.2.2 XRD and Raman Spectroscopy Analysis of CNT reinforced composites

XRD patterns from SPS sintered ZrB_2 and ZrB_2-CNT composites are presented in Fig. 3.16. For monolithic ZrB_2 and ZrB_2-CNT composites, all the characteristic peaks of ZrB_2 were identified. Note that characteristic (002) peak ($2\theta=26.2°$) corresponding to CNTs could not be found in the XRD patterns from the ZrB_2-CNT composites. This is probably due to very low volume fractions of CNTs in the ZrB_2 ceramic matrix. No additional peaks were observed suggesting sintering of two phase mixtures without any undesirable interfacial reactions.

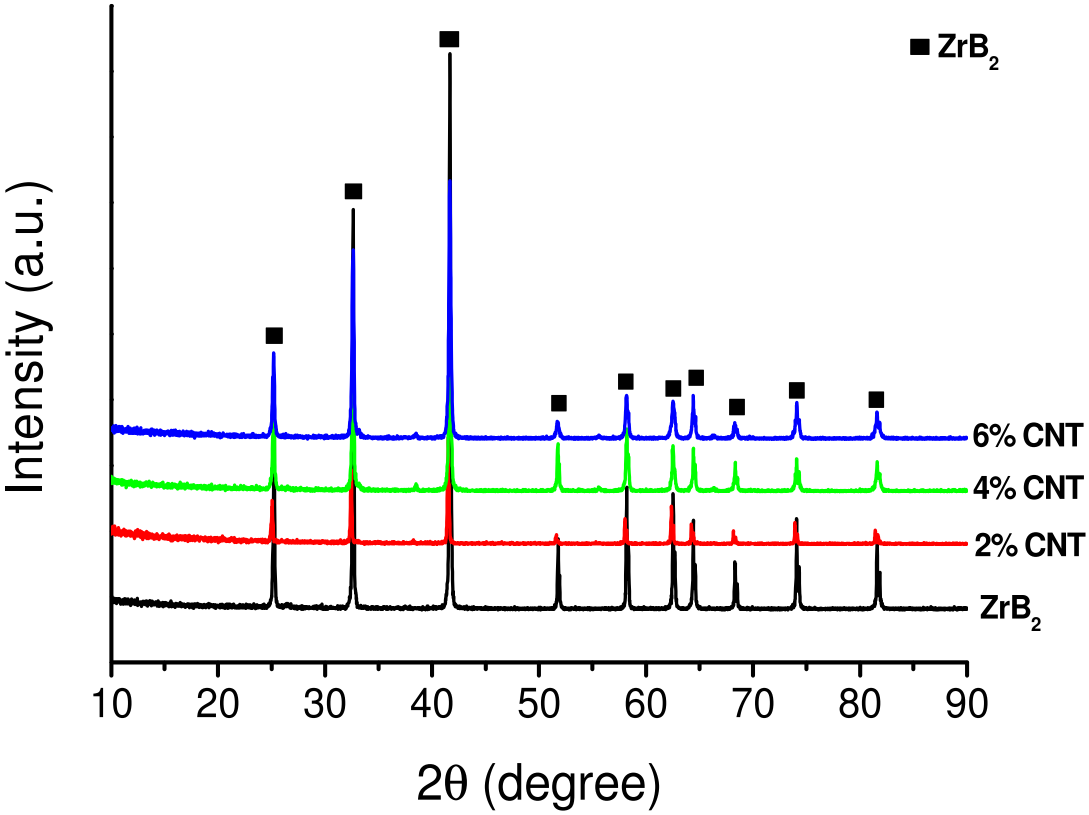

Fig. 3.16 XRD patterns from Spark Plasma Sintered ZrB_2 and ZrB_2-CNT composites.

A detailed characterization of the CNT networks in the ZrB_2-CNT composites using Raman spectroscopy was performed to understand the chemical and structural changes in the CNTs during the SPS process. The MWCNTs used in this work are too large in diameter to observe Radial Breathing Mode (RBM) features and hence, we focused on the characteristic Raman peaks of sp^2 hybridized carbon namely, D (~ 1350 cm^{-1}), G (~ 1580 cm^{-1}), D' (1620 cm^{-1}), and G' (~ 2700 cm^{-1}). The G and D are associated with the in-plane stretching of C–C and breathing modes, respectively, whereas G' and D' correspond to their respective second order phonon counterparts [69, 124-125]. The G band is the characteristic band of all sp^2 hybridized graphitic materials and is used to distinguish between different carbon nanostructures. The G' is a dispersive characteristic speak of all sp^2 hybridized graphitic materials the position of which is highly depended on the excitation laser energy and thus gets its name as a dispersive peak. The G' is used to study the electronic nature of the carbon nanotubes. The D and D' are called the disorder induced peaks and as the name suggests they are used as a measure to study the disorder or defects in CNT. The D and D' are not observed in the perfect graphite and they become active in the presence of defects and therefore these peaks are indicative of disorder in the sp^2 carbon materials. Fig. 3.17 depicts the Raman spectra of ZrB_2-CNT (2, 4, and 6 %) composites compared with ZrB_2, pristine MWCNTs, and sintered MWCNTs. ZrB_2 has no active Raman modes [126] and thus the spectra show the characteristic peaks of CNTs in the composites. The peak position of G, D, D and G is provided for all the spectra to get a clear understand the effect of high temperature sintering and the interaction of the CNTs with the ceramic matrix. It is evident from the spectra that the D, G, and G' bands have shifted to higher energies in case of sintered CNTs and ZrB_2-CNT composites. This high energy shift can be owed to: i) decrease in the average distance between defects [69, 124-125]; ii) the residual compressive stress on the CNT network imposed by the ceramic matrix [80, 127-129] that evolves during the cooling step (i.e., thermal contraction of ZrB_2 matrix surrounding CNTs).

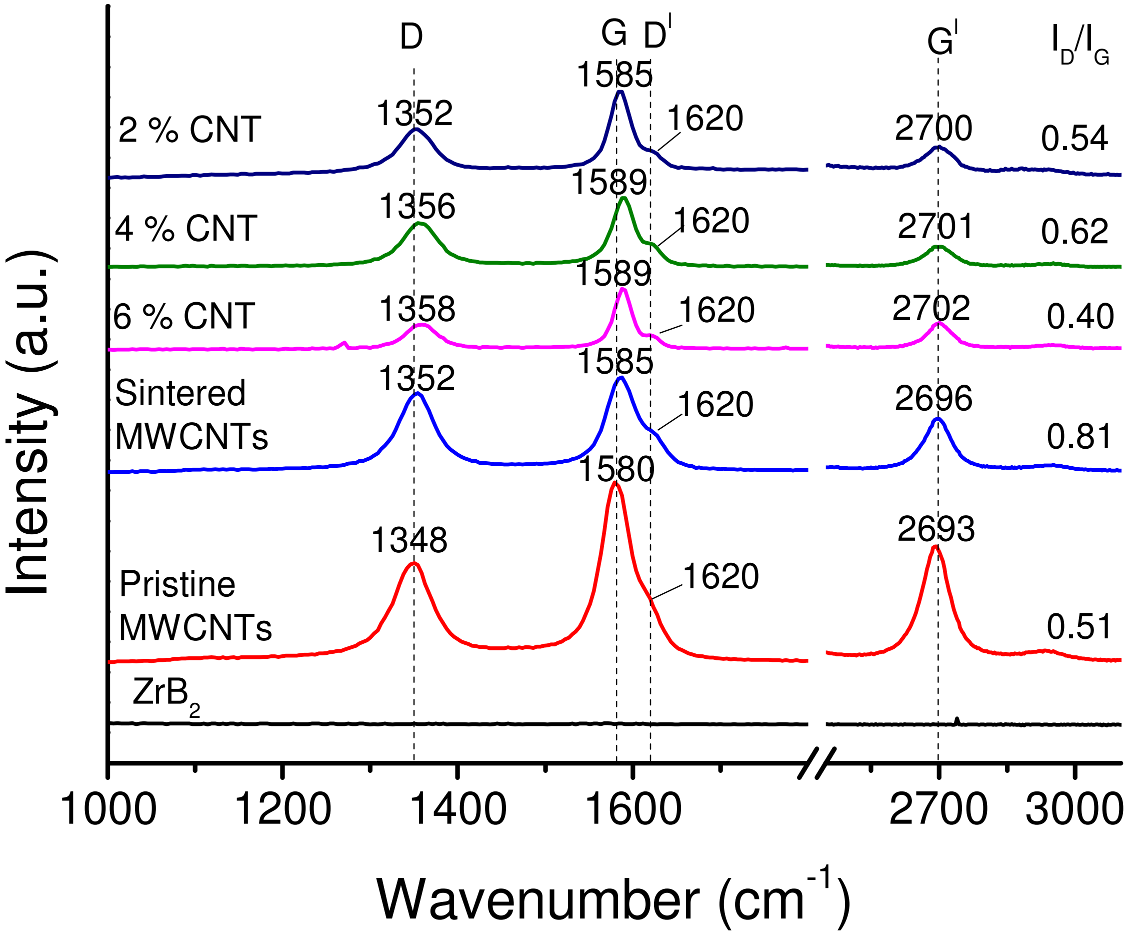

Fig. 3.17 Raman Spectra from ZrB_2-CNT composites showing in the frequency ranges 1000-1750 cm^{-1} and 2450-3000 cm^{-1}.

The ratio of intensities of D to G (I_D/I_G) is a way to quantify the density of defects or the degree of chemical damage in the CNTs [124-125]. From Fig. 3.17, it is obvious that the I_D/I_G has not varied significantly compared with pristine CNTs implying there is no significant defect formation during the SPS process. Indeed, the persistence of the G' band during the SPS process indicates structural consistency of sp^2 carbon [125]. The highest I_D/I_G value is 0.61 (6 % CNT). To study the impact of I_D/I_G ratio and peak position of G on the structural quality of CNT, the intensity ratio and peak position was compared with ion-bombarded glassy carbon. For 0.61 I_D/I_G, the G peak was found at 1565 cm^{-1} for ion-bombarded glassy carbon [125]. On the other hand, our G peak is found at 1589 cm^{-1} (being significantly higher than 1565 cm^{-1}) that suggests the high energy shift in our G peak is mainly due to stress. This argument is also supported by the Raman spectrum of sintered CNTs in Fig. 3.16, where I_D/I_G is 0.81 but G peak is only at 1585 cm^{-1} which is in agreement with Ref. 125. In addition, the shift in the peaks is higher in case of 4 and 6 % CNT than 2 % CNT composites. This observation is attributed by higher stress formation in the 4 and 6 % CNT cases due to denser ceramic matrix formation that inhibits stress relaxation. Therefore, our Raman findings corroborate that the structure of CNTs remain intact with insignificant defect formation during SPS process. Compressive stress is developed of in the CNTs possibly due to thermal contraction of the ceramic matrix during cooling causing a shift in the peak position of G band.

3.2.3 Mechanical Properties of ZrB_2-CNT composites

3.2.3.1 Micro Hardness

The variation of hardness of ZrB_2 and ZrB_2-CNT composites with the reinforcement content is shown in figure 3.18. The average hardness of the monolithic ZrB_2 is 16.64 GPa. There was no significant improvement in the hardness of the CNT reinforced ZrB_2 composites. In fact there was a small reduction in the micro hardness of ZrB_2-CNT composites. Among the composites the 4 vol.% CNT reinforced ZrB_2 had the highest hardness of 16.39±1.95 GPa. The 2 and 6 vol.% CNT reinforced ZrB_2 composites had hardness of 14.17±0.38 and 15.18±0.40 GPa respectively. The strengthening effect of CNTs was not evident in ZrB_2-CNT composites even though the CNT reinforcement resulted in significant improvement in the densification (relative density>95%). This can be attributed to the reason that CNTs are distributed in the ZrB_2 matrix in the form of dispersed networks instead of individual CNTs. Furthermore, the ZrB_2-CNT composites also showed significant grain growth. Better dispersion of CNTs in the ZrB_2 ceramic matrix would have improved the hardness of the composites.

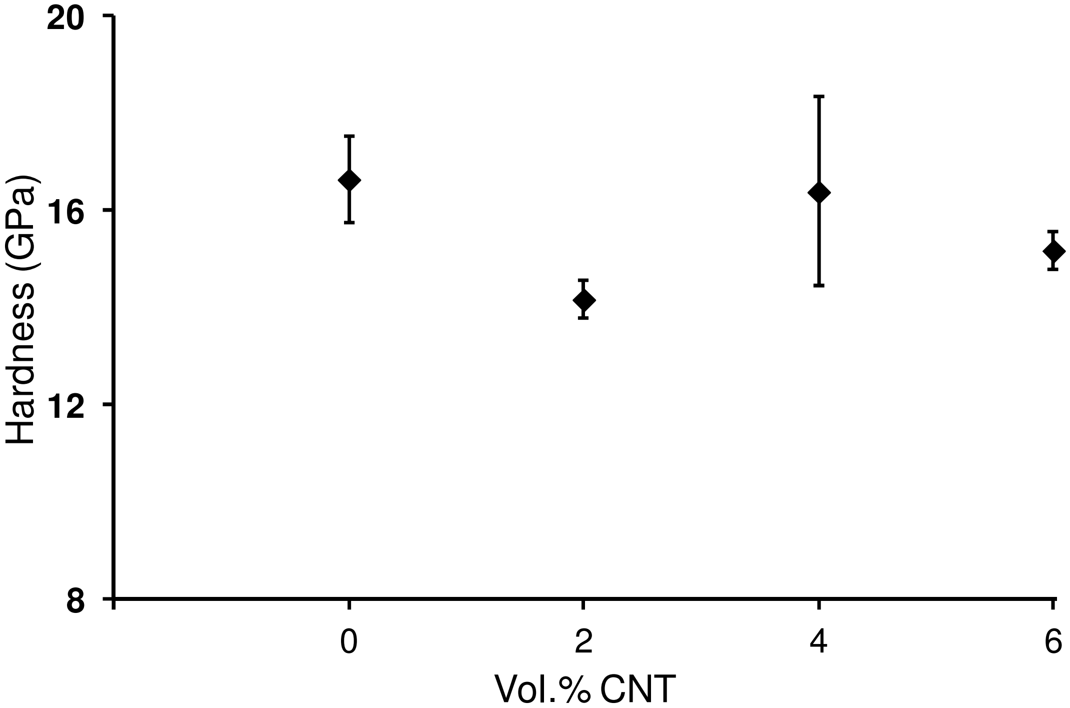

Fig. 3.18 Hardness of ZrB_2-CNT composites as a function of reinforcement content.

3.2.3.2 Flexural Strength

The flexural strength of monolithic ZrB_2 and ZrB_2- 2, 4 and 6 vol.% CNT composites is shown in figure 3.19. The monolithic ZrB_2 had flexural strength of 162±31 MPa and the CNT composites had flexural strength in the range of 150-315 MPa. The 4 CNT reinforced ZrB_2 composite had the highest flexural strength of 315±65 MPa and the 2 and 6 vol.% composites had flexural strength of 151±07 and 274±20 MPa respectively. The relatively low strength of the 2 vol.% CNT composites can be attributed to low relative density and distribution of CNTs as networks rather than as individual nanotubes. The fracture surface of the composites shows smooth surface morphology with shear band features indicating predominantly transgranular form of fracture for 4 and 6 vol.% composites and intergranular fracture for 2 vol.% composite. The improvement in the fracture strength of the 4 and 6 vol.% in spite of significant grain growth of ~5 to 10 μm is attributed to good relative density of >99% and CNTs pull out of the ceramic matrix which is a novel strengthening mechanism in CNT reinforced ceramic composites. The voids seen in the fracture surface in the CNT composites is attributed to CNTs pull-out. The high magnification image (3.15) from ZrB_2-CNT composites clearly showed pulled out CNTs and CNT networks both at the grain boundaries and inside the grains.

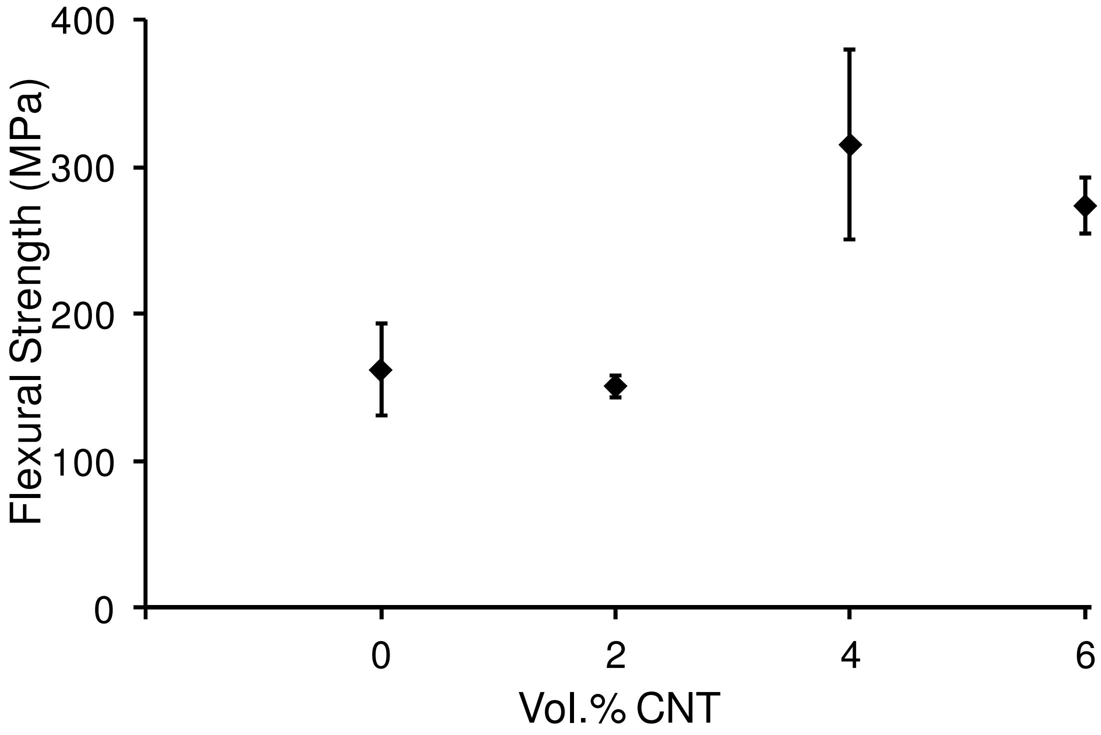

Fig. 3.19 Flexural strength of ZrB_2-CNT composites as a function of reinforcement content.

3.2.3.3 Fracture Toughness

Significant improvement in fracture toughness was observed in the ZrB_2-CNT composites compared to ZrB_2. The variation of fracture toughness with reinforcement content of CNT is shown in figure 3.20. The fracture toughness of monolithic ZrB_2 was 1.51±0.0247 $MPa.m^{1/2}$. The fracture toughness increased with increasing CNT reinforcement content and was in the range of 1.5-3.5 $MPa.m^{1/2}$. The ZrB_2-CNT composites reinforced with 6% CNTs exhibited highest fracture toughness of 3.53±0.47 $MPa.m^{1/2}$. The 2 and 4 vol.% CNT reinforced composites had toughness of 1.52±0.07 and 2.62±0.68 $MPa.m^{1/2}$ respectively.

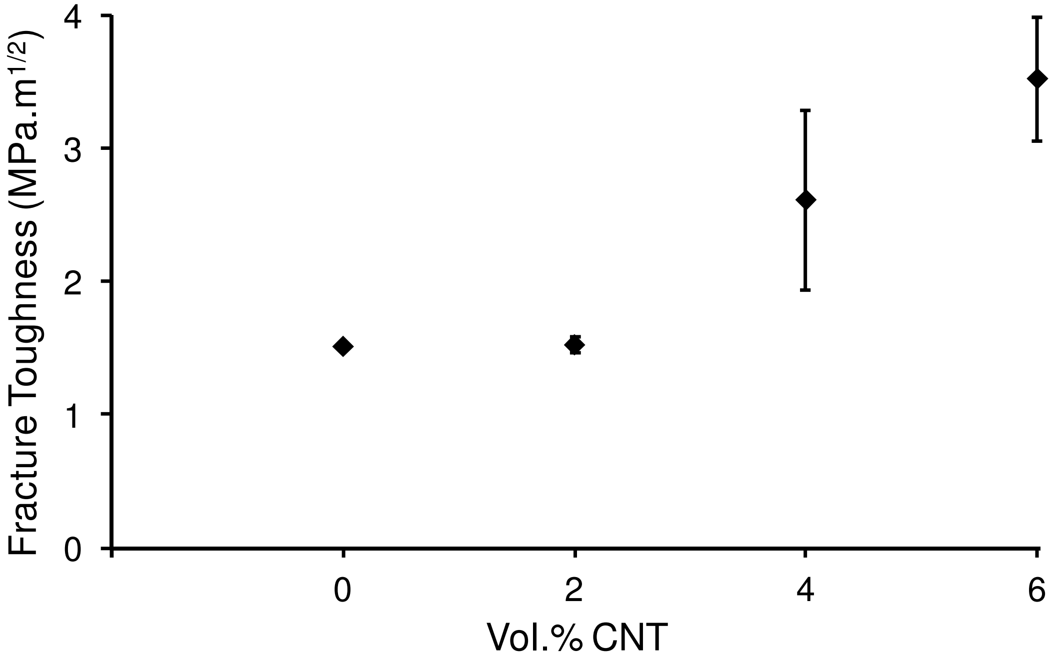

Fig. 3.20 Fracture toughness of ZrB_2-CNT composites as a function of reinforcement content.

The significant improvement in fracture toughness of the CNT reinforced ZrB_2 composites is attributed to better relative density of the composites and novel toughening mechanisms like CNT pull-out crack deflection by the CNT networks. Figure 3.21 shows the indentation crack propagation in monolithic ZrB_2 and 4 vol.% CNT composites. In ZrB_2 samples, the crack front was relatively straight without significant bending or deflection whereas the crack is deflected by the CNT networks in the composites making the crack to follow a more torturous path and thus improving the fracture toughness of the composites. As seen in fig 3.21, the propagating crack encounters the networks of CNTs and goes around the networks. As the ZrB_2-CNT composites with very low level of reinforcement (up to 6% CNTs) exhibited higher fracture toughness than that for ZrB_2-

SiC composites (with up to 40% SiC), it seems that CNTs are more effective in toughening the ZrB_2-based UHTCs. Better dispersion of CNTs in the ZrB_2 ceramic matrix is further expected to improve the toughening effects.

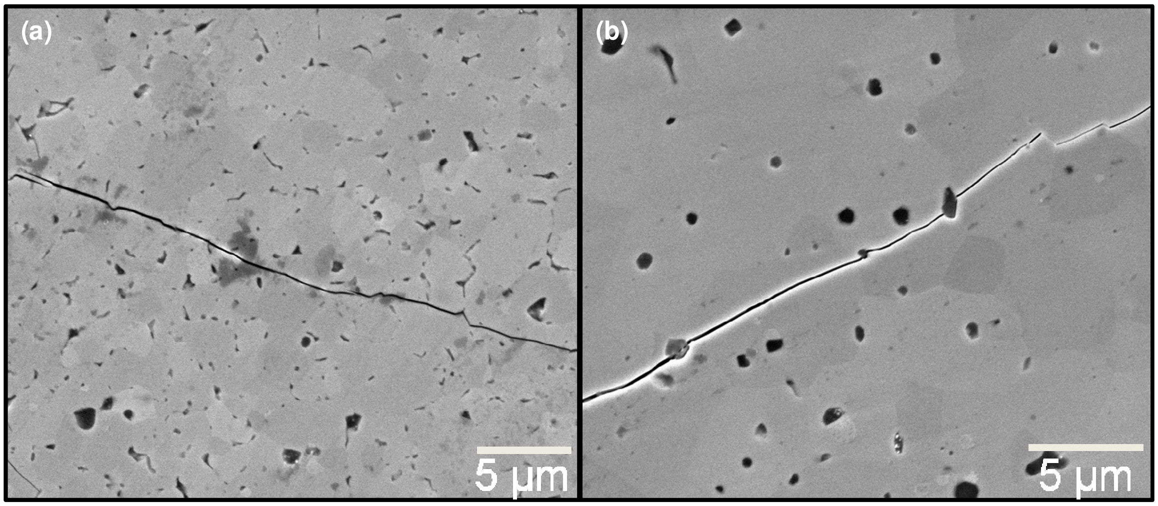

Fig. 3.21 High Magnification Crack Propagation and Toughening mechanism of (a) Monolithic ZrB_2 and (b) 4% CNT

Table 3.2 lists the relative density and mechanical properties of monolithic ZrB_2 and ZrB_2-CNT ceramic composites.

Table 3.2 Relative density and mechanical properties of ZrB_2 and ZrB_2-CNT ceramic composites.

Sample	Relative density (%)	Hardness (GPa)	Fracture toughness (MPa.m$^{1/2}$)	Flexural strength (MPa)
ZrB_2	84.8	16.64±0.90	1.51±0.02	162±31
ZrB_2+2%CNT	95.3	14.17±0.38	1.53±0.07	151±07
ZrB_2+4%CNT	99.3	16.39±1.95	2.62±0.68	315±65
ZrB_2+6%CNT	99.3	15.18±0.40	3.53±0.47	274±20

3.3 Spark Plamsa Sintering of GNP reinforced ZrB_2 Ceramic Composites

3.3.1 Relative density, Densification Mechanism and Microstructure

Figure 3.22 shows the relative density of ZrB_2 and ZrB_2-GNP composite samples with respect to the volume percentage of reinforcement. The monolithic ZrB_2 and 2 percentage GNP composites had an average relative density of ~85%. For similar SPS processing the 4 and 6 percent composites exhibited better relative density. The 4 and 6 percentage samples showed a relative density of ~97%. The improvement in densification of the GNP reinforced ZrB_2 composites can be attributed to particles rearrangement by applied pressure, necking and grain diffusion mass transfer mechanism caused by pulsed DC.

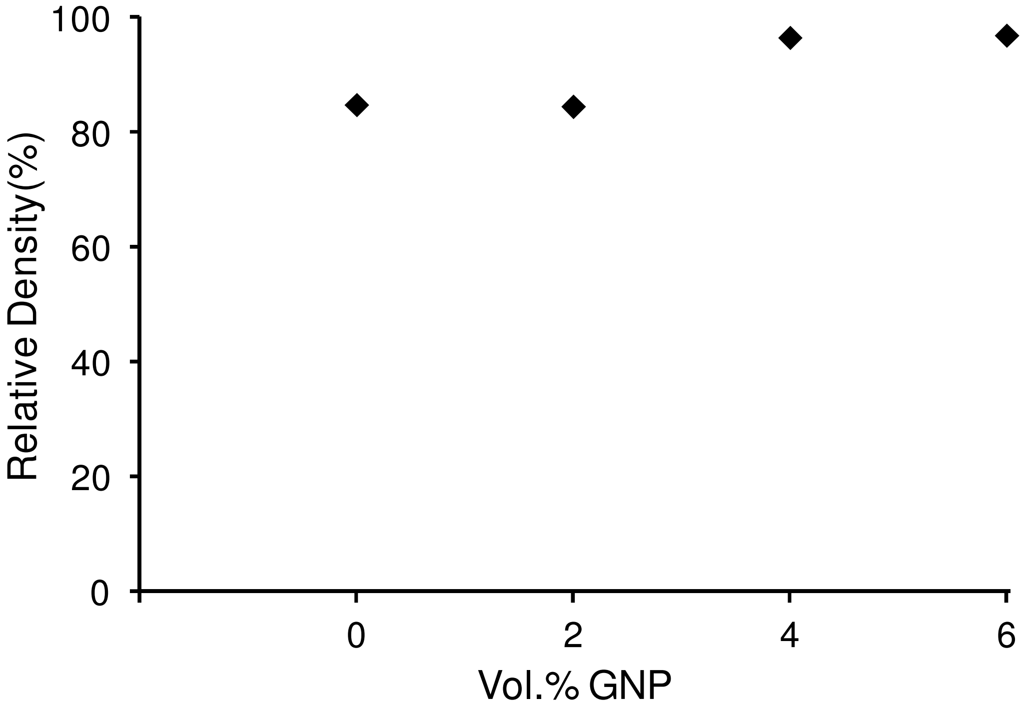

Fig. 3.22 Variation of relative density of ZrB_2-GNP composites with reinforcement content.

Similar to the SiC and CNT composites, the SPS ram displacement was studied for the GNP reinforced ZrB_2 ceramic composites (fig 3.23). The GNP reinforced composites had better punch displacement than the monolithic ZrB_2 during stage I. Graphene is an excellent lubricant and this lubricating effect aids in better rearrangement of the ceramic matrix. It can be seen from the figure that this phase of compression is hugely influenced by the volume percentage of GNP reinforcement. 2, 4 and 6 percent GNP composites had a punch displacement of ~0.6, ~0.8 and ~1mm respectively whereas monolithic ZrB_2 had small punch displacement of ~0.25mm due to lack lubrication. The punch displacement improves with increase in GNP content thus indicating the lubricating effect of GNP in rearranging the ZrB_2 particles. The sliding of hard ZrB_2 particles over the graphene nano platelets can cause shearing and exfoliation of the GNP into fewer layers.

The second stage is the thermal expansion of the compact powder leading to negative punch displacement. The third and final stage is the punch displacement due to densification caused by the pulsed DC and simultaneous pressure. Mass transfer induced densification takes place attributed by necking of adjacent particles enabling volume diffusion and grain boundary diffusion. The difference in thermal conductivities of ZrB_2 and GNP helps in densification process. The thermal conductivity of GNP could be as high as 4840 W/mK [130] which is far higher than the thermal conductivity of ZrB_2 which is reported to be 56 W/mK [122]. This huge difference in the thermal conductivities of GNP and ZrB_2 leads to very high non-uniform temperature gradient and local melting of particles within the interparticle contact areas improving densification. This is evident from the improvement of relative density directly proportional to GNP content in the composites. Thus lubrication effect and thermal conductivity mismatch between GNP and ZrB_2 led to the densification of the composites.

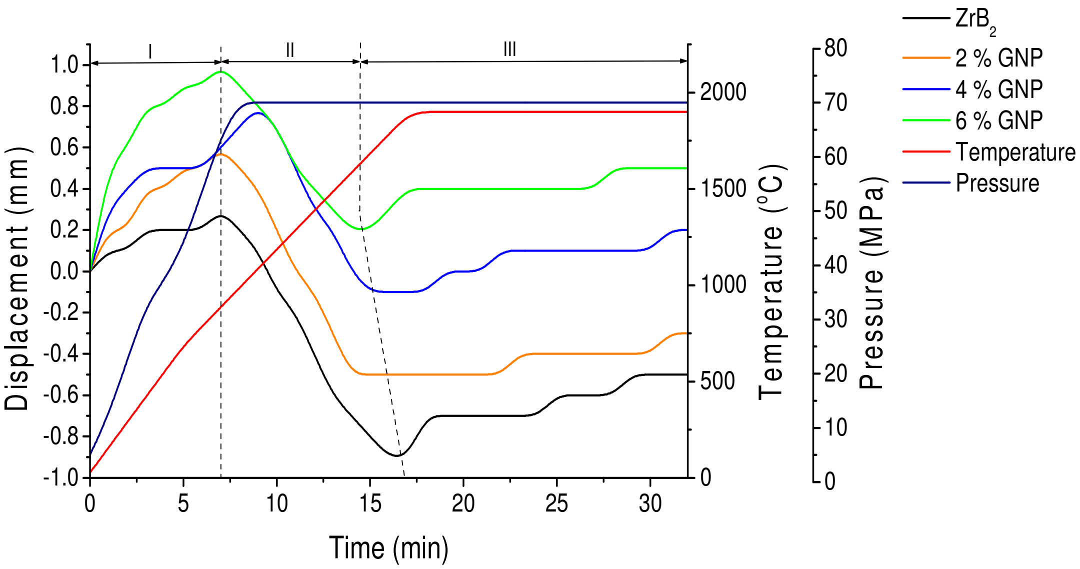

Fig. 3.23 Ram displacement, temperature and pressure profiles during heating and soaking stages of SPS sintering cycles for ZrB_2-GNP composites

The SEM micrographs from the fracture surface of the ZrB_2 and GNP composites are shown in figure 3.24. As seen from fig. 3.24(a, b) the monolithic ZrB_2 and 2% GNP composite has uniformly distributed porosity accounting for their low relative density. Figure 3.24(b) also shows the presence of GNP on the fracture surface of 2% composite. The monolithic ZrB_2 and 2% composites had an average grain size of 2.1 and 2.35µm respectively which is comparable with the starting particle size of 1-2µm. The 4 and 6% GNP composites showed a dense microstructure with the wrapping of GNP along the grain boundaries fig. 3.24(c, d). The micrograph also indicates that there is slight grain growth in case of the 4 and 6% composites. They had an average grain size of 4.69 and 4.05μm respectively. This small grain growth facilitated the elimination of pores in the composites. The SEM micrographs corroborates with the calculated relative density of the samples. The grain growth in the GNP reinforced composites is due to the high non-uniform temperature gradient and local melting of particles within the interparticle (GNP and ZrB_2 particles) contact areas improving densification. The 2 vol.% composite shows intergranular fracture whereas the 4 and 6 vol.% composites shows predominantly transgranular fracture features attributed by dense and large grained microstructure. This observation is similar to that of CNT composites.

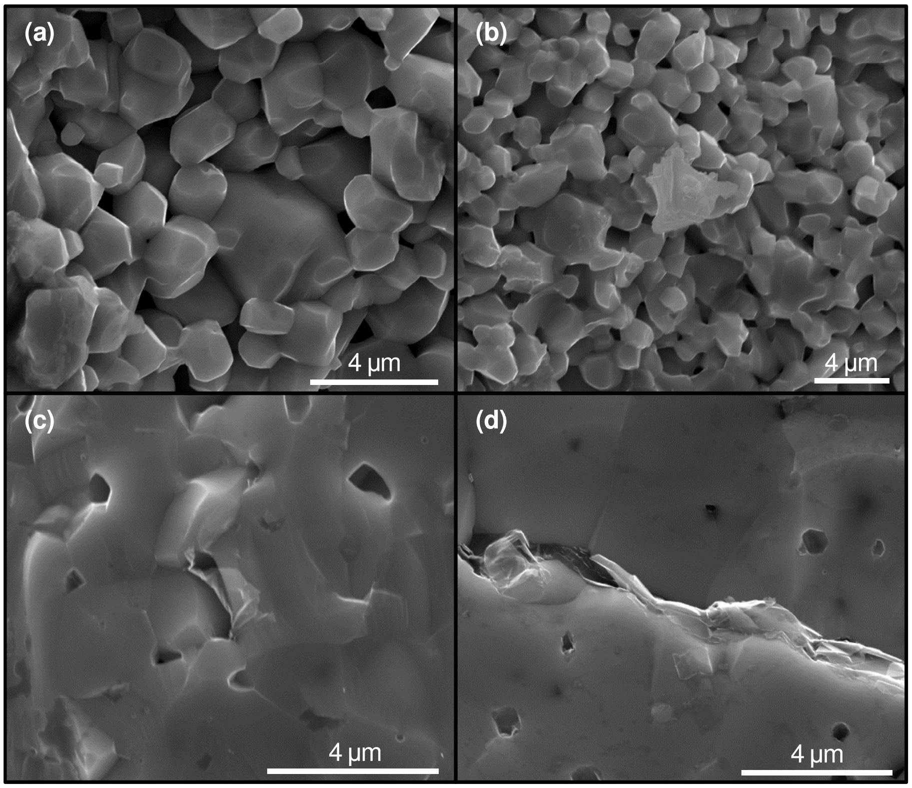

Fig. 3.24 SEM micrographs from the fracture surface of (a) ZrB_2, (b) ZrB_2+2% GNP, (c) ZrB_2+4% GNP, and (d) ZrB_2+6% GNP composites.

Figure 3.25 shows the high magnification SEM images of the GNP wrapping along the grain boundaries of the 4 and 6% composites. This kind of wrapping of the GNP will improve the strength and toughness of the ceramic composite. It can be seen from fig. 3.25(b) that a small amount of ZrB_2 particle that has melted and consolidated on the graphene platelets, which survives as proof for the local melting of ZrB_2 due to high localized heating caused by thermal conductivity mismatch between GNP and ZrB_2. These SEM micrographs provide clear evidence for the survival of GNP under high SPS parameters. The fractographic analysis and strengthening mechanisms of the composites is explained in detail in the mechanical properties section.

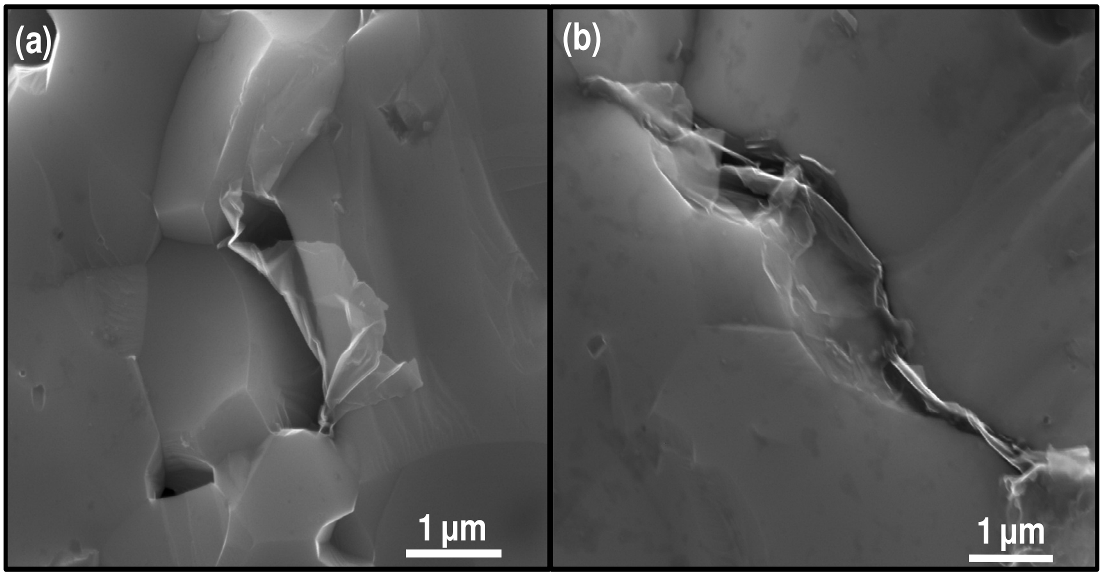

Fig. 3.25 High magnification SEM micrographs showing (a)wrapping of GNP along the grain boundaries in 4% GNP composite, (b) wrapping of GNP along the grain boundaries and localized melting of ZrB_2 in 6% GNP composite.

3.3.2 XRD and Raman Spectroscopy Analysis of GNP reinforced composites

X-ray diffraction (XRD) was carried out on the monolithic ZrB_2 and GNP composites (fig. 3.26). All the characteristic peaks of ZrB_2 were indentified, but the characteristic (002) peak of graphene at 2θ=26.6˚ was not found in the XRD pattern. This is accounted by the low volume fraction of GNP reinforcement. There were no unidentified peaks in the spectra indicating there were no undesirable interfacial reactions taking place during sintering.

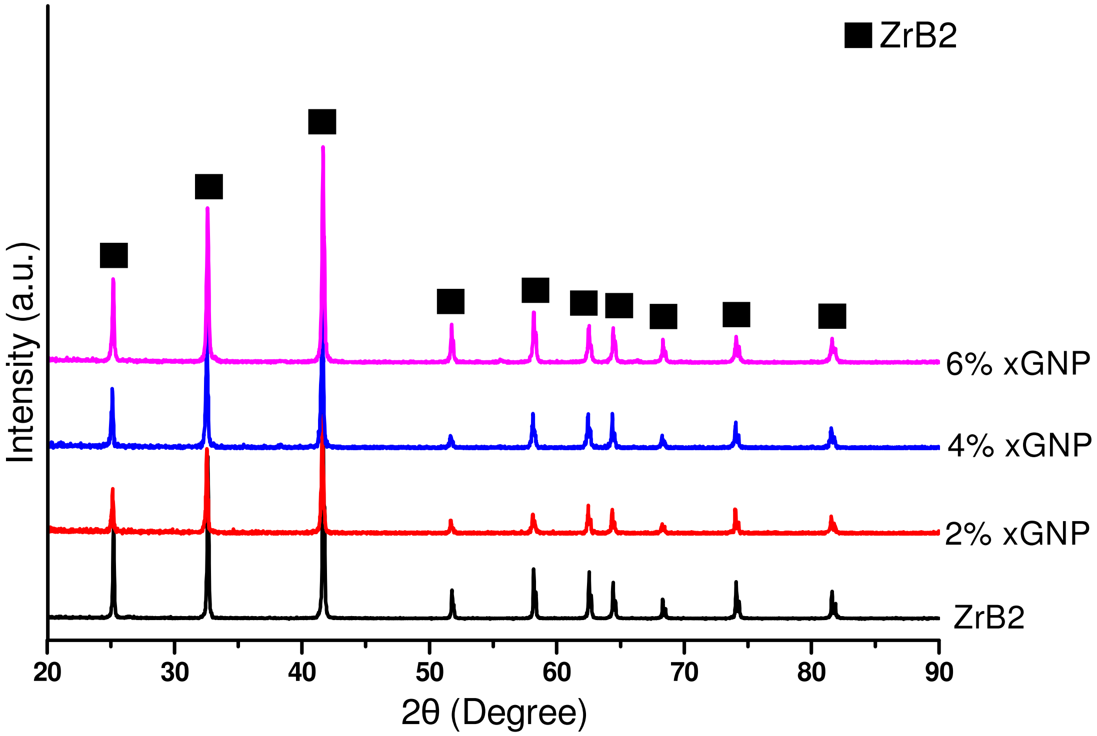

Fig. 3.26 XRD patterns from Spark Plasma Sintered ZrB_2 and ZrB_2-GNP composites.

We employed Raman spectroscopy to characterize ZrB_2-GNP composites. Raman acquisitions reveal the state of GNPs during the fabrication of composites. A typical graphitic carbon exhibit characteristic Raman peaks at D (~ 1350 cm^{-1}) and G (~ 1580 cm^{-1}) representing in-plane stretching and breathing modes, respectively, while the peaks at D' (~ 1620 cm^{-1}) and G' (~ 2700 cm^{-1}) are attributed to their respective higher order modes [41-43]. The modes corresponding to D and D' peaks are forbidden in the perfect sp^2 hybridized carbon due to symmetry. However, the presence of defects creates structural disorder that allows the breathing mode [41-43]. Hence, the D and D' peaks are observed only in graphitic carbon with disorder in its crystal structure. In the present study, we analyzed the characteristic Raman peaks of GNP at the fractured surfaces of the composites.

Figure 3.27a shows the Raman spectra of ZrB_2-GNP (2, 4 and 6 %) composites along with sintered GNP and ZrB_2. It is obvious from the Raman spectrum of ZrB_2 that it has no Raman-active vibrational modes in the frequency range of 1000-3000 cm^{-1}. Hence, the Raman spectra acquired from the composites exhibit the characteristic peaks of GNPs. Further, it is apparent that the D and G peaks in ZrB_2-GNP composites has shifted to higher energy, while the G' band has shifted to lower energy. The position of G and G' peaks are influenced by the following factors: i) density of defects in the GNP incurred during composite processing [43], ii) the thermal residual stress [44-46] that evolves during the cooling step (i.e., thermal contraction of ZrB_2 matrix surrounding GNPs), and iii) reduction in number of graphene layers (nGLs) [47-48].

A routinely used measure of density of defects in graphitic carbon materials is the ratio of intensities of D to G peaks (I_D/I_G) [41,43]. I_D/I_G values for GNP in ZrB_2-GNP (2, 4 and 6 %) composites, sintered GNP, and pristine GNP are displayed in Fig. 6a, (in fact, these values are close to average values of I_D/I_G). It is evident from the values of I_D/I_G that the average density of defects has increased by more than 4 times in 2 and 4 % composites. The density of defects is comparatively higher in 2 % than 4 and 6 % GNP composites and it scales inversely with the concentration of GNPs. In general, high temperature (>1600 °C) sintering of nanocrystalline graphite increases the average crystallite size [49]. This situation is directly observed in sintering of pure GNP. The I_D/I_G value of sintered GNP is close to zero (Fig. 3.27a) which is reminiscent of crystalline graphite. This point is further corroborated by G peak position being at 1581 cm^{-1} (Fig. 6a), which is in close agreement with literature [43].

Hence it is inferred that, I_D/I_G has increased for ZrB_2 composites because of chemical interaction between GNP and ZrB_2 matrix at high processing temperature (1900 °C) in SPS. I_D/I_G is higher at low concentrations of GNP possibly due to two reasons: i) less GNP aggregation and therefore, more carbon surface interaction with ZrB_2 per GNP; and ii) higher multiplication of GNPs due to exfoliation at lower GNP concentration. The exfoliation of GNP provides more GLs in contact with ZrB_2 matrix in 2 and 4 % GNP composites and it will result in a higher I_D/I_G [50]. This point is supported by the position of G and G' peak.

In addition, the G peak frequency in ZrB_2-GNP (2, 4 and 6 %) for corresponding I_D/I_G values is expected to decrease simultaneously with increasing concentration of GNP [43]. According to Ferrari *et al.*, when the I_D/I_G value increases from 0 to 2 due to increasing concentration of defects in nanocrystalline graphite, a high energy shift of the G peak from 1580 to 1600 cm^{-1} is observed concomitantly [43]. On the contrary, we observe the G peak frequencies at1584 and 1585 cm^{-1} for 2 and 4 % GNP, respectively (Fig. 3.27a). This shift is lower than the expected G peak shift by 6 and 5 cm^{-1}, respectively (estimated from Ref. 43 using corresponding I_D/I_G values of 2 and 4 % GNP). This discrepancy is due to reduction in nGLs in GNP of 2 and 4 % that occurred due to exfoliation [50-51]. On the other hand, the G peak of 6 % GNP composite (at 1588 cm^{-1}) has shifted to higher energy than expected G peak that is suggestive of the residual compressive stresses acting on GNP incurred during thermal contraction of ZrB_2 matrix [45-47]. The thermal stresses are more prominent in 6 % than 2 % GNP composite due to higher densification of the ceramic matrix. Concurrently, we observe a higher frequency shift in the D peak in 6 % composite due to residual compressive stresses.

In order to investigate the process of exfoliation we focussed on the G' band. It is evident from Fig. 3.27a, that the G' band of the composites has shifted to lower energy. This lower shift in G' band implies that the nGLs has decreased [50-51]. Alternatively, the shift in the G' peak is also possible due to chemical damage incurred during the high temperature processing of composites. In the ZrB_2 and GNP composites, the possible chemical damage could be due to: i) formation of a complex compound of Zr, B and C or ii) doping of GNP with B atoms. Both possible chemical interactions will induce p-type doping in GNP that will lead to high energy shift in G' band [52]. On the other hand, we observe a low energy shift in the G' band that suggests reduction in nGLs has the dominant influence on the G’ band frequency.

To further investigate the origin behind exfoliation of graphene, we acquired Raman spectra in ball-milled GNP with and without ZrB_2 powder as shown in Fig. 3.27b.

The lower energy shift in the G' band indicates a decrease in nGLs during ball-milling. In addition, the trend in I_D/I_G as well as G peak frequency suggests that the ball-milling has induced minimal damage. Additional shift in the G' band of sintered composite suggests further decrease in nGLs during SPS processing of the ball-milled mixture of ZrB_2 and GNP

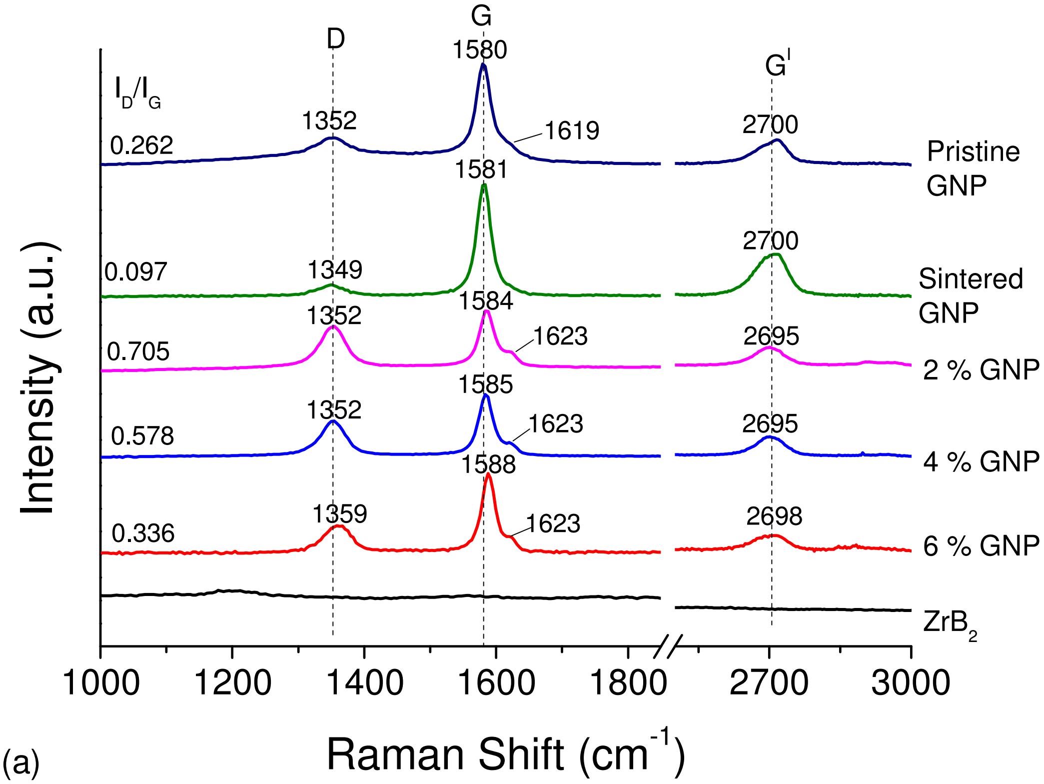

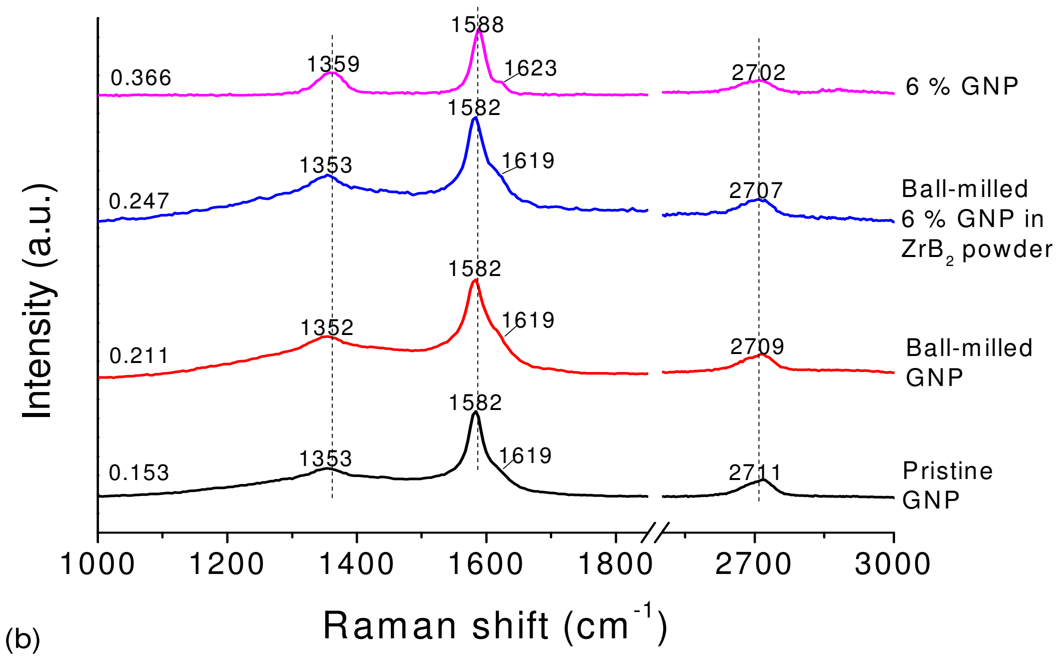

Fig. 3.27 Raman spectra of (a) ZrB_2 - 2, 4, and 6 % GNP composites, ZrB_2, pristine GNPs, and sintered GNPs. (b) Raman spectra of ball-milled GNP and ZrB_2 - 6% GNP composite powder, pristine GNP and sintered 6 % composite.

3.3.3 Mechanical Properties of ZrB_2-GNP composites

3.3.3.1 Micro Hardness

Figure 3.28 shows the variation of hardness with reinforcement content of GNP. There was no significant improvement in the hardness of the composites. In fact the monolithic ZrB_2 had the highest average hardness of 16.64±0.90 GPa and among the composites the 4% GNP composites had the highest average hardness of 15.9±0.84 GPa. The 2 and 6% GNP composites exhibited a lower average hardness of 13.53±0.24 and 14±0.6 GPa respectively. The lower hardness of the 2% composite is accounted by the well distributed porosity causing low relative density. Whereas the 4 and 6 vol.% GNP composites showed better hardness due to relatively better density. Better dispersion of GNP in the ceramic matrix is expected to improve the hardness.

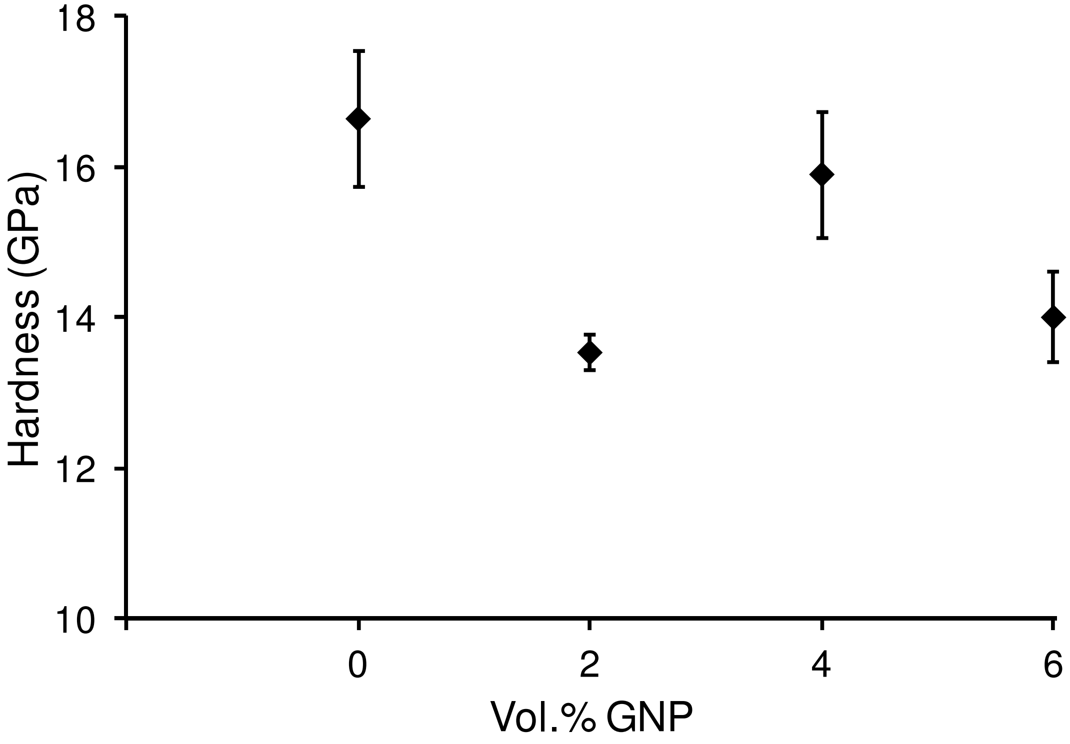

Fig. 3.28 Hardness of ZrB_2-GNP composites as a function of reinforcement content.

3.3.3.2 Flexural Strength

All the composites showed better strength and toughness compared to the monolithic ZrB_2 which had flexure strength of 162±31 MPa. The 6% GNP composite had the highest average strength of 316±85 MPa which is ~ 96% more than the monolithic ceramic samples. The 2 and 4% composites had an average strength of 204±34 and 219±23 MPa.

Figure 3.29 shows the variation of strength with respect to reinforcement content. The significant improvement in strength can be attributed by fairly uniform distribution of GNP in the ceramic matrix; strengthening of composite by sheet wrapping of GNP along the grain boundaries resisting GNP pull-out. The better densities of the composites also contributed to strengthening.

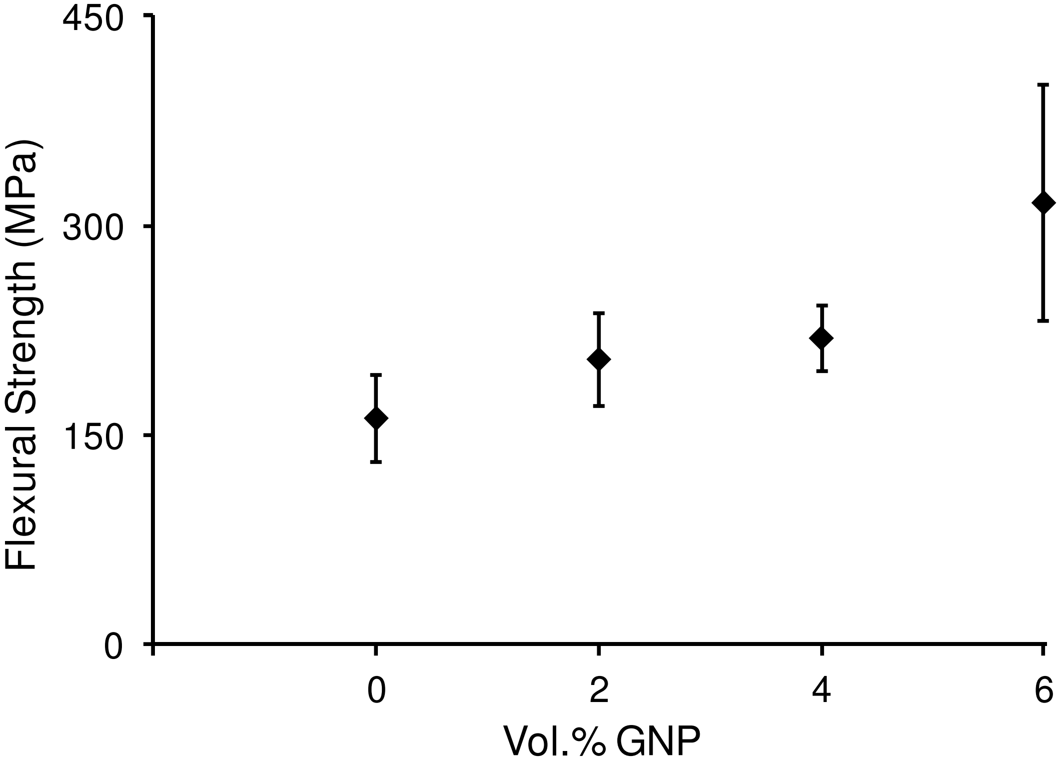

Fig. 3.29 Flexural strength of ZrB_2-GNP composites as a function of reinforcement content.

It can be noted that for almost similar relatively density between the ZrB_2 and 2% composite, the 2 vol.% GNP composite exhibited better strength. This improvement in 2% composite is mainly due to the strengthening mechanism induced by GNP reinforcement. The SEM micrographs (Fig. 3.24) on the fracture surface of the samples are analyzed to explain the strengthening mechanism and mode of failure of the samples during flexure. The micrograph of monolithic ZrB_2 indicates brittle and predominantly intergranular fracture and the grains appear to have sharp edges. It also indicates faster crack propagation and quick failure due to lack of any strengthening mechanisms. Whereas the composites shows less brittle and transgranular fracture (4 and 6% GNP composites) microstructure and also the anchoring of the GNP sheets along the grain boundaries can be clearly seen in the 4 and 6% composites (also refer fig.3.25). This kind of GNP wrapping along the grains has strengthened the composites by resisting the GNP pull-out.

3.3.3.3 Fracture Toughness

The composites had a significant improvement in fracture toughness compared to the monolith. Among the composites the 6% GNP composite had the highest average toughness of 2.77±0.06 $MPa.m^{1/2}$ which is ~80% more than the monolithic ZrB_2 which had an average toughness of 1.51±0.02 $MPa.m^{1/2}$. The 2 and 4% composites had an average toughness of 2.10±0.43 and 2.15±0.24 $MPa.m^{1/2}$. Figure 3.30 shows the variation of toughness of the monolith and composites. The improvement in the fracture toughness of the composites is attributed to novel toughening mechanisms like crack bridging, necking of GNP and crack deflection by GNP. Better density of the composites also helped in improvement of toughness. For similar density of ZrB_2 the 2 vol.% GNP composites had better fracture toughness due to the above mentioned toughening mechanisms.

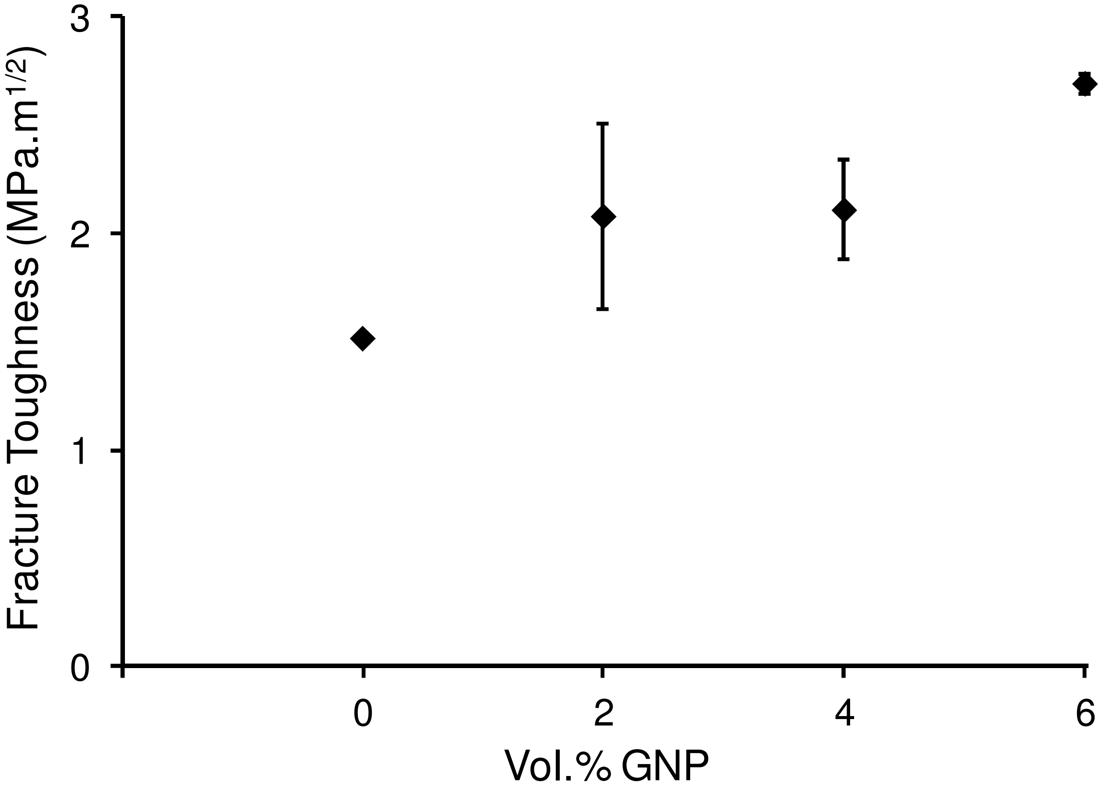

Fig. 3.30 Fracture toughness of ZrB_2-GNP composites as a function of reinforcement content.

SEM was carried out to study the crack propagation and toughening mechanisms in the composites. Figure 3.31 shows the SEM micrographs of crack propagation in the monolith and GNP composites. The crack follows a fairly straight path in the monolithic ZrB2 without any crack deflection or bridging mechanisms. The crack propagation was predominantly intergranular tracing the grain boundaries. The micrograph also shows distributed porosity on the polished surface of ZrB_2. The crack had to follow a more torturous path in the GNP composites. Crack bridging and deflection was noted when the crack approaches the GNP and it was a combination of both inter- and transgranular crack propagation. To make sure that the dark features enabling the toughening in composites seen on the polished surfaces are GNP and pores, we carried out Raman spectroscopy on these dark patches. The Raman spectra proved that these dark patches on the polished surfaces are GNP.

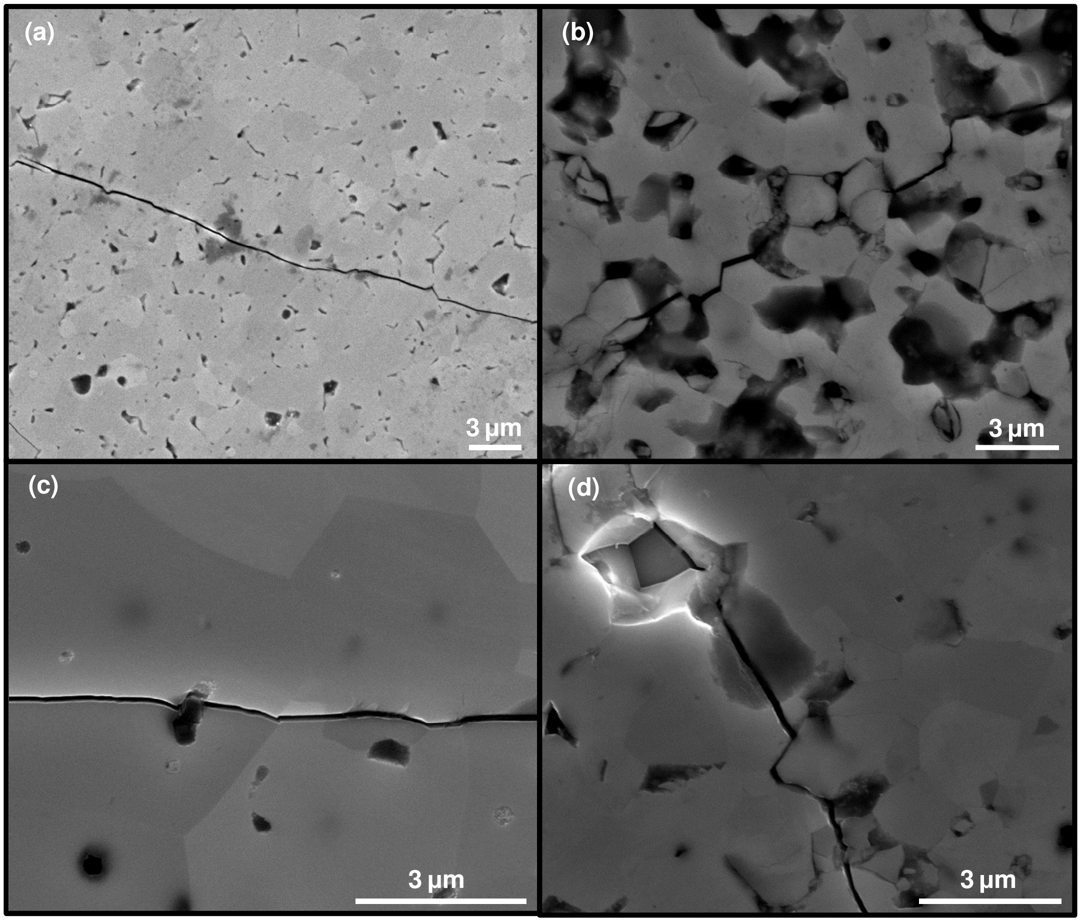

Fig. 3.31 High Magnification Crack Propagation and Toughening mechanism of (a) Monolithic ZrB_2 (b) 2% GNP (c) 4% GNP and (d) 6% GNP.

For better understanding of the toughening mechanisms in the composites, high magnification SEM was carried out the cracks. Figure 3.32 shows the toughening mechanisms in the 2,4 and 6% GNP composites.

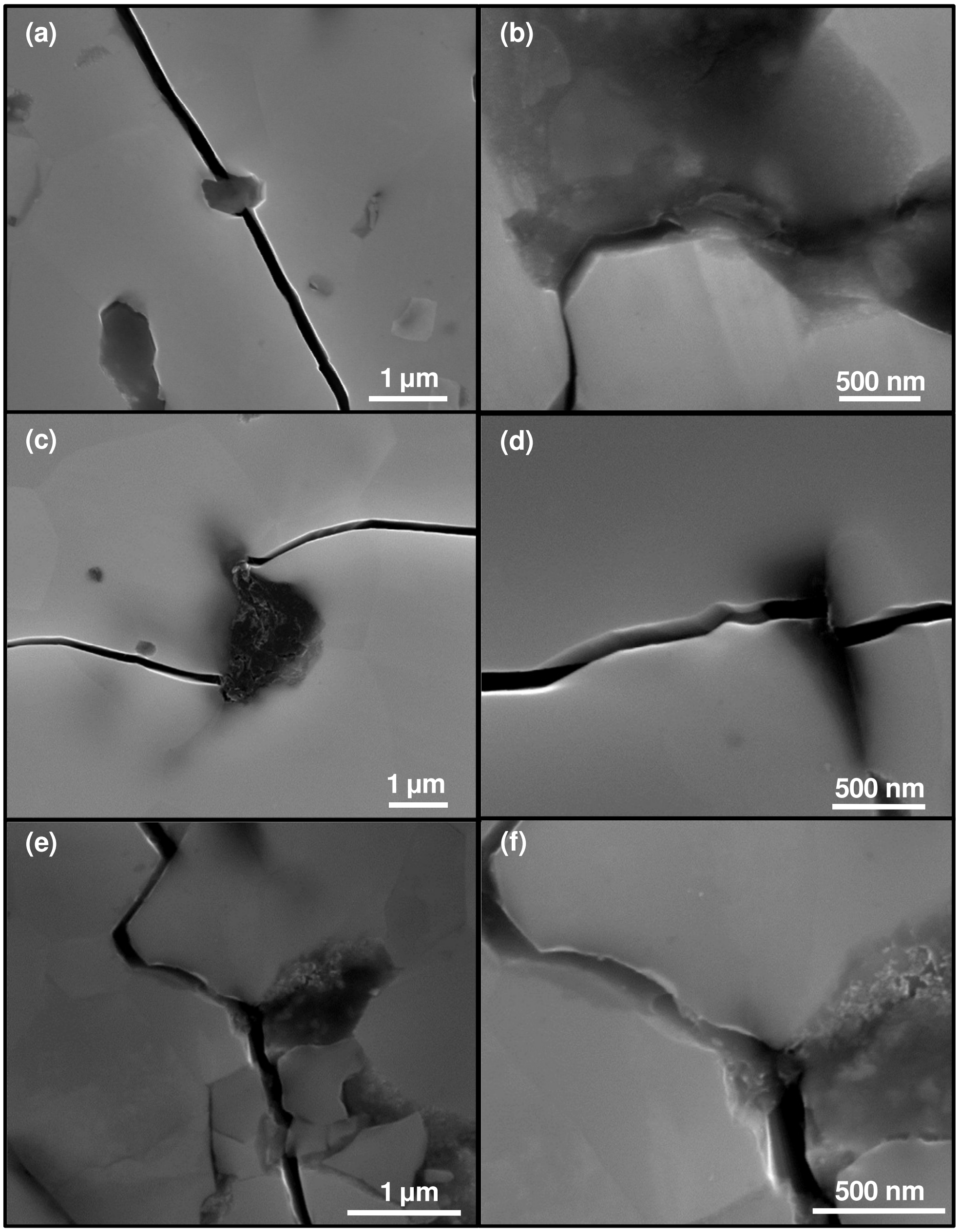

Fig. 3.32 High and low magnification SEM micrographs showing fracture toughness mechanism in (a,b) 2% GNP composite, (c,d) 4% GNP composite, (e,f) 6% GNP composite.

Fig. 3.32(a) shows the bridging and necking of the GNP as a toughening mechanism for the 2% composite. It can be seen that the size of the GNP is much smaller that the starting size of 5 μm diameter. This reduction in size is caused by ball milling of the composite powders. Fig. 3.32(c) shows the deflection of crack caused by a bigger GNP in the 4% composite. The crack is deflected, but we cannot see the path of deflection. This phenomenon may be the interesting three dimensional crack propagation induced by the GNP as explained in reference 31. More analysis is need for better understanding of this three dimensional crack propagation mechanism. Fig. 3.32(d) also shows crack deflection due to GNP in 4% GNP. We can also see presence of GNP along the crack for 2 and 6% composites (high magnification SEM images, fig. 3.32(b,e,f). It is interesting to see that the crack is able to break through the GNP in the 6% composite. But there is more energy in breaking of the GNP by the crack and thus it acts as a better toughening mechanism in the 6% composite leading to its better toughness. The wrapping of GNP sheets along the grain boundaries resists GNP pull-out by crack propagation and contributes to the improvement of toughness in the composites. This kind of sheet wrapping mechanism is better that nanotube and spherical nano reinforcements, since the energy needed for the pull-out of the wrapped sheets is much larger that the energy needed for nanotube and nano reinforcements pull-out. The SEM analysis has explained the toughening mechanisms in the composites.

Table 3.3 lists the relative density and mechanical properties of monolithic ZrB_2 and ZrB_2-GNP ceramic composites.

Table 3.3 Relative density and mechanical properties of ZrB_2 and ZrB_2-GNP ceramic composites.

Sample	Relative density (%)	Hardness (GPa)	Fracture toughness ($MPa.m^{1/2}$)	Flexural strength (MPa)
ZrB_2	84.8	16.64±0.90	1.51±0.02	162±31
ZrB_2+2%GNP	84.5	13.53±0.25	2.10±0.43	204±34
ZrB_2+4%GNP	96.5	15.90±0.84	2.15±0.24	219±23
ZrB_2+6%GNP	96.9	14.00±0.60	2.77±0.06	316±85

CHAPTER 4

Conclusions

- Spark plasma sintering was successfully used to sinter monolithic ZrB_2 (relative density ~85%) and highly dense (relative density >95) SiC, CNT and GNP reinforced ZrB_2 composites with SPS processing parameters of 1900˚C with a heating rate of 100˚C/min, uniaxial pressure of 70 MPa and soaking time of 15 min.
- Detailed analysis of punch displacement during SPS sintering indicated that the densification is favored for the ZrB_2-SiC, ZrB_2-CNT and ZrB_2-GNP composite samples in early stage I (attributed to particle re-distribution and lubricating effect of CNTs and GNP) and final stage III (densification due to pulsed DC and simultaneous pressure leading to mass transfer by necking and volume diffusion, starting at earlier times and at lower temperatures).
- While fine grains of ~2 µm were retained in ZrB_2-SiC composites, some grain growth with grain size in the range of 5-10 µm and 2-4 µm were observed for ZrB_2-CNT and ZrB_2-GNP composites respectively.

- XRD analysis indicated that no undesirable interfacial reactions took place during SPS of the composites. All ZrB_2 and SiC peaks were identified in ZrB_2-SiC composites.
- SEM micrographs showed the presence of CNT networks and wrapping of GNP along the ZrB_2 grains in ZrB_2-CNT and ZrB_2-GNP composites respectively.
- Raman spectroscopy analysis indicated that the multi-walled CNTs and GNP were retained in ZrB_2-CNT and ZrB_2-GNP composites sintered at high sintering temperature of 1900˚C.
- While SiC reinforcement improved the microhardness of the ZrB_2 composite. Whereas no hardening effect was observed in CNT and GNP reinforced ZrB_2 composites.
- All composites had better fracture toughness than monolithic ZrB_2. The SiC, CNT and GNP reinforcement improved the indentation fracture toughness of the composites through a range of toughening mechanisms, including particle shearing, crack deflection at the particle-matrix interface, and grain pull-outs for ZrB_2-SiC composites, CNT pull-outs and crack deflection in ZrB_2-CNT composites and GNP sheet pull-out, crack deflection and crack bridging in case of ZrB_2-GNP composites.

CHAPTER 5

FUTURE WORKS

- Perform high temperature mechanical testing on ZrB_2 ceramic composites.
- To understand the densification and grain growth mechanism in CNT and GNP reinforced composites.
- Investigate the thermal and electrical conductivities of ZrB_2 ceramic composites.
- Perform Raman spectroscopy to study the exfoliation of GNP during ball milling and high temperature sintering and the energy absorbed by GNP during crack deflection and bridging.
- Conduct oxidation testing on SiC, CNT and GNP reinforce ZrB_2 at a temperature range of 1500-2000 ˚C and study the evolution of oxidation products with help of XRD, SEM and EDS analysis.
- Net shaping using Spark plasma sintering.

REFERENCES

1. M.J. Gasch, D.T. Ellerby, S.M. Johnson, Ultra High Temperature Ceramic Composites. In: N. Bansal (ed.), *Handbook of Ceramic Composites*, Kluwer Academic Publishers, Boston, USA, **2005.**
2. L. Kaufman, E.V. Clougherty, RTD-TRD-N63-4096, Part III, ManLabs Inc, Cambridge, MA, **1966.**
3. E.V. Clougherty, D. Kailash, E.T. Peters, AFML-TR-68-190, ManLabs Inc, Cambridge, MA, **1968.**
4. P.T.B. Shaffer, *Ceramics and Glasses: Engineered Materials Handbook*, Vol. 4, ed. By S.J. Schneider, Jr., ASM International, Materials Park, Ohio, **1991**.
5. S. Hampshire, *Ceramics and Glasses: Engineered Materials Handbook*, Vol. 4, ed. By S.J. Schneider, Jr., ASM International, Materials Park, Ohio, **1991**.
6. R.A. Cutler, *Ceramics and Glasses: Engineered Materials Handbook*, Vol. 4, ed. By S.J. Schneider, Jr., ASM International, Materials Park, Ohio, **1991**.
7. M.M. Opeka, I.G. Talmy, E.J. Wuchina, J.A. Zaykoski, S.J. Causey, *J. Eur. Ceram. Soc.* **1999**, 19, 2405.
8. E.L. Courtright, H.C. Graham, A.P. Katz, R. J. Kerans, AFWAL-TR-91-4061, Wright Patterson Air Force Base, Ohio, **1992.**
9. H.E. Exner, Int. Metall. Rev. **1979**, 4, 149.

10. W.H. Rhodes, E.V. Clougherty, D. Kalish, AFML-TR-68-190, Part II, Vol. IV, ManLabs Inc., Cambridge, MA, **1970**.
11. P. Kolodziej, J. Salute, D.L. Keese, NASA TM-112215, **1997**.
12. C. Mroz, *Am. Ceram. Soc. Bull.* **1995**, 74, 164.
13. K. Upadhya, M. J. Yang, W. P. Hoffmann, *Am. Ceram. Soc. Bull.* **1997**, 58, 51.
14. E. V. Clougherty, R. J. Hill, W. Rhodes, E. T. Peters, AFML-TR-68-190,Part II, Vol. II, ManLabs Inc, Cambridge, MA, **1970.**
15. E.V. Clougherty, R.L. Pober, L. Kaufman, Trans. TMS-AIME **1968**, 242, 1077.
16. K.K. Chawla, M. Metzger, *J. Mater. Sci.* **1972**, 7, 34.
17. N. Chawla, Y.L. Shen, *Adv. Eng. Mater.* **2001**, 6, 3.
18. R.G. Munro, J. Phys. Chem. Ref. Data **1997**, 26, 1195.
19. A.L. Chamberlain, W.G. Fahrenholtz, G.E. Hilmas, *J. Am. Ceram. Soc.* **2004**, 87 [6], 1170.
20. R. Telle, L.S. Sigl, K. Takagi, *Hand Book of Ceramic Hard Materials*, ed. by R. Riedel, Wiley-VCH, Weinheim, Germany, **2000**.
21. A. L. Chamberlian, W. G. Fahrenholtz, G. E. Hilmas, D. T. Ellerby, *J. Am. Ceram. Soc.* **2004**, 87, 1170.
22. F. Monteverde, *Compos. Sic. Technol.***2005**, 65, 1869.
23. F. Monteverde, Appl. Phys. A: Mater. Sci. Process. **2006**, 82, 329.
24. F. Monteverde, C. Melandri, S. Guicciardi, *Mater. Chem. Phys.* **2006**, 100, 513.
25. F. Monteverde, *J. Alloys Compd.* **2007**, 428, 197.
26. H. Wang, C. A. Wang, X. Yao, D. Fang, *J. Am. Ceram. Soc.* **2007**, 90, 1992.

27. I. Akin, M. Hotta, F.C. Sahin, O. Yucel, G. Goller, T. Goto, *J. Eur. Ceram. Soc.* **2009**, 29, 2379.

28. W. C. Tripp, H. H. Davis, H. C. Graham, *Am. Ceram. Soc. Bull.* **1973**, 52[8], 612.

29. W.C. Tripp, H.C. Graham, *J. Electrochem. Soc.* **1971**, 118[7], 1195.

30. F. Monteverde, A. Bellosi, J. Am. Electrochem. Soc. 2003, 150[11], B552.

31. F. Monteverde, R. Savino, *J. Eur. Ceram. Soc*. **2007**, 27, 4797.

32. A. Rezaie, W.G. Fahrenholtz, G.E. Hilmas, *J. Eur. Ceram. Soc*. **2007**, 27, 2495.

33. I.G. Talmy, J.A. Zaykoski, M.M. Opeka, *J. Am. Ceram. Soc.* **2008**, 91[7], 2250.

34. J. Han, P. Hu, X. Zhang, S. Meng, Scripta Mater. 2007, 57, 825.

35. J. Han, P. Hu, X. Zhang, S. Meng, W. Han, *Compos. Sic. Technol.* **2008**, 68, 799.

36. C. Tian, D. Gao, Y. Zhang, C. Xu, Y. Song, X. Shi, *Corros. Sic.* **2011**, 53, 3742.

37. L. Silverstrani, D. Sciti, *J. Am. Ceram. Soc.* **2011**, 94[9], 2796.

38. M. Mallik, K.K. Ray, R. Mitra, *J. Eur. Ceram. Soc.* **2011**, 31, 199.

39. G. Li, W. Han, B. Wang, *Mater. Des.* **2011**, 32, 401.

40. S.C. Zhang, G.E. Hilmas, W.G. Fahrenholtz, *J. Eur. Ceram. Soc.* **2011**, 31, 893.

41. K.K. Chawla, N. Chawla, *John Wiley & Sons*, Inc. **2000**, 16, 137.

42. T.J. Clark, R.M. Arons, J.B. Stamatoff, J. Rabe, *Ceramic Engineering and Science Proceedings*, **1985**, 6, 576.

43. X. Zhang, L. Xu, S. Du, C. Liu, J. Han, W. Han, *J. Alloys Compd*. **2008**, 466, 241.

44. P. Zhang, P. Hu, X. Zhang, J. Han, S. Meng, *J. Alloys Compd*. **2009**, 472, 358.

45. D. Chen, L. Xu, X. Zhang, B. Ma, P.Hu, *Int. J. Refract. Met. Hard Mater.* **2009**, 27, 792.

46. S. Guicciardi, L. Silvestroni, M. Nygren, D. Sciti, *J. Am. Ceram. Soc.* **2010**, 93[8], 2384.
47. X. Zhang, L. Xu, W. Han, L. Weng, J. Han, S. Du, *Solid State Sci.* **2009**, 11, 156.
48. L. Silvestroni, D. Sciti, C. Melandri, S. Guicciardi, *J. Eur. Ceram. Soc*. 2010, 30, 2155.

49. S.C. Zhang, G.E. Hilmas, W.G. Fahrenholtz, *J. Am. Ceram. Soc.* **2006**, 89(5), 1544.
50. S. Park, R. S. Ruoff, *Nat. Nanotechnol.* 2009, 4, 217.
51. A. K. Geim, K. S. Novoselvo, *Nat. Mater.* 2007, 6, 183.
52. M. Segal, *Nature Nanotechnol.* 2009, 4, 612.
53. A.A. Balandin, S. Ghosh, W. Bao, I. Calizo, D. Teweldebrhan, F. Miao, C.N. Lau, *Nano Lett*. 2008, 8, 902.
54. C. Lee, X. Wei, J.W. Kysar, J. Hone, *Science* **2008**, 321, 385.
55. C. Soldano, A. Mahmood, E. Dujardin, *Carbon* **2010**, 48, 2127.
56. Y. Zhang, J.P. Small, W.V. Pontius, P. Kim, *Appl. Phys. Lett.* **2005**, 86, 073104.
57. K.S. Novoselvo, A.K. Geim, D. Jiang, M.I. Katsnelson, I.V. Grigorieva, A.A. Firsov, *Science* **2004**, 306, 666.
58. K. S. Novoselov, E. McCann, S. V. Morozov, V. I. Fal'ko, M. I. Katsnelson, U. Zeitler, D. Jiang, F. Schedin and A. K. Geim, *Nature Phys.* **2006**, 2, 177.
59. O. Tapaszto, L. Tapaszto, M. Marko, F. Kern, R. gadow, C. Balazsi, *Chem Phys Lett*. **2011**, 511, 340.
60. S. Stankovich, D.A. Dikin, G.H.B. Dommett, K.M. Kohlhass, E.J. Zimney, E.A. Stach, *Nature* **2006**, 442, 282.
61. U.Khan, P. May, A. O’Neill, N.J. Coleman, *Carbon* **2010**, 48, 4035.

62. T. Ramanathan, A.A. Abdala, S. Stankovich, D.A. Dikin, M. Herrera-Alonso, R.D. Piner, D.H. Adamson, H.C. Schniepp, X. Chen, R.S. Ruoff, *Nat Nanotechnol*, **2008**,3,327.
63. M.A. Rafiee, J. Rafiee, Z. Wang, H. Song, Z.Z. Yu, N. Koratkar, *ACS Nano* **2009**, 3, 3884.
64. L.S. Walker, V.R. Marotto, M.A. Rafiee, N. Koratkar, E.L. Corral, *ACS Nano* **2011**, 5, 3182.
65. P. Kun, O. Tapaszto, F. Weber, C. Balazsi, *Ceram. Int.* **2012**, 38, 211.
66. J. Wang, Z. Li, G.fan, H. Pan, Z.Chen, D. Zhang, *Scripta Mater.* **2012**, 66, 594.
67. Z. Wang, S. Wang, X. Zhang, P. Hu, W. Han, C. Hong, *J. Alloys Compd.* **2009**, 484, 390.
68. Z. Wang, Z. Wu, G. Shi, *Mater. Sci. Eng. A* **2011**, 528, 2870.
69. M.S. Dresselhaus, A. Jorio, M. Hofmann, G. Dresselhaus, R. Saito, *Nano Lett.* **2010**, 10 (3), 751.
70. E.F. Antunes, A.O. Lobo, E.J. Corat, V.J. Trava-Airoldi, A.A. Martin, C. Verissimo, *Carbon* **2006**, 44 (11), 2202.
71. S. Iijima, *Nature* **1991**, 354, 56.
72. W.Z. Wang, J.Y. Huang, D.Z. Wang, Z.F. Ren, *Carbon* **2005**, 43, 1328.
73. M.V. Antisari, R. Marazzi, R. Krsmanovic, *Carbon* **2003**, 41, 2393.
74. E.V. Barrera, M.L. Shofner and E.L. Corral, *Carbon Nanotubes in Science and Application*, In: M. Meyyappan (Ed.), CRC Press, New York, **2005**.
75. G.D. Zhan, J.D. Kuntz, J.Wan, A.K. Mukherjee, *Nat. Mater.* **2003**, 2 (1), 38.
76. J. Sun, L. Gao, X.H. Jin, *Ceram. Int.* **2005**, 31, 893.

77. J.-W. An, D.-S. Lim, *J. Ceram. Proc. Res.* **2002**, 3 (3), 201.
78. C. Balazsi, Z. Shen, Z. Konya, Z. Kasztovsky, F. Weber, Z. Vertesy, L.P. Biro, I. Kiricsi, P. Arato, *Compos. Sci. Technol.* **2005**, 65 (5), 727.
79. J. Tatami, T. Katashima, K. Komeya, T. Meguro, T. Wakihara, *J. Am. Ceram. Soc.* **2005**, 88 (10), 2889.
80. E.L. Corral, H. Wang, J. Garay, Z. Munir, E.V. Barrera, *J. Eur. Ceram. Soc*. **2011**, 31 (3), 391.
81. W.-B Tian, Y.-M Kan, G.-J. Zhang, P.-L. Wang, *Mater. Sci. Eng. A* **2008**, 487, 568.
82. F. Yang, X. Zhang, J. Han, S. Du, *Mater. Lett.* **2008**, 62, 2925.
83. F. Yang, X. Zhang, J. Han, S. Du, *Mater. Des.* **2008**, 29, 1817.
84. F. Monteverde, A. Bellosi, *Adv. Eng. Mater.* **2004**, 6, 331.
85. F. Monteverde, A. Bellosi, *J. Eur. Ceram. Soc*. **2004**, 25, 1025.
86. F. Monteverde, L. Scatteia, *J. Am. Ceram. Soc.* **2007**, 90 (4), 1130.
87. D. Sciti, L. Silvestroni, M. Nygren, *J. Eur. Ceram. Soc*. **2008**, 28, 1287.
88. D. Sciti, G. Bonnefont, G. Fantozzi, L. Silvestroni, *J. Eur. Ceram. Soc*. **2010**, 30, 3253.
89. M. Gasch, S. Johnson, *J. Eur. Ceram. Soc*. **2010**, 30, 2337.
90. L. Weng, X. Zhang, J. Han, W. Han, C. Hong, *J. Alloys Compd*. **2009**, 473, 314.
91. R. Licheri, R. Orru, C. Musa, A.M. Locci, G. Cao, *J. Alloys Compd*. **2009**, 478, 572.
92. D. Sciti, L. Silvestroni, M. Nygren, *Scripta Mater*. **2008**, 58, 638.
93. L. Zhao, D. Jia, X. Duan, Z. Yang, Y. Zhou, *J. Alloys Compd*. **2011**, 509, 9816.
94. A. Sayir, *J. Mater. Sci.* **2004**, 39, 5995.

95. L. Silvestroni, A. Bellosi, C. Melandri, D. Sciti, J.X. Liu, G.J. Zhang, *J. Eur. Ceram. Soc*. **2011**, 31, 619.
96. E. Khaleghi, Y.-S. Lin, M.A. Mayers, E.A. Olevsky, *Scripta Mater.* **2010**, 63, 577.
97. S.R. Bakshi, V. Musaramthota, D. Lahiri, V. Singh, S. Seal, A. Agarwal, *Mater. Sci. Eng. A* **2010**, 528, 1287.
98. S.R. Bakshi, V. Musaramthota, D.A. Virzi, A.K. Keshri, D. Lahiri, V. Singh, S. Seal, A. Agarwal, *Mater. Sci. Eng. A* **2010**, 528, 2538.
99. L. Liu, F. Ye, Y. Zhou, *Mater. Sci. Eng. A* **2010**, 528, 4710.
100. Z.A. Munir, U.A.Tamburini, *J. Mater. Sci.* **2006**, 41, 763.
101. M. Tokita, Proceeding of NEDO International symposium, 1999.
102. J.E. Garay, *Annu. Rev. Mater. Res*. **2010**, 40, 12.1.
103. J. Xu, S.R. Casolco, J.E. Garay, *J. Am. Ceram. Soc*. **2009**, 92, 1506.
104. W. Chen, U.A. Tamburini, J.E. Garay, J.R. Groza, Z.A. Munir, *Mater. Sci. Eng. A* **2005**, 394, 139.
105. U.A. Tamburini, S. Gennari, J.E. Garay, Z.A. Munir, *Mater. Sci. Eng. A* **2005**, 394, 132.
106. S.-Q. Guo, J.M. Yang, H. Tanaka, Y. Kagawa, *Comp. Sci. Technol.* **2008**, 68, 3033.
107. W.M. Guo, J. Vleugels, G.J. Zhang, P.L. Wang, O.V. Biest, *Scripta Mater.* **2010**, 62, 802.
108. S.R. Levine, E.J. Opila, M.C. Halbig, J.D. Kiser, M. Singh, J.A. Salem, *J. Eur. Ceram. Soc*. **2002**, 22, 2757.
109. W.-W. Wu, G.-J. Zhang, Y.-M. Kan, P.-L. Wang, K. Vanmeensel, J. Vleugels, O.V. Biest, *Scripta Mater.***2007**, 57, 317.

110. C.Q. Hong, X.H. Zhang, W.J. Li, J.C. Han, S. H. Meng, *Mater. Sci. Eng. A* **2008**, 498, 437.
111. Q. Liu, W. Han, X. Zhang, S. Wang, J. Han, *Mater. Lett.* **2009**, 63, 1323.
112. Y. Zhao, L.J. Wang, G.J. Zhang, W. Jiang, L.D. Chen, *Int. J. Refract. Met. Hard Mater.* **2009**, 27, 177.
113. Q. Liu, W. Han, J. Han, *Scripta Mater.* **2010**, 63, 581.
114. M. Cao, S. Wang, W. Han, *Mater. Sci. Eng. A* **2010**, 527, 2925.
115. P. Hu, Z. Wang, *J. Eur. Ceram. Soc*. **2010**, 30, 1021.
116. S. Ran, O.V. Biest, J. Vleugels, *J. Eur. Ceram. Soc*. **2010**, 30, 2633.
117. W. Zhang, I. Srivastava, Y-F. Zhu, C.R.Picu, N. Koratkar, *Small* **2009**, 5, 1403.
118. M.V. Antisari, A. Montone, N.Jovic, E. Piscopiello, C. Alvani, L.Pilloni, *Scripta Mater.* **2006**, 55, 1047.
119. K.A. Khalil, S.W. Kim, *Int. J. Appl. Ceram. Techno*. **2006**, 3, 322.
120. ASTM C1499-05, *Standard test method for monotonic equibiaxial flexural strength of advanced ceramics at ambient temperature*, vol. ASTM International, 1499.
121. J.E.O. Ovri, *Mater. Chem. Phys.* **2000**, 66(1), 1.
122. J.W. Zimmermann, G.E. Hilmas, W.G. Fahrenholtz, R.B. Dinwiddie, W.D. Porter, H. Wang, *J. Am. Ceram. Soc*. **2008**, 91, 1405.
123. S. Berber, Y.K. Kwon, D. Tomanek, *Phys. Rev. Lett*. **2000**, 84, 4613.
124. J. Ado, M.S. Dresselhaus, S. Ricchiro, G.F. Dresselhaus, *Raman Spectroscopy in Graphene Related Systems,* WILEY - VCH Verlag GmbH & Co. KGaA : Weinheim, Germany, 2011.
125. A.C. Ferrari, J. Robertson, *Phys. Rev. B* **2000**, 61, 14095.

126. J. Watts, G. Hilmas, W.G. Fahrenholtz, D. Brown, B. Clausen, *J. Eur. Ceram. Soc.* **2010**, 30, 2165.
127. X. Wang, N.P. Padture, H. Tanaka, *Nat. Mater.* **2004**, 3 , 539.
128. P.M. Ajayan, L.S. Schadler, C. Giannaris, A. Rubio, *Adv. Mater.* **2000**, 12, 750.
129. O. Lourie, H.D. Wagner, *J. Mater. Res.* **1998**, 13, 2418.
130. A.A. Balamdin, S. Ghosh, W. Bao, I. Calizo, D. Teweldebrhan, F. Miao, C.N. Lau, *Nano Lett.* **2008**, 8, 902.
131. J. Ado, M.S. Dresselhaus, S. Ricchiro, G.F. Dresselhaus, *Raman Spectroscopy in Graphene Related System*, WILEY-VCH Verlag GmbH & Co. KGaA: Weinheim, Germany **2011**.
132. M.S. Dresselhaus, A. Jorio, M. Hofmann, G. Dresselhaus, R. Saito, *Nano Lett.* **2010**, 10 (3), 751.
133. A.C. Ferrari, J. Robertson, *Phys. Rev. B* **2000**, 61 (20), 14095.
134. X. Wang, N.P. Padture, H. Tanaka, *Nat. Mater.* **2004**, 3 (8), 539.
135. P.M. Ajayan, L.S. Schadler, C. Giannaris, A. Rubio, *Adv. Mater.* **2000**, 12 (10), 750.
136. G. Tsoukleri, J. Parthenios, K. Papagelis, R. Jalil, A.C. Ferrari, A.K. Geim, K.S.Novoselov, C. Galiotis, *Small* **2009**, 5 (21), 2397.
137. A. Gupta, G. Chen, P. Joshi, S. Tadigadapa, P.C. Eklund, *Nano Lett.* **2006**, 6 (12), 2667.
138. A.C. Ferrari, J.C. Meyer, V. Scardaci, C. Casiraghi, M. Lazzeri, F. Mauri, .S Piscanec, D. Jiang, K.S. Novoselov, S. Roth, A.K. Geim, *Phys. Rev. Lett.* **2006**, 97 (18), 187401.

139. K. Takai, M. Oga, H. Sato, T. Enoki, Y. Ohki, A. Taomoto, K. Suenaga, S. Iijima, *Phys. Rev. B* **2003**, 67 (21), 214202.

140. J. Ado, M.L. Marcia, S. Fernando, H.M.F. Erlon, V.O.M. Marcus, B.C. Rodrigo, A.A. Carlos, *J. Phys.: Condens. Matter* **2010**, 22 (33), 334204.

141. E.H. Martins Ferreira, M.V.O. Moutinho, F. Stavale, M.M. Lucchese, R.B. Capaz, C.A. Achete, A. Jorio, *Phys. Rev. B* **2010**, 82 (12), 125429.

142. A. Das, S. Pisana, B. Chakraborty, S. Piscanec, S.K. Saha, U.V. Waghmare, K.S. Novoselov, H.R. Krishnamurthy, A.K. Geim, A.C. Ferrari, A.K. Sood, *Nat. Nanotech.* **2008**, 3 (4), 210.

APPENDICES

PUBLICATION

Govindaraajan B. Yadhukulakrishnan, Arif Rahman, Sriharsha Karumuri, M. Stackpoole, A. Kaan Kalkan, Raman P. Singh, Sandip P. Harimkar, Spark Plasma Sintering of Silicon Carbide and Multi-walled Carbon Nanontube Reinforced Zirconium Diboride Ceramic Composite, In Press, *Materials Science and Engineering A* **2012**.

VITA

Type Full Name Here

Candidate for the Degree of

Master of Science

Thesis: SPARK PLASMA SINTERING OF SILICON CARBIDE, MULTI-WALLED CARBON NANOTUBE AND GRAPHENE REINFORCED ZIRCONIUM DIBORIDE CERAMIC COMPOSITE

Major Field: Mechanical and Aerospace Engineering

Biographical:

Education:

Completed the requirements for the Master of Science in Mechanical and Aerospace Engineering at Oklahoma State University, Stillwater, Oklahoma, in July, 2012.

Completed the requirements for the Bachelor of Sciences in Mechanical Engineering at Anna University, Chennai, India, in 2010.

Experience:

- One year and six months of research experience in Materials Engineering, as Graduate Research Assistant at OSU.
- Graduate Teaching Assistant for Engineering Design CAD, Mechanical Design II and Elementary Dynamics courses at OSU.
- Student Intern at Ashok Leyland Ltd, Royal Enfiel and India Piston Rings Ltd, Chennai, India.
- Author of ‘Spark Plasma Sintering of SiC and MWCNT Reinforced ZrB_2 Ceramic Composite’, *Materials Science and Engineering A*, In Press.

Professional Memberships:
Student Member of ASME (American Society of Mechanical Engineers).

Name: Govindaraajan Balaraman Yadhukulakrishnan Date of Degree: July, 2012

Institution: Oklahoma State University Location: Stillwater, Oklahoma

Title of Study: SPARK PLASMA SINTERING OF SILICON CARBIDE, MULTI-WALLED CARBON NANOTUBE AND GRAPHENE REINFORCED ZIRCONIUM DIBORIDE CERAMIC COMPOSITE

Pages in Study: 126 Candidate for the Degree of Master of Science

Major Field: Mechanical and Aerospace Engineering

Scope and Method of Study:

Space vehicles re-entering the earth's atmosphere experience very high temperatures due to aerodynamic heating. Ultra-high temperature ceramics (UHTC) with melting point higher than 3200°C are promising materials for thermal protection systems of such space vehicles re-entering the earth's atmosphere. Among several UHTC systems ZrB_2 based ceramic composites are particularly important for thermal protection systems due to their better mechanical and thermoelectric properties and high oxidation resistance. In this study spark plasma sintering of SiC, carbon nanotubes (CNT) and graphene nano platelets (GNP) reinforced ZrB_2 ultra-high temperature ceramic matrix composites is reported.

Findings and Conclusions:

Systematic investigations on the effect of reinforcement type (SiC, CNTs and GNP) and content (10-40 vol.% SiC, 2-6 vol.% CNTs and 2-6 vol.% GNP) on densification behavior, microstructure development, and mechanical properties (microhardness, bi-axial flexural strength, and indentation fracture toughness) are reported. With the similar SPS parameters near-full densification (>99% relative density) was achieved with 10-40 vol.% SiC, 4-6 vol.% CNT reinforced composites. Highly dense composites were obtained in 4-6 vol.% GNP reinforced composites. The SiC, CNT and GNP reinforcement improved the indentation fracture toughness of the composites through a range of toughening mechanisms, including particle shearing, crack deflection at the particle-matrix interface, and grain pull-outs for ZrB_2-SiC composites, CNT pull-outs and crack deflection in ZrB_2-CNT composites and crack deflection, crack bridging and GNP sheet pull-out for ZrB_2-GNP composites.

ADVISER'S APPROVAL: Dr. Sandip P. Harimkar